UNIVERSITY OF
BATH

DOCTOR OF ENGINEERING (ENGD)

Advanced 3D and 2D Modelling of HTS CORC Cable based on the T-A Formulation for the Propulsion System of Hybrid-Electric Aircraft

Zhu, Zixuan

Award date:
2020

Awarding institution:
University of Bath

Link to publication

Advanced 3D and 2D Modelling of HTS CORC Cable based on the T-A Formulation for the Propulsion System of Hybrid-Electric Aircraft

Zixuan Zhu

A thesis submitted for the degree of Doctor of Philosophy (PhD)

Department of Electrical and Electronic Engineering

University of Bath

May 2020

Abstract

The dramatic growth and development in the aviation industry contribute to huge amounts of greenhouse gas emissions in the atmosphere. Control of gas emissions from international air transport has become an emergent task to prevent further air pollution caused by carbon emission. Revolutionary design concepts for the next generation of environmentally friendly aircraft with low gas emissions and high efficiency are urgently needed. NASA has been conducting and supporting research on cutting-edge technologies in the aviation industry. Improvements in the design of aeroplane are in urgent need to enhance the performance in terms of noise, gas emissions, reliability and efficiency. A specific innovation objective involves the development of hybrid-electric aircraft, for it has potential advantages including increased fuel efficiency, reduced noise, and it is more environmental-friendly. By far, NASA has started several new projects in the aim of developing enabling technologies for the propulsion system of hybrid-electric aircraft. Boeing, collaborating with Safran, has been investing in electric or hybrid-electric propulsion systems. A 12-seat hybrid-electric commercial aircraft has been under development by U. S. ZUNUM Aero.

The ampacity of power cables used on hybrid-electric aircraft propulsion is expected to be more than several kA. Cross-section of the conventional copper cable increases with the increasing current carrying requirement, making the cable heavy and huge, which may fail to meet the improving fuel efficiency requirement of next-generation aircraft. On the contrary, superconducting cable, having a compact structure and high current carrying capacity, is a promising candidate for the propulsion system of hybrid-electric aircraft. In particular, the Conductor-on-Round-Core (CORC) cable wound with high temperature superconducting (HTS) tapes is an important cabling concept. It is advantageous for its high flexibility, high operating current, high current density, low cryogenic cost, and small bending radii. However, the complex helical geometry of CORC cable makes the understanding of its electromagnetic performance and quench behaviour challenging. This thesis presents a thorough study of HTS CORC cables mainly by numerical methods. The finite element analysis software, COMSOL Multiphysics, is used to build models for the simulation of CORC cables.

The focusing point of the thesis is to understand how the cable structure influences the electromagnetic and quench behaviour, as well as on how these influences can be reduced. The novelty of this thesis mainly lies in the use of a new T-A formulation, which is, for the first time, applied to three-dimensional (3D) modelling of CORC cables with practical geometry. The use of the new T-A formulation in FEM software COMSOL enables the research on how the winding angle and variation of transport current and magnetic field affect the electromagnetic and quench behaviour of CORC cables.

The first model proposed in this research is a 3D T-A CORC cable model. It is used to thoroughly analysing the electromagnetic behaviours of CORC cable. A good agreement is achieved between the simulation results and published experimental data, which proves the accuracy and reliability of the proposed new 3D T-A CORC cable model. A novel 2D T-A CORC cable model is then built to further shorten the computation time from days to less than an hour.

Then, quench behaviour of CORC cable is analysed using a novel 3D multi-physics T-A model to locate the potential cause of quenching during cable operation. The coupling of four modules; the T-formulation module, the A-formulation module, the heat transfer in thin shell module, and the equivalent circuit module, enables the modelling of hotspot-induced quench of CORC cables. The physical process of hotspot-induced quench is simulated and discussed in detail. The influence of uniform and non-uniform terminal contact resistances on the quench behaviours is analysed.

Finally, an HTS tri-axial CORC cable is conceptually designed for the electrical propulsion system of hybrid-electric aircraft. Two 2D T-A models are proposed in the aim of analysing how the n-th harmonic current will affect the AC loss of CORC cable and how it can be improved. The minimum quench energy of the cable during hotspot-induced quenching process is calculated.

The thesis provides efficient modelling tools for thoroughly investigating the electromagnetic and quench behaviour of CORC cables. The powerful modelling tools presented in this thesis will be valuable guidance for the next stage of design of stable-operated

CORC cables with minimized AC losses for high-field and high energy conversion and transmission applications.

Acknowledgement

Firstly, I would like to express my sincere gratitude to my supervisor, Prof. Weijia Yuan. He has guided me into the field of superconductivity since the final year of my undergraduate study. His continuous support on my research work has provided me the power to keep digging into this amazing research area. I would like to sincerely thank Dr. Xiaoze Pei for her generous and kind instructions on both my research and my life here. Also, I would like to thank to Dr. Min Zhang for guiding me on the model development as well as thoughtful advice on paper modification.

I would like to pay special thanks to Dr. Huiming Zhang, for his generous and continuing support throughout my entire research time. With his help, I stepped into this research field and managed to build the very first numerical model on my own. He also gave useful advice that supported me for moving forwards.

Also, I'm eternally grateful to Dr. Yawei Wang, who has guided me to find out my research topic from the very beginning of my PhD life. He passed on his experience to me unreservedly, taught me the correct way to do research, and never hesitated to help me whenever I met difficulties. It is only with his help that I managed to walk through this journey.

To all my colleagues in the applied superconductivity group at the University of Bath: Dr. Jianwei Li, Dr. Zhenyu Zhang, Dr. Fei Liang, Dr. Sriharsha Venuturumilli, Dr. Mariam Elshiekh, Dr. Qixing Sun, Dong Xing, Hamoud Alafnan, Muhammad Zulfiqar Ali, I'm honored to be a part of this amazing group, thank you for showing up every day, for giving me a hand when I met problems, and for cheering me up when I was down. Also, thanks to my colleagues at the University of Strathclyde, Abdelrahman Elwakeel, Felix Huber, Zhidun Zeng, Fangjing Weng and Tian Lan.

Finally, to my family, to all my friends, to all those who have been a part of me getting there. I am beyond words of gratitude. Thank you for always being there for me.

List of Publications

[1] **Zhu, Z.**, Wang, Y., Xing, D., Pei, X., Zhang, M. and Yuan, W., 2019. Quench of a single-layer ReBCO CORC cable with non-uniform terminal contact resistance. *IEEE Transactions on Applied Superconductivity*, 29(5), pp.1-5.

[2] **Zhu, Z.**, Wang, Y., Venuturumilli, S., Sheng, J., Zhang, M. and Yuan, W., 2018. Influence of harmonic current on magnetization loss of a triaxial CORC REBCO cable for hybrid electric aircraft. *IEEE Transactions on Applied Superconductivity*, 28(4), pp.1-5.

[3] Wang, Y., Zhang, M., Grilli, F., **Zhu, Z.** and Yuan, W., 2019.   Study of the magnetization loss of CORCcables using a 3D TA formulation. *Superconductor Science and Technology*, 32(2), p.025003.

[4] Wang, Y., Zheng, J., **Zhu, Z.**, Zhang, M. and Yuan, W., 2019. Quench behaviour of high-temperature superconductor $(RE)Ba_2Cu_3O_x$ CORC cable. *Journal of Physics D: Applied Physics*, 52(34), p.345303.

Table of Contents

List of Figures

xi

List of Tables

List of Abbreviations

1G	First Generation
2D	Two-dimensional
2G	Second Generation
3D	Three-dimensional
AC	Alternating current
BCS	Bardeen-Cooper-Schrieffer theory
CC	Coated-conductor
CO_2	Carbon dioxide
CORC	Conductor-on-Round-Core
DEAP	Distributed electric aerospace propulsion
DOE	The US Department of Energy
EF	Electric fan
FCL	Fault current limiter
FEM	Finite element method
GTF	Geared-turbofan
HTS	High temperature superconductor
LH_2	Liquid hydrogen
LN_2	Liquid nitrogen
LTS	Low temperature superconductor
MEA	More-electric aircraft
MMEV	Minimum magnetic energy variation
MQE	Minimum quench energy
MRI	Magnetic resonance imaging
NMR	Nuclear magnetic resonance
NZPV	Normal zone propagation velocity
PDE	Partial differential equation
PIT	Powder-in-tube

RACC	Roebel-assembled coated conductor
RE	Rare earth
ReBCO	Rare-earth barium copper oxide
SC	Superconductor
TCR	Terminal contact resistance
TeDP	Turbo-electric distributed propulsion
TSTC	Twisted stacked-tape cable
YBCO (or YBa$_2$Cu$_3$O$_7$)	Yttrium barium copper oxide

List of Symbols

Symbol	Description	Unit
θ	Winding angle	Degree (°)
$\boldsymbol{A}$	Magnetic vector potential	Wb/m
$\boldsymbol{B}$	Magnetic flux density	T
$B_{0\perp}$	Perpendicular magnetic field	T
$B_{0\parallel}$	Parallel magnetic field	T
B_{ext}	External magnetic field	mT
B_{irr}	Irreversibility field	T
$\boldsymbol{E}$	Electric field	V/m
E_0 (or E_c)	Critical electric field	V/m
f	Frequency	Hz
f_1	Fundamental frequency	Hz
H_1 & H_2	Magnetic field on the left and right edges of tapes	A/m
H_c	Critical magnetic field	T
H_{c1} & H_{c2}	Lower and upper critical magnetic field	T
I_c	Critical current	A
I_{met}	Transport current flowing in the metallic layer	A
I_{op}	Transport current	A
I_{su}	Transport current flowing in superconducting layer	A
I_{total}	Total current flowing in ReBCO tape	A
$\boldsymbol{J}$	Current density	A/m²
J_c	Critical current density	A/m²
J_e	Engineering critical current density	A/m²
$\boldsymbol{M}$	Magnetization (Magnetic moment/unit volume)	A/m
m	Mass	Kg
n	A constant value with respect to the E-J power law	
$\mathbf{n}$	Normal unit vector	

Q	AC loss per cycle time	*Joules/cycle*
q	Electric charge	*C*
Q_p	The applied heat pulse energy	*mJ*
R_{met}	Resistance in the metallic layer	*Ohm (Ω)*
R_{su}	Resistance in the superconducting layer	*Ω*
R_t	Terminal contact resistance	*$\mu\Omega$*
R_{tape}	Total resistance of ReBCO tape	*$\mu\Omega$*
T	Current vector potential	
t	Time	*s*
T_c	Critical temperature	*K*
T_h	Temperature of superconducting materials	*K*
T_o	Operating temperature	*K*
V	Electric potential	*V*
λ_L	London penetration depth	*nm*
μ	Magnetic permeability	*N/A^2*
Ω	Region of HTS materials in the model	
f_n *(n=2, 3, 4, ...)*	The *n*-th order harmonic frequency	*Hz*

Chapter 1. Introduction

1.1 Thesis background

Human activities can considerably affect the natural greenhouse effect, leading to global warming, which is one of the greatest challenges faced by the world today. Burning fossil fuels including coal and oil puts loads of carbon dioxide (CO_2) and other greenhouse gases into the atmosphere. Too much of these gases trap part of the Sun's heat, causing the earth to warm up. The dramatic growth and development in the aviation industry contribute to around 2.5% of global greenhouse gas emissions and is predicted to consume a quarter of the carbon budget by the year of 2050, which makes it a central point of reducing greenhouse gas emissions in the sector of transportation [1]. By far, however, comprehensive research shows that though innovative airframes, engines, and fans have been continuously developed, it is not enough to slow down the growth rate of CO_2 emissions from international air travel and freight [2].

Control of the gas emissions from international air transport has become an emergent task to prevent further air pollution caused by the carbon emission. Revolutionary design concepts for the next generation of environmentally friendly aircraft with lower gas emissions and higher efficiency are urgently needed. The aircraft industry has been so far boosting the use of electrical power to avoid any further fuel consumption. Driven by this motivation, several concepts for the next generation commercial aviation fleet has been proposed; more-electric aircraft (MEA), turboelectric aircraft, and hybrid-electric aircraft. The particular developing component for these aircraft designs is the propulsion system. An electrical propulsion system delivers low engine noise, reduced fuel consumption and high reliability. However, the narrow space on an aircraft considerably limits the volume and weight of the propulsion system. Superconducting devices are potentially enabling technologies to cope with these limitations while maintain the power transmission requirement. The use of superconducting materials in industrial applications prevents gas emissions and lowers the generation of losses.

A commercial passenger aircraft requires up to 50 MW power to be delivered during the flight [3]. In previous research, comparison was made between a three-phase single-core HTS

cable system (4 km, 450 MVA, 132 kV) and a comparable conventional cable system (450 MVA). The conventional copper cable system, as can be seen in Figure 1. 1, generates way more losses than the total losses in the HTS cable system at a rated current of 2 kA$_{rms}$ [4]. Although the losses in the HTS cable are bit higher than the losses in the conventional cable when there is no load, it increases slowly with the increase of current, and becomes lower than the losses in the conventional cable when the load current reaches around 33% load of the system. This indicates that the HTS cables are mainly dominated by no-load losses, for the thermal insulation of the cables is not ideal. The AC losses generated due to the load are quite small. Moreover, according to research published in [5], a fully superconducting system is 25 times lighter than a conventional cable system. The space needed for a superconducting system is also 12 times less than a conventional cable system. Thus, HTS cables are by far the most feasible and promising candidates for system with heavy loads but limited space to lower the losses in the system, as well as to save space.
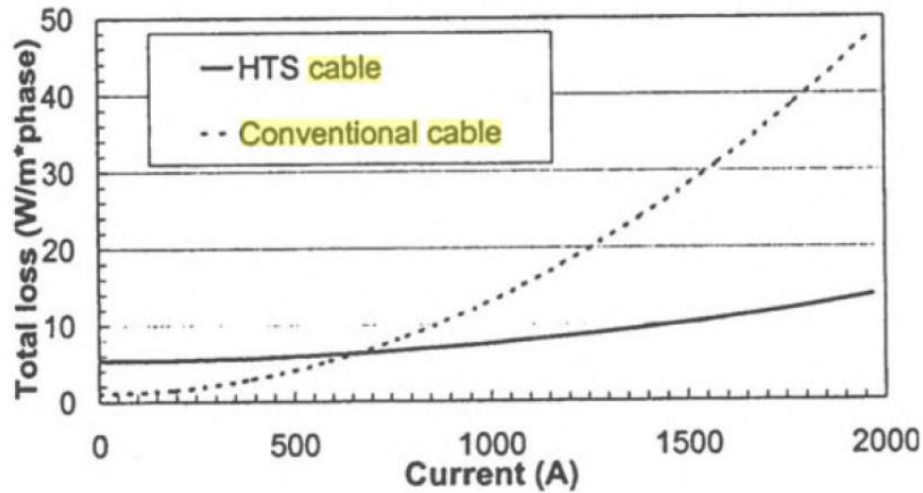
Figure 1. 1 Comparison of total losses in systems that uses an HTS cable and a conventional

cable respectively. The systems have rated power of 450 MVA [4].

One of the HTS cabling concepts, the so-called 'Conductor-on-Round-Core' (CORC) cable, being advantageous for its high flexibility, high operating current, high current density, low cryogenic cost, and small bending radii, is an ideal match for industrial applications that require high-field and low-inductance but has only limited space [6]. This CORC technology has been taken into consideration after the numerous benchmarking [7-9]. It enables the production of

2

round, multi-filament, coated Rare-Earth (RE) $Ba_2Ca_3O_{7-x}$ materials, and has already been applied to widely range of power and magnetic applications [6, 10, 11]. The research and development efforts on CORC cabling technology have been active for the last 10 years.

According to Van der Laan (2018), the US Department of Energy (DOE) has supported HTS CORC cable technology and development to develop HTS cables for use in the electric power grid [12]. The ReBCO conductor applied in the HTS technology is important because it reduces transmission loss, increases the density of power, and supports high magnetic fields. The ReBCO technology is also used in driving wind turbines, medical applications and other power transmission systems that allow high current density power. In the next generation of high field superconducting magnets, accelerator magnets that operate at the field beyond 20 T and some research magnets that operate at the even higher field are required to be constructed using HTS materials [13]. The use of ReBCO technology not only boosts the performance of a cable but also reduces the cost of cabling [14]. It will also benefit magnets, especially those used in the compact fusion machines. Thus, it is suitable to be applied to electrical aircraft design.

For effective operation of the HTS cables, the need for winding ReBCO tapes in a helical manner in a thin core improves the performance of CORC cable and limit heat loss to the surroundings. Therefore, a specific wrapping technology was adopted to avoid the damaging of the superconducting tape during cabling, as shown in the figure below.
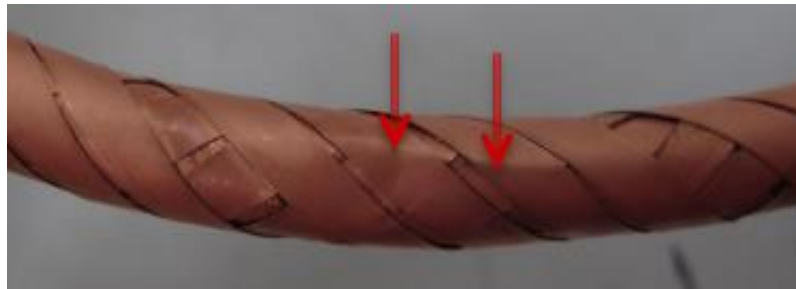
Figure 1. 2 Bending of a CORC cable [7].

Additionally, the full transposition of the tapes in each layer of the CORC cable effectively reduces the coupling current of 2G HTS tapes. It also considerably reduces magnetization loss of the cable. Anvar *et al.* (2018) also stated that the cable experiences a larger tape strain during

cable winding but a lower tape strain in case the cable is bending. In the CORC cable, the tape count is varied in order to suit the range of applications. Wang *et al.* (2019) states that, the CORC cable is suitable for high energy physics applications, as well as for high current density applications [15]. The newly-proposed T-A formulation is employed for three-dimensional modelling of CORC cable. Wang also states that, applying this T-A formulation to FEM software enables the study of how the winding direction and multi-layer structure will influence the AC losses of CORC cables.

1.2 Scope of the study

This dissertation presents a thorough study of the electromagnetic and quench behaviour of HTS CORC cables constructed using ReBCO tapes. The first part of this dissertation investigates the electromagnetic behaviour of HTS CORC cable with various transport current, external magnetic fields and multiple layers. The 3D numerical model used to calculate AC losses of the cable is built using the new T-A formulation and is validated by both experimental data and by comparing with well-validated H-based model. Then, to study the quench behaviour of CORC cable, a 3D multi-physics quench model is proposed. Finally, a conceptual design of HTS tri-axial CORC cable for the propulsion system of hybrid-electric aircraft is proposed. Influence of harmonic current on the AC losses of the proposed cable is numerically simulated and discussed.

The helicity of HTS CORC cable makes the understanding of its electromagnetic as well as quench performance challenging. Since the alternating current (AC) loss can be theoretically examined, conducting numerical calculations will be the basic methodology for the research. However, by far there are limited researches in regard to three-dimensional modelling of HTS CORC cables. Moreover, quench is a quite dramatic event that may occur during the operation of superconductors, causing abrupt temperature increase in a small region. The superconductor might lose its superconductivity for a while, or worse, might be burned out due to this considerable heat generation on a certain spot. Thus, it is always necessary to predict the possibility of quenching for a superconducting cable using numerical methods before the realistic utilization in the industrial area.

This research is focused on building novel numerical models for providing a thorough study on the alternating current (AC) loss and quench behaviour of HTS CORC cables. The modelling will involve the use of both three-dimensional (3D) modelling and two-dimensional (2D) modelling using a new set of formulation, the T-A formulation. The FEM software, COMSOL Multiphysics, is used to build all models proposed in this thesis.

Firstly, it is always important to fully understand how the variation of transport current and external magnetic field affects the transport AC loss and the magnetization AC loss of the HTS CORC cable. Also, the influence of the cable structure (including the winding direction and multi-layer structure) on the AC losses needs to be studied in detail to find out feasible design parameters for practical HTS CORC cables. Numerical modelling of HTS CORC cables with high efficiency is therefore essential to investigate the electromagnetic behaviour of CORC cables. Both 3D and 2D models should be considered.

Secondly, quench is a crucial physical phenomenon that is well-established as propagating slowly in HTS conductors. So far, quench protection remains a key challenge for the cable design. To start with, a thorough understanding of the quench behaviours of the HTS CORC cable is required. Quench behaviour of LTS materials has been well studied previously. However, the quantitative behaviours of HTS materials are quite different [16, 17]. For instance, the minimum quench energy (MQE) of an HTS magnet is relatively high while its corresponding normal zone propagation velocity (NZPV) is much slower than that in a LTS magnet [18-23]. The aim of a quench detection and protection system is to prevent the HTS CORC cable from irreversible degradation caused by a quench. The first step for a quench protection is to detect a disturbance that might induce a quench within the conductors. Thus, a 3D multi-physics quench model for the HTS CORC cable is needed to detect and analyze the quench behaviours of the cable in detail.

The third part of this thesis focuses on the conceptual design of HTS CORC cables that can be applied to construct the electrical propulsion system of hybrid-electric aircrafts. Combined with the tri-axial design, of which three coaxial-arranged phases of the cable are delta-connected, a tri-axial CORC cable will be constructed with a compact structure, high current carrying capacity, reduced use of ReBCO tapes, and reduced capacity of the cryogenic system.

Design concept of the tri-axial CORC cable in this dissertation is to deliver power of 10 MW from the generator to the motors with a rated voltage of 3 kV$_{rms}$ and a rated current of 2 kA$_{rms}$. Components such as generators, motors and AC/DC converters in a practical propulsion system of an electrical aircraft will induce harmonic currents, which might have significant impact on the generation of AC losses. If a tri-axial CORC cable is to be used in the propulsion system, a detailed analysis regarding the influence of harmonic currents on the AC losses of the cable need to be done. As the first stage of this conceptual design, a full cross-sectional 2D T-A based model is needed to calculate the AC losses of the tri-axial CORC cable both with and without the existence of harmonic current to see the actual impact of it. Also, due to the fully axisymmetric geometry of the cross-section of the cable, it is reasonable to build a 1/28 sector-shaped 2D model for the cable to further cut the computation time. Both the full cross-sectional and sector-shaped model should be used to present a thorough study on the influence of harmonic current on the AC losses of the tri-axial CORC cable.

1.3 Structure of the dissertation

This dissertation will investigate the aforementioned problems regarding the HTS CORC cables, in order to provide fully-functional numerical modelling tools to develop HTS CORC cables using 2D and 3D modelling with the T-A formulation technique. Followed the set map for Chapter 1, this thesis is organized as follows:

Chapter 2 details the fundamentals of superconductivity and the important properties related to superconducting cables. Therefore, some basic and core properties of the materials used in the modelling of the HTS CORC cables are highlighted with the theories that support their usability. This chapter will similarly explore some literature reviews on the superconducting materials, especially focused on the second-generation (2G) HTS commercial wires. Moreover, cable technologies of HTS CORC cables are introduced with the strategies of development for each stage based on the recent technological topologies. Moreover, the existing modelling methods, including analytical methods, differential methods and integral methods, will be discussed. The need to involve theoretical formulations like the H-formulation, A-V formulation and T-A formulation is also introduced in this chapter. After modelling techniques,

the structural application of the developed models is elaborated to expose the aim and objectives of the research.

Chapter 3 major covers the AC loss calculation and analysis (including the transport loss and the magnetization loss) of the CORC cable, mainly by the means of 3D modelling using T-A formulation in COMSOL Multiphysics. Firstly, the T-A formulation will practically be introduced and applied to a 3D CORC cable model. Additionally, this chapter rate the assumptions of the T-A formulation based on the implementation of different modelling methodology on 2D HTS CORC cable models. The validation and comparison of the two 2D models will be achieved. Validation of the 3D T-A model is conducted by comparing the calculated AC losses with the experimentally validated data. Two multi-layer CORC cable samples are proposed and their AC losses are studied using this 3D T-A models. Finally, three novel 2D T-A models are proposed. Simulation results obtained from these models are compared with that from the 3D models.

Chapter 4 presents a thorough numerical study on the quench behaviour of HTS CORC cables. First part of this chapter introduces the mechanism of quenching with plenty of literature reviews. Then a multi-physics 3D quench model is proposed based on the T-A formulation. The multi-physics modelling methodology is explained in detail. After that, the influence of both the uniform and non-uniform terminal contact resistance on the quench behaviour of the CORC cable is studied using this 3D quench model.

Chapter 5 proposes a conceptual design of a 10 MW/3 kV/2 kA HTS tri-axial CORC cable to improve the propulsion system of hybrid-electric aircraft. A full cross-sectional 2D T-A based model is built for the three-phase delta-connected HTS tri-axial CORC cable. Also, taking advantage of the symmetry of the CORC cable, a 1/28 sector-shaped 2D T-A model is developed to simulate only a small sector of the cable's cross section. Both two models are used to calculate the AC losses of the cable with and without the existence of harmonic currents. Discussions are made to analyse the factors that affect the AC loss of the cable when both transport current and harmonic current are applied to the cable.

The last chapter, Chapter 6, concludes the research work where the future prediction of the HTS CORC cable will be presented based on the improvements that are gradually conducted on the HTS CORC cables.

1.4 The contribution of the thesis

The novel contributions of this thesis are as follow:

- A novel three-dimensional (3D) model is built based on the new T-A formulation for the simulation of multi-layer HTS CORC cable. The thin sheet approximation of T-A formulation successfully overcomes the modelling difficulties related to the high aspect ratio of the HTS wires. A two-dimensional (2D) H-based model is proposed as a reference model to validate a 2D T-A CORC model, proves the feasibility of the T-A formulation. Then, the 3D model is validated using experimental data obtained from other research groups. Accurate AC losses, including the transport loss and the magnetization loss, are calculated. To provide even better efficiency, three novel 2D T-A models are proposed with significantly shortened computation time. The most accurate AC losses, current distribution and field distribution are calculated from the Advanced 2D model and compared with the 3D model. The 3D and 2D model proposed here can be used to thoroughly study the electromagnetic behaviours of the multi-layer CORC cable. It can also be extended to simulate other superconducting devices with complex geometry.

- Efficient 3D multi-physics quench model of a single-layer CORC cable is presented based on the T-A formulation. It is the first-ever 3D multi-physics model that coupled four modules; the T-formulation, the A-formulation, the heat transfer module, and the equivalent circuit module, together to accurately simulate the whole process of hotspot-induced quench in an HTS CORC cable constructed using 3 ReBCO tapes. Multi-physics properties of this quench model are introduced in detail. The influence of the uniform and non-uniform terminal contact resistance (TCR) on the quench behaviour of CORC cable is studied. We further calculate the minimum quench energy (MQE), finding that the tape with moderate value of TCR is the most stable one during a quench, while the tape with the lowest TCR has the worst thermal stability.

- Conceptual design of a 10 MW/3 kV/2 kA HTS tri-axial CORC cable for the propulsion system of hybrid-electric aircrafts. Three delta-connected phases of the cable are concentrically arranged. Each phase contains 28 ReBCO tapes. A full cross-sectional 2D T-A model is proposed for this tri-axial CORC cable. Then, due to the fully symmetric geometry of the cable, a 1/28 sector-shaped 2D model is proposed to simulate only a small sector of the cable's cross section. The simulation results of these two models are compared. Influence of the harmonic currents on the magnetization AC loss of the cable is analysed.

Chapter 2. Superconductivity and superconducting cable

2.1 Fundamentals of superconductivity

2.1.1 History of superconductivity

The phenomenon of superconductivity was discovered by a Dutch physicist, Heike Kamerlingh Onnes, in the year 1911. The electrical resistivity of solid mercury dropped to zero at a temperature just below 4.2 K [24]. The zero resistance is one of the properties of a superconductor. Following this notable milestone, several materials, most of which are elemental metals (such as iron, lead and tin), were discovered to exhibit superconductivity at temperatures below 30 K [25]. These materials are classified as 'low temperature superconductors' (LTS). However, limited by the low value of the critical magnetic field, the LTS materials were not suitable for being widely applied to electrical applications. By 1986, Georg Bednorz and K. Alex Muller discovered that the copper-based compound (cuprate) revealed superconductivity under relatively high temperature (around 35 K) [26, 27]. Shortly after, the discovery of Yttrium Barium Copper Oxide ($YBa_2Cu_3O_7$) broke the temperature limit of liquid nitrogen (77 K), with its critical temperature reached the value of 93 K [28]. Materials with high superconducting temperatures are then classified as 'high temperature superconductors' (HTS), which have renewed research interest for reaching room temperature superconductivity.

2.1.2 Characteristics of superconductors

2.1.2.1 Working conditions of superconductor

Ever since the discovery of superconductivity, tremendous ongoing research activities have been carried out to characterize the physical properties of superconductors. A superconductor only enters the superconducting phase under certain working conditions. The vanishing of the resistivity in a superconductor occurs below a certain temperature, which is called 'the critical temperature' or 'the transition temperature' (T_c). This quantity, along with the other two factors,

the critical magnetic field (H_c) and the critical current density (J_c), defines the superconducting region of a superconductor. Figure 2.1 presents the 'critical surface' in 3-dimensional space for a superconductor. Limited by the maximum values of T_c, H_c and J_c, a superconductor only remains superconductivity within the boundary of the critical surface. These critical values are interdependent on each other. Once one of them reach beyond its critical value, the superconductor enters the normal conductor state. Thus, the critical surface in Figure 2.1 represents the working conditions of superconductors.
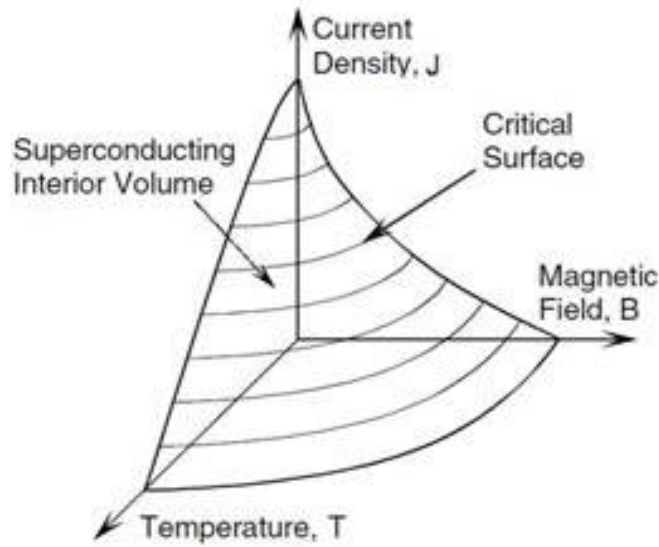
Figure 2.1 The critical surface of a superconductor [29].

2.1.2.2   The Meissner Effect

According to Posen *et al.* (2016), when operating under superconducting state, the superconducting materials expel magnetic flux within them [30]. This property has been critical in the naval forces, and other power applications since the charge generated can cause an explosion as a result of the charging mechanism within the two conductors. A good example is landmines that are charged by electric current underneath water bodies, causing serious damages and loss of lives when such strategies occur. Majorly, the defect of self-generation of currents by the superconductors is referred to as the Meissner Effect [31]. According to Kruger (2017), Meissner Effects are caused by constraining forces within metals, generating charges that are introduced to the surrounding area [32]. Thus, Figure 2. 2 indicates the magnetic flux

criteria in the superconductors. Known as the most essential physical property of superconductors, the Meissner Effect shows that, when a superconductor is set in an existing steady-state magnetic field with a temperature lower than its transition temperature (T_c), the magnetic flux inside the bulk of superconductor is fully expelled from its interior [33, 34]. However, this phenomenon is normally misunderstood as 'perfect conductor'. The difference in these two concepts are visually presented in Figure 2. 3. For a perfect diamagnetic conductor, if there is a steady magnetic field through its interior, after being cooled down to a zero-resistance state, the magnetic field should theoretically remain the same as before. A superconductor, on the other hand, will immediately exclude any magnetic flux once it enters superconducting state.
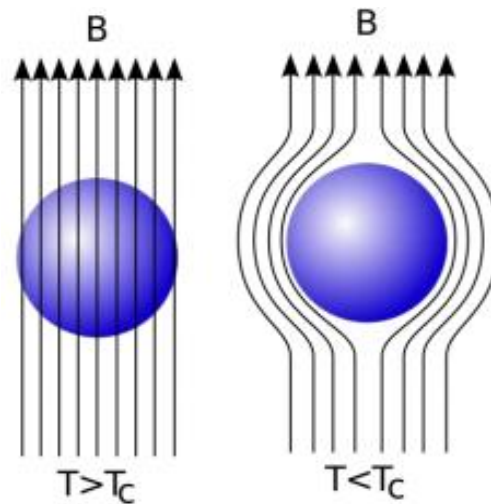
Figure 2. 2 Diagram of the Meissner Effect of superconductors [35, 36].
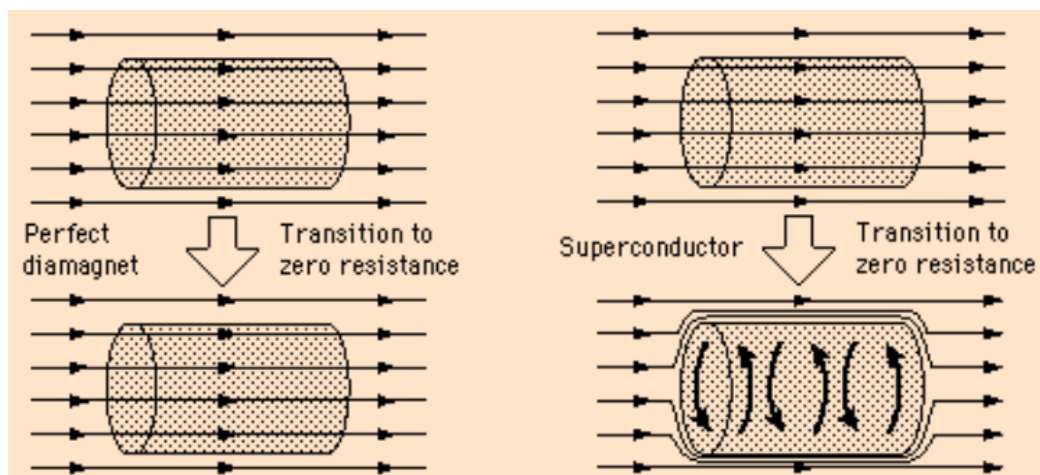
Figure 2. 3 Difference between a perfect diamagnet and a superconductor [37].

12

2.1.2.3 London equations and penetration depth

The London brothers, Fritz and Heinz London, mathematically explained the Meissner Effect in 1935. The Ohm's law is well known as the constitutive relation for a normal conductor. Similarly, the London equation is the simplest constitutive relation for the superconducting current and the magnetic field of a superconductor. These equations assume that the current density J of a superconductor is proportional to the vector potential A. Definition of this vector potential is as follow,

$$\begin{cases} \mathbf{B} = \nabla \times \mathbf{A} \\ \nabla \cdot A = 0 \end{cases}$$

Equation 2. 1

The London equation is then given by,

$$\mathbf{J} = -\frac{1}{\left(\mu_0 \lambda_L^2\right)} \mathbf{A}$$

Equation 2. 2

Which can also be written as,

$$\nabla \times \mathbf{J} = -\frac{1}{\left(\mu_0 \lambda_L^2\right)} \mathbf{B}$$

Equation 2. 3

The λ_L here represents the 'London penetration depth'. It is the characteristic length in superconductors [38]. It shows the distance that is necessary for the magnetic field of a superconductor to decay to 1/e times the applied external magnetic field [39]. Its expression is as follow,

$$\lambda_L = \sqrt{\frac{m}{\mu_0 n q^2}}$$

Equation 2. 4

Here, n is the superconducting electron density, while m is the mass and q is the electric charge.

Using following Maxwell's equations,

$$\nabla \times \mathbf{B} = \mu_0 \mathbf{J}$$

Equation 2. 5

Combined with the vector calculus identity,

$$\nabla \times \nabla \times \mathbf{B} = -\nabla^2 \mathbf{B}$$
Equation 2. 6

Rewritten Equation 2.3 can express the Meissner Effect from London Equation as follow,

$$\nabla \times \nabla \times \mathbf{B} = \nabla \times (\mu_0 \mathbf{J}) = -\frac{\mathbf{B}}{\lambda_L^2}$$
Equation 2. 7

$$\nabla^2 \mathbf{B} = \frac{\mathbf{B}}{\lambda_L^2}$$
Equation 2. 8

By the definition of Maxwell's equations,

$$\nabla^2 \mathbf{B} = 0$$
Equation 2. 9

The value of $\mathbf{B}$ at the interior of superconductor needs to be zero. The only exceptional case is that the London penetration depth is infinite, which means the conductor is no longer a superconductor. This explains the Meissner Effect of the superconductor.

2.1.2.4   The V-I curve for superconductors

For a practical superconducting wire, the transition from the superconducting state to the normal-conductor state occurs gradually [40, 41]. The critical current I_c of a superconductor is explained as the flowing current at which the voltage drop along the length of a superconducting wire is larger than the critical electric field E_c. Value of E_c is normally 1 µV/cm at 77 K under self-field. The self-field is referred to the magnetic field that is induced by a flowing current in the superconducting wire under operation. Figure 2. 4 gives the basic V-I curve. The N-value in the graph represents the relationship between the voltage drop on the length of wire and the transport current flowing in the wire.

The V-I curve can be calculated using following power law,

$$E(I) = E_c \left(\frac{I}{I_c} \right)^N \qquad\qquad \text{Equation 2. 10}$$

Here $E(I)$ represents the voltage drop along the length of the superconducting wire as a function of its applied transport current. $E_c = 1$ µV/cm. I is the transport current in the superconductor, while I_c is the critical current. N value defines the exponent of the transition of superconductors, which also presents the quality of the superconducting materials. Higher N-value means better quality of superconductor. For instance, the ReBCO tape used in this research, the 4 mm ReBCO tape produced by SuNAM has the *n*-value of 30.5 [43].

The critical current density J_c is calculated from the measured critical current I_c by dividing it by the cross-sectional area of the superconductor. In practical applications, however, the engineering critical current density J_e is more often used as a vital quantity of superconductors. This value is obtained by dividing I_c using the cross-section of the whole wire, including the superconducting area and the normal conductor area [42].

2.2 Classification of superconductivity

These are basic considerations for a superconductor that introduces and highlights the behaviours of the two main classifications of superconductors; the Type I superconductor and Type II superconductor. According to Rey and Malozemoff (2015), the type I and type II superconductors differ in their capability of corresponding magnetic behaviours and temperature [38]. Base on the classical theory, the superconductivity process fails in explaining the in-depth understanding of the source and discovery of superconductivity in a detailed manner.

2.2.1　Type I superconductor

Type I superconductors can also be referred to as low-temperature superconductors. They are also formerly named as soft superconductors. The Meissner Effect applies perfectly to this type of superconductors. They are superconducting materials that shows a total magnetic flux

expulsion in the interior during superconducting state. Figure 2. 5 gives a basic magnetization curve for Type I superconductors. Notice that when $B = 0$ (or $M= - H$), the Type I superconductor shows a full magnetic flux expulsion. Here M is the magnetization of the superconductor. When $H = H_c$, the transition is reversed abruptly.
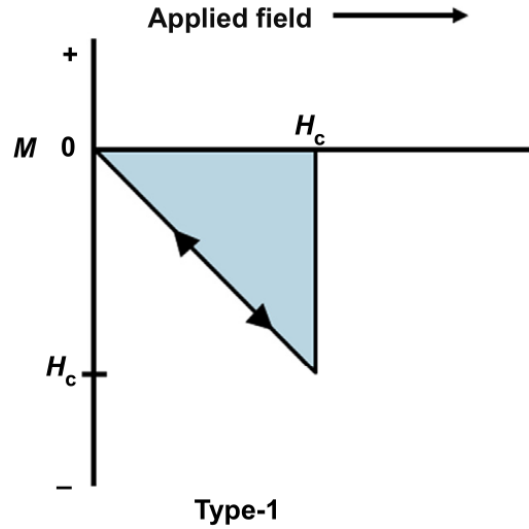
Figure 2. 5 The typical magnetization curve for Type I superconductors [38].

Most of the Type I superconductors are made of pure metals such as aluminium, indium, mercury, lead, tin, etc. For a type I superconductor, there is one and only one upper limit of the magnetic field, which is the critical magnetic field H_c. Its corresponding current density is the critical current density J_c that is mentioned before. H_c varies with the temperature of superconductors. The decrease in temperature leads to increase of H_c. Similarly, with the temperature increased to its critical value T_c, the value of H_c drops to zero. The critical temperature of a type I superconductor usually ranges from 0 K to 10 K with a critical magnetic field of a range of 49 μT to 1 T. Meanwhile, the critical current density J_c also has this temperature dependence. The criterion of critical current density J_c for Type I superconductors is quite low, which significantly limits their potential of being applied to electrical power applications in which high transport current is in urgent need.

2.2.2 Type II superconductor

Magnetic behaviour that differs from the Type I superconductors were first observed in Alloys and several impure metals. Abrikosov (1957) proposed a brand-new type of superconductor in

1957, which he claimed that has a completely different physical properties with the Type I superconductors. This type of superconductors is called hard superconductors, and is later called Type II superconductors.

One highlighted difference between Type I and Type II superconductors is that, the Type II superconductor only partly obeys the Meissner effect. There is a 'mixed state' between the superconducting state and normal state. Figure 2. 6 shows the transition process from superconducting state to normal state for Type I and Type II superconductors respectively.

Type I superconductor   Type II superconductor
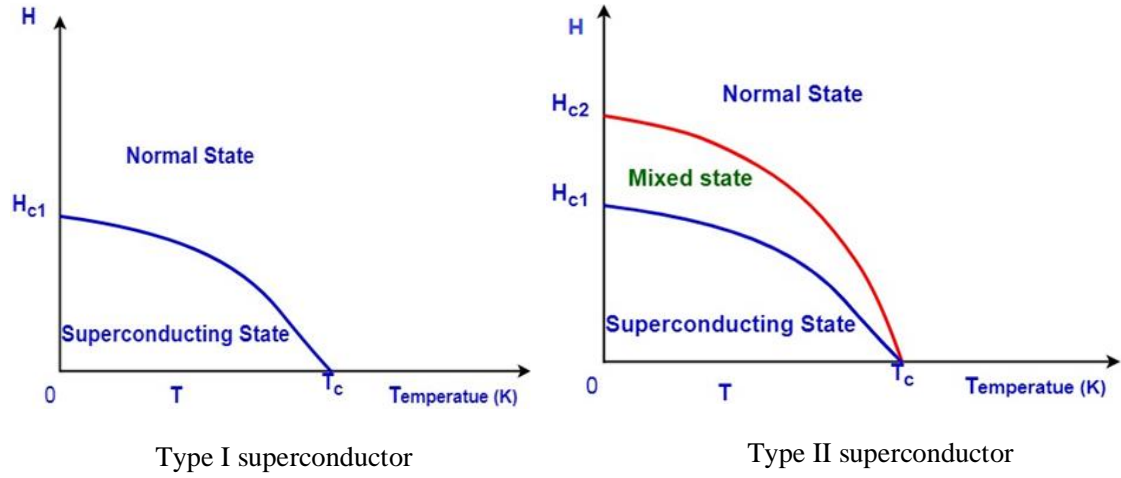
Figure 2. 6 Different operating states in Type I and Type II superconductors.

From the graph, the Type II superconductor has two magnetic field thresholds, the lower critical magnetic field H_{c1} and the upper critical magnetic field H_{c2}. The magnetic field in the interior of a Type II superconductor is completely expelled when the magnetic field is below the lower limit H_{c1}, so that the superconductor is operating in its superconducting state. When the applied magnetic field is above the upper limit H_{c2}, the superconductor loses superconductivity and can only work in its normal state. However, for the case when $H_{c1}<H<H_{c2}$, the Type II superconductor transits into the mixed state. In this state, the magnetic flux lines partially penetrates to the bulk of superconductors as quantized vortex lines (or vortex filaments) [44]. This means that when a superconductor is at mixed state, it is divided into two domains, the alternating normal domain and the superconducting domain. Every vortex line comes with a normal core that can be considered as a long cylinder. Axis of these cores are parallel to the external magnetic field. A persistent supercurrent is generated by the vortex to

circulate around the normal conductor core, generating magnetic field that has the same direction with the external field [45]. This partial penetration of the external magnetic field in the interior of Type II superconductors is defined as the 'mixed state'. The magnetization curve of Type-II superconductors is given in Figure 2. 7 as a comparison to the curve of Type-I superconductors in Figure 2. 5.
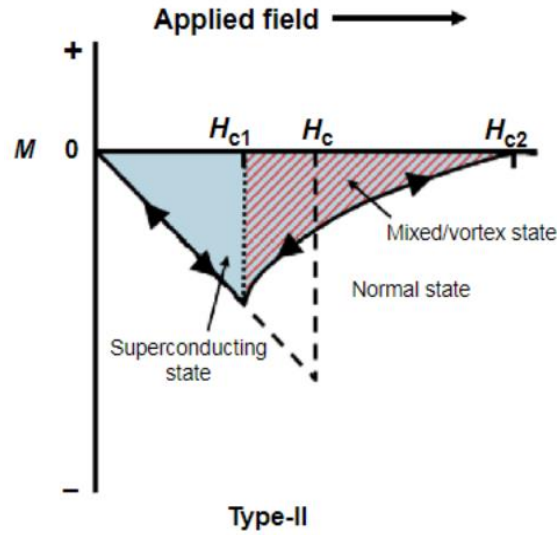
Figure 2. 7 The typical magnetization curve of a Type-II superconductor [45].

2.2.3 Low temperature superconductor

There is no specific cut-off temperature between the low-temperature superconductors (LTS) and the high-temperature superconductors (HTS). The general idea of defining an LTS material is to see whether it follow the classical Bardeen-Cooper-Schrieffer (BCS) theory or not. The BCS theory was first proposed by John Bardeen, Leon N Cooper and John R Schrieffer in the year 1957 [46]. Basic conceptual element of the BCS theory is the coupling of electrons into Cooper pairs against the Coulomb repulsion under a certain temperature, typically below 30 K [47]. The critical temperatures and critical magnetic fields of some LTS materials are listed in Table 2. 1. Most of the LTS have low critical temperatures, no larger than 30 K. One exception, however, is the binary compound MgB_2, which has a critical temperature around 39 K. This criterion is even higher than some of the HTS materials. Judging from the electron-pairing mechanism of MgB_2, it should be classified into LTS. However, based on its relatively high critical temperature, it is also included in the HTS classification in some of the published papers.

Table 2. 1 T_c and H_c of LTS materials

Materials	Critical temperature T_c	Critical magnetic field H_c
Titanium (Ti)	0.40 K	5.60 mT
Aluminium (Al)	1.18 K	10.5 mT
Indium (In)	3.41 K	28.1 mT
Zinc (Zn)	0.85 K	5.40 mT
Mercury (Hg)	4.15 K	41.1 mT
Lead (Pb)	7.19 K	80.3 mT
Tantalum (Ta)	4.50 K	83.0 mT
Nb-Ti (Alloy)	10.20 K	15.0 T
Nb_3Sn	18.30 K	30.0 T

Though tremendous development has taken place in the field of HTS materials, most of the commercially used superconductors are still LTS materials. Two representative LTS materials used in the industrial market are NbTi and Nb_3Sn. Use of NbTi benefits from its simple crystal structure, as can be seen in Figure 2. 8. There is no determined position for Nb and Ti. The NbTi wire is easy to fabricate with excellent ductility. Several examples of monolith NbTi wires are given in Figure 2. 9 with different shapes and various filaments numbers. The low cost also contributes to one of its advantages for being applied to commercial applications such as magnetic resonance imaging (MRI), nuclear magnetic resonance (NMR) and high energy magnets [38].
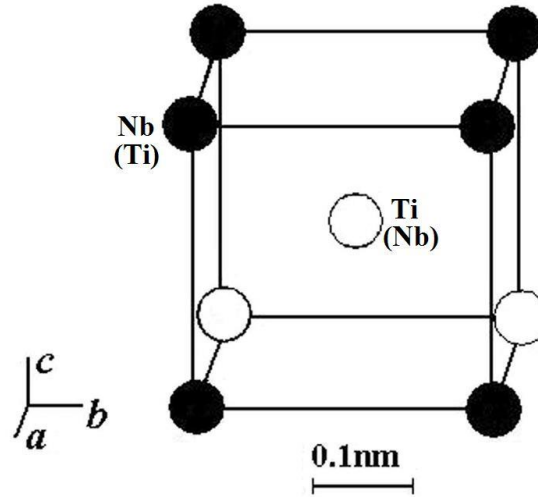
Figure 2. 8 The crystal structure of NbTi alloy [48].

| (a) | (b) | (c) |
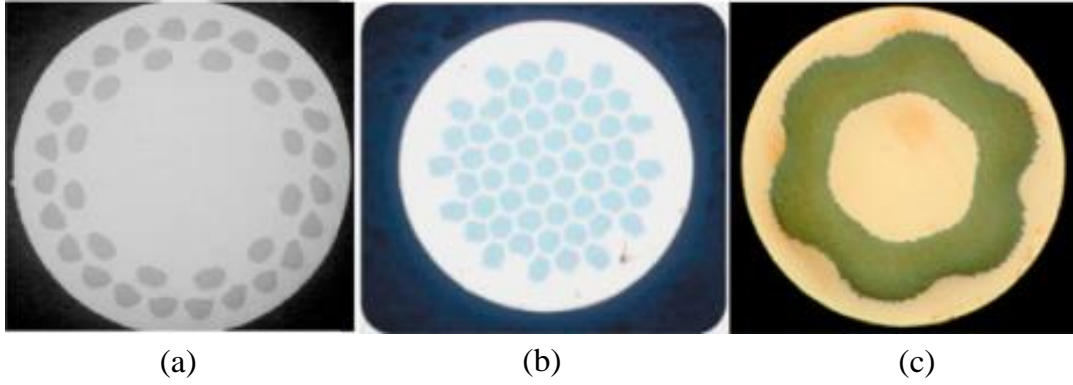
Figure 2. 9 Cross sections of monolith NbTi wires with (a) 36 filaments; (b) 55 filaments; and

(c) 2616 filaments [49].

Figure 2. 10 presents the crystal structure of Nb_3Sn. The Sn atom is centred in the interior a cubic with two Nb atoms cantered on every surface of the cubic. This structure is fragile and sensitive to mechanical strain, which makes Nb_3Sn a harder material to work with, compared with the NbTi wires. Cross sections of two Nb_3Sn wires with the same tube but different numbers of filaments are given in Figure 2. 11. The Nb_3Sn wire is widely implemented on applications such as high-field magnets and fusion magnets.
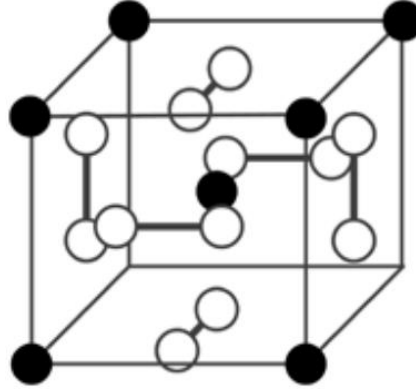
Nb - in white; Sn - in black.

Figure 2. 10 The crystal structure of A 15-type Nb$_3$Sn [50].
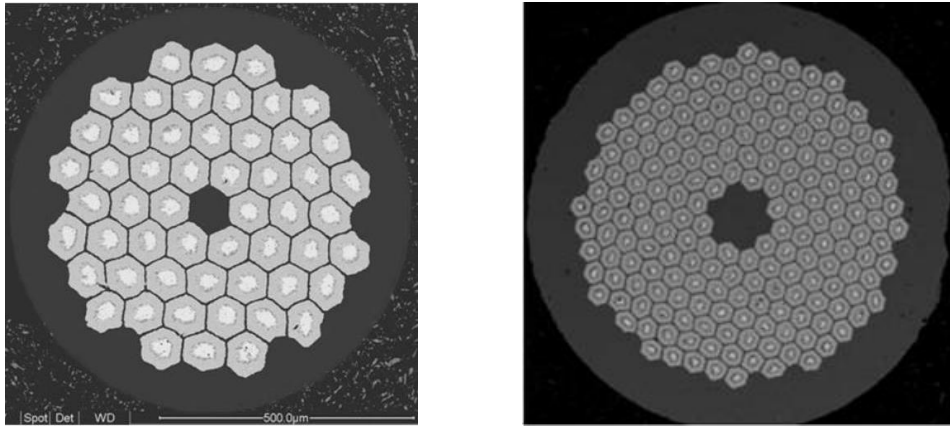
Figure 2. 11 Cross sections of two different Nb$_3$Sn wires.

MgB$_2$ has the highest transition temperature, T_c=39 K, among all pure metallic superconductors. Its simple hexagonal crystal structure is presented in Figure 2. 12. Despite of its unusually high critical temperature T_c, the large anisotropy of MgB$_2$ still limit the bulk current density to a relatively low level [51]. Moreover, coupling between grain boundaries is weak, making the transport current density in the samples highly sensitive to external magnetic field. Thus, it is still clarified as low temperature superconductor, as its electronic properties are strongly fit the classical BCS theory. MgB$_2$, having high T_c and high H_{c2}, rises widely commercial interest for easily fabricating it into wires with relatively low cost. The powder-in-tube (PIT) approach is adapted to fabricate MgB$_2$ wires. Figure 2. 13 shows the cross section of a basic multi-filamentary MgB$_2$ wire fabricated using the PIT approach. Though MgB$_2$ wires have drawbacks such as the low irreversibility field (B_{irr}, the magnetic field where the transport current density J_c becomes zero) and the large inherent anisotropy,

21

this type of wire still has obvious advantages in terms of low production cost and classical, easy fabrication route [52]. This type of wire has been used in many electric power applications, such as AC/DC power cables, transformers, fault current limiters (FCLs), motor and generators, etc.
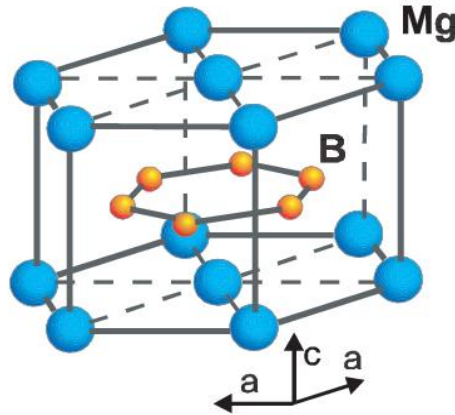
Figure 2. 12 The crystal structure of MgB$_2$ [53].
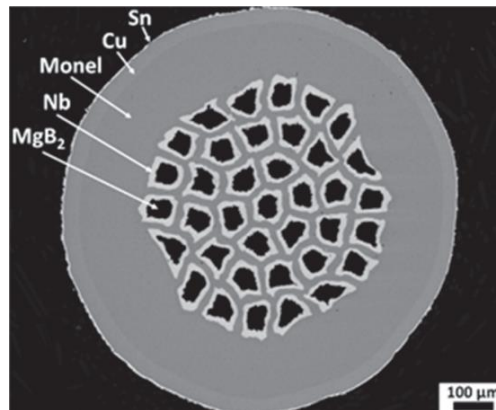
Figure 2. 13 Cross section of a multi-filamentary MgB$_2$ wire [54].

2.2.4   High temperature superconductor

The amazing discovery of high-temperature superconductivity (J.G Bednorz and K.A. Mueller, 1986) indicated that the worldwide research of superconductivity officially entered a new age [27]. The high-temperature superconductivity was firstly found in a series of materials with critical temperature ranges from 35 K to 40 K. Later in 1987, following the footsteps of Bednorz and Muller's work, Yttrium barium copper oxide (YBCO) with a transition temperature of 93 K was discovered. This transition temperature is obviously above the boiling point of liquid nitrogen (77 K) [55]. The ReBCO family was the first to be found with T_c values higher than

77 K. The rare earth elements, having similar atomic structures with yttrium, are substituted for Y and are referred to as rare-earth barium copper oxide (ReBCO). The Bi-Sr-Ca-Cu-O (BSCCO) system was discovered by Maeda *et al.* (1988) and Tallon *et al.* (1988) with even higher transition temperature, i.e., T_c = 120 K for BSCCO-2223 [56, 57]. In the same year, Z. Z Sheng and A.M. Hermann (1988) found that the Tl-Ba-Ca-Cu-O system reaches a transition temperature of 125 K [58]. By far, the highest T_c values among all materials is obtained in the Hg-Ba-Ca-Cu-O system. A. Schilling et al. (1993) found superconductivity in Hg-1223 at around 133 K under ambient pressure. This value reaches around 160 K under high pressure [59].

2.2.4.1   Anisotropy of high-temperature superconductors

The basic definition of the anisotropy of the HTS conductors is as follow; the critical current I_c depends on both the magnitude and direction of an applied external magnetic field. During the design and manufacture of a superconducting device, the anisotropy should always be considered with care.

There are two factors affecting the anisotropy; the layer structure of the YBCO materials, and the grain boundaries. The former factor is an intrinsic physical property of the YBCO conductors. Thus, the influence of the grain boundaries on anisotropy of superconductor gains more research interests. Strong anisotropy of the critical current J_c may cause problems in electric power applications, as I_c doesn't depend only on the temperature and magnetic field of the superconductor. The direction of the external magnetic field also affects the I_c. A numerical model was proposed by Meer *et al.* (2001) to study the angular dependence of I_c (T, H, θ) in a Bi-2223 superconducting tape [60]. By assuming that the external magnetic field perpendicular to the conductor surface is the only dependent factor for I_c of the tape, this model is suitable for analysing the I_c behaviour of the superconductor under magnetic field in all directions. In the same year, T. Kiss *et al.* (2001) developed a theoretical *E-J* model to analyse the strength and distribution of pinning, as well as the angular dependence of Bi-2223 tapes [61, 62]. These studies together provide a rough and theoretical study on the property of anisotropy.

The Kim-Anderson model, on the other hand, gives more detailed explanation of anisotropy from the real engineering perspective [63-65]. The dependence of I_c on the magnetic field can be expressed as follow,

$$I_c(B) = \frac{I_{c0}}{1 + \dfrac{B}{B_0}}$$

Equation 2. 11

Here, I_{c0} represents the critical current under self-field, while $I_c(B)$ is the critical current of which value relies on the magnetic field B. B_0 is a fitting variable. This equation only suits for superconductors with isotropy. For those with anisotropy, the angular dependence on I_c needs to be considered in the equation as well. Thus, the magnetic field in Equation 2.11 is decomposed into parallel and perpendicular fields;

$$\begin{cases} I_c(B, \perp) = -\dfrac{I_c}{1 + \dfrac{B}{B_{0\perp}}} \\[4ex] I_c(B, \|) = -\dfrac{I_c}{1 + \dfrac{B}{B_{0\|}}} \end{cases}$$

Equation 2. 12

$B_{0\perp}$ and $B_{0/\!/}$ in these two equations have similar use with B_0 in Equation 2.11. They are the fitting parameters for perpendicular and parallel magnetic fields respectively. However, it is not enough to just study the anisotropy on two specific directions. The calculation of the critical current under all magnetic field orientations should be obtained. Thus, a new theory, which is called the 'effective mass model', was proposed by G. M. Zhang *et al.* (2003) [66]. This model gives an assumption that, when the external magnetic field H is far away from the c-axis, H can be effectively assumed as a magnetic field $H_\perp{}'$ that is perpendicular to the ab-plane. m_a and m_b are used to represent the effective mass along a and b axes. Approximation is thus made as,

$$m_a = m_b = m_{ab}$$

Equation 2. 13

Then the effective $H_\perp{}'$ is given as,

$$\begin{cases} H_{\perp}^{'} = H\left(\sin^2\theta + \dfrac{1}{\gamma^2}\cos^2\theta\right)^{\frac{1}{2}} \\[4mm] \gamma = \dfrac{B_{0\|}}{B_{0\perp}} \end{cases}$$

<div align="right">Equation 2. 14</div>

γ here is the parameter that characterize the anisotropy of HTS materials. θ represents the angle between the orientation of the external magnetic field and the ab-plane. Normally, for the YBCO family, value of γ is between 5 to 7 [67]. For the BSCCO family, γ is always higher than 10 [68].

Next assumption is that the grains in the high-temperature superconducting tape are well aligned, which means I_c of this tape mainly relies on the magnetic field that is perpendicular to the tape surface [69, 70]. Combined Equation 2. 12 and Equation 2. 14, the relation between I_c and an arbitrary angle of magnetic field can be expresses as follow;

$$I_c(B,\theta) = \frac{I_c}{1 + \dfrac{B}{B_{0\perp}}\left(\sin^2\theta + \dfrac{1}{\gamma^2}\cos^2\theta\right)^{\frac{1}{2}}}$$

<div align="right">Equation 2. 15</div>

On the other side, if I_c only depends on the magnetic field that is parallel to the tape surface, then Equation 2. 15 is rewritten as;

$$I_c(B,\theta) = \frac{I_c}{1 + \dfrac{B}{B_{0\|}}\left(\sin^2\theta + \dfrac{1}{\gamma^2}\cos^2\theta\right)^{\frac{1}{2}}}$$

<div align="right">Equation 2. 16</div>

By using Equation 2. 15 and Equation 2. 16, the critical current under magnetic field with arbitrary angle can be calculated.

For most electric power applications, including the transformers, motors/generators, fault current limiters, etc., lower value of J_c may eventually result in higher current carrying capacity of the device, for the external magnetic field penetrates from all directions to the ab-plane of the superconducting tape [38]. Larger anisotropy of superconducting materials leads to lower J_c, which means more turns will be required in the superconducting magnet to equal with the number of ampere-turns. This negatively increases the mass, size and fabrication cost of the device. The superconducting cable, on the contrary, has different performance. A superconducting cable

generates a magnetic field during operation. The field it induced has small magnitude, and is orientated into directions that can carry maximal flowing current, which is the most favourable situation during the operation of electric power applications.

2.2.4.2 Practical HTS wires

Table 2. 2 T_c of HTS materials

Materials	Critical temperature T_c (K)
NbZr	11
NbGe	23.6
NbAl	19.1
$Bi_2Sr_2CaCu_2O_8$ (Bi-2212)	90
$Bi_2Sr_2Ca_2Cu_3O_8$ (Bi-2223)	110
$Pb_2Sr_2CaCu_2O_x$	122
$Tl_2Ba_2Ca_2Cu3O_{10}$(Tl-2223)	125
$HgBa_2Ca_2Cu_3O_8$ (Hg-1223)	135
$YBa_2Cu_3O_{7-x}$ (YBCO)	92

Table 2.2 gives the highest critical temperatures of several HTS material families. However, by far, only the BSCCO-2212, BSCCO-2223 and ReBCO superconducting materials are practically applied in fabrication of electric power applications at 77 K.

The BSCCO family is classified as first generation (1G) HTS materials. The powder-in-tube (PIT) method is used as the fabrication technology of this series of materials. Though the mature PIT technology has sufficient properties, wide usage of this technology is limited by the high fabrication cost. The PIT fabrication technology involves the usage of silver, which is unavoidably expensive. Silver is the essential and irreplaceable material that can be chemically compatible with the BSCCO materials. It can also permeate to oxygen under processing temperature. Silver is used as a sheath for BSCCO-2212 and BSCCO-2223. However, nearly 60 % of the cross-section of a BSCCO wire is consisted with silver, which leads to considerable

high fabrication cost. Also, with the existence of external magnetic field, performance of 1G HTS is not comparable with second-generation (2G) ReBCO tapes.

On the other hand, production of the 2G ReBCO conductors uses the coated conductors (CCs) architectures. It is a multi-layer technology that uses textured substrate for coating. Several layers, including a thin buffer layer (MgO, CeO_2, etc.) and a film of superconducting YBCO layer, are covered on a metallic layer (Ni alloy) [71]. Two basic configurations of the 2G HTS CCs are presented in Figure 2. 14. The nickel alloy layer is applied here as a depositing base for the buffer and superconducting layers. The buffer layer is applied to strain the metal atoms within the substrate rather than diffuse into the superconducting layer. The superconducting behaviour of the 2G HTS largely relies on the grain directions, which means it requires epitaxial growth. The epitaxial growth texture can be obtained by two fabrication techniques, the Ion-Beam-Assisted Deposition (IBAD) technique [72-74] and the Rolling-Assisted Biaxially Textured Substrates (RABiTS) technique respectively [75, 76]. The final superconducting properties of the CCs are highly related to the thin film deposition technique for the superconducting layers of the tape. Several thin film deposition techniques, including the Pulsed Laser Deposition (PLD), Metal Organic Chemical Vapor Deposition (MOCVD), and Metal Organic Deposition (MOD) have been used widely by industry [77]. The coated conductors approach greatly improves the irreversibility behaviour of the YBCO conductors under high-field situation or at high temperatures. Besides, since fabrication of the CCs only requires very little Ag, it reasonably reduce the fabrication cost of the 2G HTS tapes/wires.

Unlike the theory of low temperature superconductivity, which can be described as the interaction between electrons in crystal lattice, the mechanism of high temperature superconductivity remains a mystery. The complicated crystal structure of $YBa_2Cu_3O_7$ is presented in Figure 2. 15. Copper-oxygen planes and copper-oxygen chains can be observed in the crystal structure of YBCO materials. Planes of CuO_2 separate the perovskite structure layers. Yttrium atoms are centred between the copper-oxygen planes. Oxygen atoms bridge copper atoms into square lattices to form the planes. Barium atoms are located between the parallel copper-oxygen planes and the chains of CuO. Variation of the oxygen content of YBCO materials leads to considerable changes on its physical properties [78].
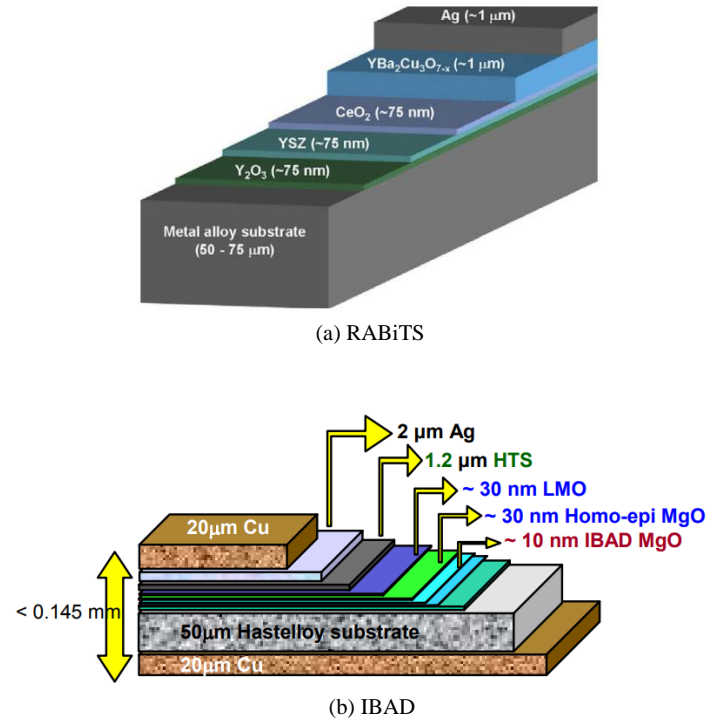
(a) RABiTS

(b) IBAD

Figure 2. 14 The configuration of second-generation coated conductors constructed using (a)

RABiTS technique; and (b) IBAD technique [72].
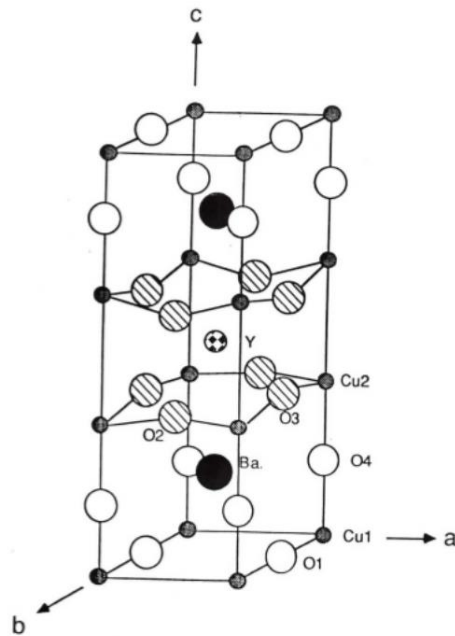
Figure 2. 15 The crystal structure of YBCO [78].

2.3 2G HTS cables

Superconducting cables are one of the most promising candidates to be applied to power systems, for superconducting cable systems are considered to be more efficient than equivalent resistive cable systems [79]. Superconducting DC cables, with a compact structure that requires less spaces, are easier to be installed underground, compared with conventional transmission lines. Thus, superconducting DC cables have higher security and reliability. In the 1960s, Garwin and Matisso analysed a multi-gigawatt superconducting DC power cable [80]. Following their footsteps, the Los Alamos Scientific Laboratory developed a cable using low-temperature superconductors for DC power transmission [81, 82]. Then, with the development of high-temperature superconductors, the Electric Power Research Institute (EPRI) started a project to develop an HTS DC power transmission system [83]. In 2005, EPRI carried out a study on two intraregional DC cable. One of the intraregional DC cables was rated at 2 GW with a length of 200 km, while the other one was rated at 10 GW with a length of 1000 km [84, 85]. However, with the increase of the voltage level in recent power applications, the considerable amount of losses generated during the operation of high voltage DC power transmission (HVDC) eventually led to the development of high voltage AC power transmission (HVAC). Moreover, the operating voltage of a DC power cable is restricted to no more than 10 kV within areas with high population density. This also limits the use of HVDC superconducting cables [3]. On the other hand, superconducting AC cables, which can operate at low voltage levels, have high current densities but requires only small passageway, have become a promising solution for applications that require high power at low operating voltages. In other words, the superconducting AC cables can be a powerful candidate for power transmission in the electric aircraft.

In recent two decades, Rare-Earth (Re) based 2G HTS cables have been commercially applied to various industrial and scientific power applications [86]. Compared with the conventional cables, or even with the bismuth-based 1G HTS cables, the 2G HTS cables have advantages including high mechanical strength, high engineering critical current density, high irreversible field, etc. They are also able to carry electric power that is 3 to 5 times than conventional power cables [87]. Also, due to its lower transmission loss and higher current-

carrying capacity, the 2G HTS cable becomes a powerful and trustworthy candidate for applications involving power transmission and distribution. The focus point now is to propose a reliable, stable manufacturing process for the production of 2G HTS cables with low cost but high performance [88]. There are currently several superconducting cables that have been developed.

2.3.1 ROEBEL cable

The Roebel cabling concept was first proposed by Ludwig Roebel *et al.* in 1914. It is a low-loss copper cable which is wound by multiple insulated strands with full transposition. It was the first cabling concept that implementing the segmentation of the ReBCO conductors to insulate strands from each other. This cabling method also reduces the generated eddy currents and related current loops by achieving the full transposition of tape strands. The Siemens Corporate Technology group demonstrated the first high temperature Roebel cable constructed with 13 BSCCO-2223 tapes as strands [89]. The self-field reduced DC transport current of this cable was around 400 A @ 77 K, which was as expected. The Roebel cabling concept was thus applied to improve the design and fabrication of superconducting transformers [90].

In 1997, Martin Wilson *et al.* proposed the idea to fabricate the Roebel cable with ReBCO coated conductors (CCs) [91]. However, formation of the strand shape, bending technology, and assembling issue of the Roebel cable were still challenging at that time. A few years later, after the improvement of homogeneity and robustness of coated conductors, the zigzag shaping of the CCs was proposed by Karlsruhe Institute of Technology (KIT) in 2006 to deal with these problems [92, 93]. The Roebel bar made from CC tapes is presented in Figure 2. 16.
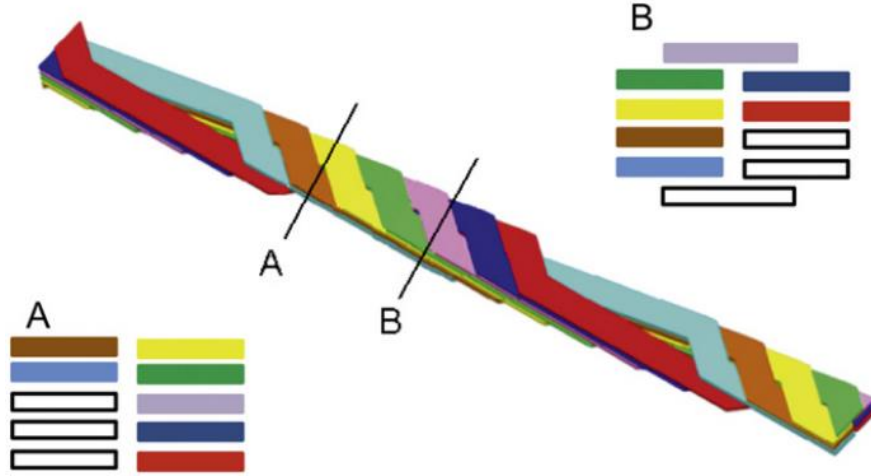
Figure 2. 16 Scheme of the Roebel bar made from CC tapes. A and B are the transversal cross sections at different positions of the bar [94].

The first Roebel cable was manufactured by the THEVA company. It was constructed with 16 punched DyBCO CC strands and carried a transport current of 500 A at 77 K under self-field, while the sum of the critical currents of each tape was around 1000 A [93]. However, due to the lack of copper stabilizer, this cable was damaged by the quenching occurred during the operation process. Then a stable operating Roebel-assembled coated conductor (RACC) cable was constructed using Superpower MOCVD-CC tapes and had two full transposition lengths. The DC transport current of this cable reached 1.02 kA at 77 K under self-field, which proved the reliability and stability of the Roebel cabling concept [95]. The third Roebel-assembled cable was a short sample made from THEVA-CCs [96]. An inter-strand connection was achieved by applying Ag-filled epoxy to connect the strands of the cable.

W. Goldacker *et al.* presented their RACC cables in 2008 [97]. They analysed four RACC cables with various numbers of strands (from 11 to 16) using both the SuperPower MOCVD-CC and THEVA TCE-CC. It was observed that the inhomogeneous high self-field caused degradation of the critical current of the RACC cable by around 30%, compared with the sum of critical currents of single tapes. The investigation verified the feasibility of reliable production and the possible extension in length of Roebel-assembled cables. The RACC concept was proved to be suitable for electrical power applications that require only a few kA AC transport currents.

Industrial Research Limited (IRL) developed automated machines to cut 40 mm wide YBCO strips into 2 mm wide strands for the manufacture of YBCO Roebel cables [98]. Since cutting YBCO strips into the zigzag Roebel shape causes inevitable loss of materials, cutting the widest possible YBCO tapes can effectively raise the rate of utilization of feedstocks. Mechanical punching of the machines managed to cut strips into 2 mm wide strands without losing current capacity.

The Roebel cabling concept enlarges the possibility to increase the transport current and the thermal or mechanical stability of the cable, simply by changing the geometry of strands constructing the cable. Further improved cabling method of threefold-layered strands was proposed in [99]. The 1.1 m long sample of a threefold-layered 45-strand Roebel cable with a transposition length of 18.8 cm investigated in this paper carried a transport current of 2.6 kA at 77 K in self-field. Another way to increase the current performance is to simply increase the transposition length of the cable to endure more strands.

The power cables used in electric aircraft propulsion systems need to be lightweight with the capability of transmitting high range of power in limited space. S. S. Fetisov *et al.* proposed the first 6 m long Roebel cable with transposition length of 226 mm for the aircraft propulsion systems [100]. The study showed that the AC loss of the Roebel cable was a bit higher than that of coaxial or tri-axial HTS cables. However, the light weight of Roebel cable still made it a powerful cabling method for on-board use in superconducting power systems in electric aircraft.

2.3.2 Twisted stacked-tape cable

Arranging ReBCO tapes in parallel can dramatically increase the current carrying capacity of a 2G HTS cable. However, this also leads to considerable AC losses generated by the magnetic flux coupling generated in the loop circuits among stacked ReBCO tapes, eventually influence the efficiency of power transmission of the cable. The twisting transposition technique was applied to overcome this problem [101].

In the year 2010, Makoto Takayasu *et al.* proposed that the 2G HTS tapes have great mechanical performance under torsion strains [102]. Thus, by twisting the stacked flat 2G HTS tapes along the axial direction of the stack, the so called twisted stacked-tape cable (TSTC) was developed. The

strain analysis for the critical current of TSTC cable was performed in [102]. The critical current degradation, current and inductance distributions among tapes, hysteresis loss, and the termination method for 2G HTS tapes, were studied in detail by Makoto's group [103-105]. Basic geometry of the TSTC cable as well as its cross section are presented in Figure 2. 17. As there is no former inside the TSTC cable, metals may be used as supporting structure as well as stabilizer to enclose the terminal of the cable [105].
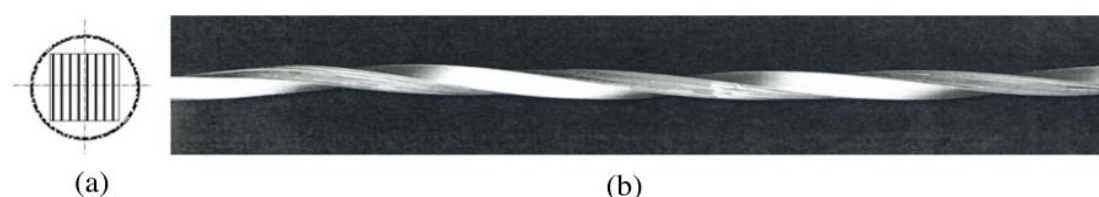
Figure 2. 17 (a) The cross section of stacked and twisted HTS tapes; (b) Basic structure of TSTC cables.

CERN tested the twisted-pair HTS cables carrying current of 1 kA [106]. The cables were tested under both LH_2 and LN_2 temperatures and showed no degradation. They also developed unique electrical joining techniques for this twisted-pair HTS cable. This investigation enabled the design and assembly of TSTC cables with long cryogenic lines.

The mechanical characteristics of TSTC conductors were investigated by L. Chiesa's group in 2014 [107]. Effects of transverse loads on the single ReBCO tapes and TSTC cables were analysed in detail for the understanding of their mechanical behaviours. Results show that, when the electromechanical Lorentz forces were much lower than averaged transverse loads, high current caused degradation of the critical current of TSTC cables.

In 2015, M Tomita *et al.* investigated a 2 m long TSTC cable that was wound by 32 YBCO tapes [108]. Critical current of the tested TSTC cable was 1.45 kA at around 77 K. This paper stated that controlling the operation equilibrium vapor pressure of LN_2 effectively improved the critical current of the cable. The highest critical current of the measured TSTC cable reached 3.65 kA at 64 K. The dependence of I_c of the cable on the temperature agreed well with a single YBCO tape with width of 4 mm.

A 40-tape TSTC cable constructed with SuperPower ReBCO tapes was experimentally analysed in [109]. It successfully carried current up to 6.0 kA at magnetic field of 17 T when the ambient temperature was 4.2 K. The Lorentz transverse load degradation of the cable was ignorable at the end of each cycle of the performed cyclic test. Thus, the TSTC cabling concept was proved to be suitable for magnet applications and power transmission cables that require high field and high currents. However, there was still 16 % of critical current discrepancy between the TSTC cable and the single ReBCO tape situations. Further evaluation of the conductor's mechanical performance in a Lorentz load environment was required.

2.3.3 Conductor on round core cable

High-field applications requires great electromechanical properties of conductors to endure high axial compressive strain. The YBCO CCs do not degrade easily under high field and high strain situation. Thus, the conductor-on-round-core (CORC) cabling method was proposed by D. C. Van der Laan *et al.* to be used in high-field magnetic applications with low AC loss [110]. By winding the YBCO CCs around a round former with small radius, the full transposition of the conductors is achieved. The basic structure of a CORC cable is given in Figure 2. 18.
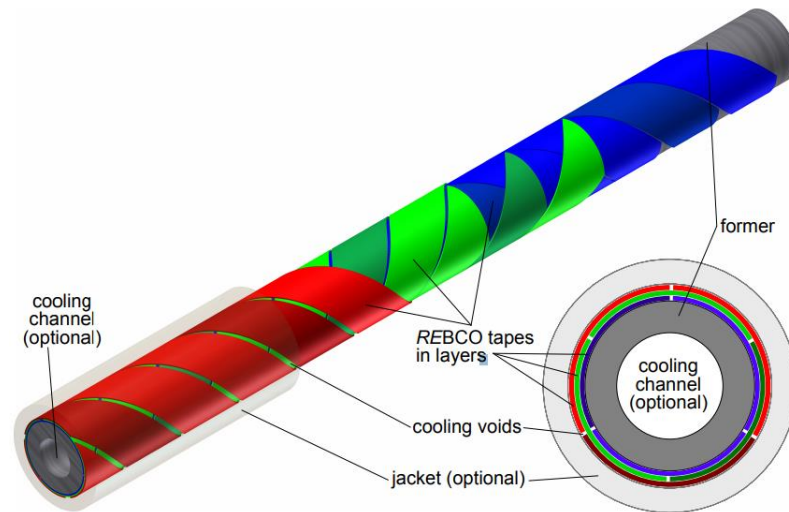
Figure 2. 18 Basic structure of a conductor-on-round-core (CORC) cable. The ReBCO tapes are helically wound on a round former (usually made from copper) with a relatively small diameter. Winding direction here is opposite between layers [111].

In this paper, six multi-layer CORC cable prototypes were presented and studied to prove the feasibility of this cabling concept. The YBCO tapes were tightly wound in compression on a brass former with an outer diameter of 3.19 mm. No irreversible degradation of the tapes was observed in any prototypes. I_c of the cables were calculated as a function of the length of the twist pitch. Based on the measurement, value of I_c was expected to reach 6.8 kA at 16 T in a 4.2 K magnetic field, which proved the feasibility of the CORC cabling method.

Based on previous study, Van der Lann *et al.* carried out an experiment on CORC cables in liquid helium (LH$_2$) in magnetic field of up to 20 T in 2013 [112]. At an ambient temperature of 4.2 K, the critical current of CORC cable reached 5021 A under a magnetic field of 19 T. The engineering current density J_e was 114 A/mm^2. It was the highest ever J_e for a superconducting power transmission cable under such a high magnetic field. Then, by using a 6m-long CORC cable, a 12-turn, double-layer magnet was built by Van der Lann's group. It was the first magnet that was wound from HTS cables. This magnet had an I_c of around 2 kA in the magnetic field of 20 T.

M Majoros *et al.* studied the magnetization losses in an AC magnetic field of several YBCO CORC multi-layer cables [113]. The cable analysed in this research has up to 40 YBCO tapes and up to 13 layers. The experiment was carried out under AC magnetic fields of up to 80 mT with frequencies between 50 to 200 Hz at 77 K. The influence of number of layers, helical geometry, and the applied direction of the external magnetic field on the variation of AC losses of CORC cables were studied in detail.

In 2015, the Institute for Technical Physics of the Karlsruhe Institute of Technology (KIT) characterized a 1.16m-long CORC cable sample, which was wound by 15 SuperPower ReBCO tapes with a width of 4 mm [111]. A five-step investigation was taken to fully analyse the performance of this CORC cable sample. The CORC cable carried a self-field current of 1638 A at 77 K, which only degraded by 14.38%, compared with the expected value. The self-field temperature dependence of the sample was measured between 42 to 77 K. The measured data agreed well with the predicted value. Under a maximal transverse Lorentz force of 31.4 kN/m, the sample's current carrying capability did not degrade at all. The dependence of the current carrying capabilities on the magnetic field and temperature agreed well with extrapolated data

of single ReBCO tapes given by their manufacturers, which proved that the field and temperature dependence of the CORC cable sample was identical with the constituent tapes. It also indicated that the current carrying capability of the tapes was fully achieved after being wound into CORC cables. No irreversible reduction of CORC cable sample's performance was observed during the five-step investigation, which successfully proved that the CORC cabling concept is a reliable and powerful candidate for transmission cables used in high-field applications.

2.4 Modelling methods

To design superconducting devices, numerous models have been developed in both analytical and numerical ways. Analytical methods are more often applied to models with simple geometries. It employs simple formulations to calculate certain magnetic fields, helping us to learn the basic electromagnetic behaviour of a given model. Although this method is fast and easy to apply, the constraint on the simple geometry still limits its application. Thus, for the tape configuration that is to be studied in this research, the numerical method is used, as it is more flexible and can be applied to more complex geometries.

There are mainly two classes of numerical methods for solving engineering problems involving continuum. The field approach, which adapts the element approximation for the partial differential equation (PDE) solutions, is the first numerical method. It is named as 'the differential method' in the following study. The second method uses Green's function. The source distribution is integrated to directly obtain the field. It is called 'the integral method' in the following study. In other researches, these two methods are also referred to as the PDE and integral equation (IE) methods.

One of the main assumptions of these modelling methods is to ignore the Meissner effect and only consider the mixed state. When the superconductor (generally refer to a type-II superconductor) is placed in an external magnetic field, an induced transport current flows through the surface of the tape, generating a magnetic field that is in the opposite direction with the external field to cancel the magnetic flux density in the interior of the superconductor. This field induced by the surface current for a type-II superconductor is called 'the self-field'. The

most difficult part in the simulation work of superconductors is how to calculate the current distribution using both the self- or external magnetic fields. There are several simulation methods to calculate the current distribution; the analytical method, the differential method, and the integral methods. A literature review of these methods is presented respectively in the following section.

2.4.1 Analytical methods

2.4.1.1 Bean's critical-state model

C. P. Bean was the first one to introduce the Bean's critical-state model that offers a macroscopic explanation of the hysteretic magnetization phenomenon of Type-II superconductors [114, 115]. For simplicity, consider an infinite slab in a uniform magnetic field, as can be seen in Figure 2. 19. As thickness of this slab is thin enough to be ignored, the magnetic field component perpendicular to the slab surface is negligible. Only the magnetic field component parallel to the slab surface is considered here. Figure 2. 20 presents the current density and magnetic field distribution of the slab. Assumption of this model is that the variation of electric field $\mathbf{E}$ induces a current density $\mathbf{J}$. Value of the current density is assumed to be a constant, J_c. Bean's critical-state model can be described using following equations,.

$$\begin{cases} J = \pm Jc & if \ |E| \neq 0 \\ J = 0 & if \ |E| = 0 \end{cases}$$

Equation 2. 17
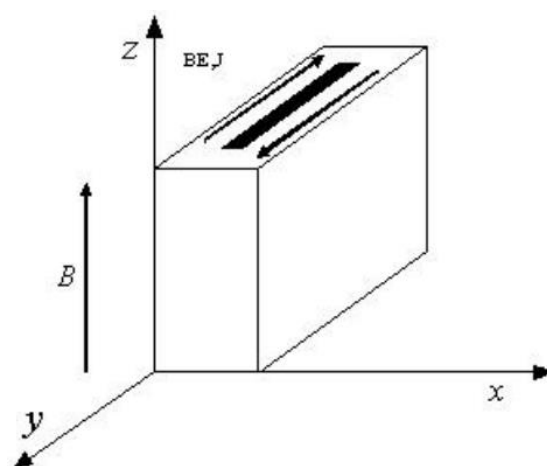
Figure 2. 19 An infinitely long slab in a uniform magnetic field [116].
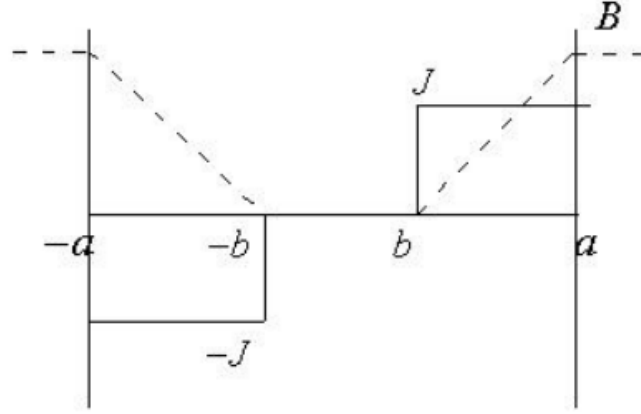
Figure 2. 20 The current density and magnetic field of an infinitely-long thin slab in an external magnetic field calculated by Bean's critical-state model [116].

However, since it is difficult to define the boundary between the critical and subcritical currents, the unknown boundary condition of Bean's critical-state model makes it hard to be applied to complicated systems [117].

2.4.1.2 Kim-Anderson model

Y. B. Kim, C. F. Hempstead and A. R. Strnad proposed a modification of Bean's model in 1962 [64, 118-120]. It is modified based on Bean's critical-state model and is named as 'The Kim-Anderson critical-state model'. This model studied the critical phenomenon of the type-II superconductors. It considered the critical current density J_c as a local variable rather than a constant value, which is more realistic. The value of J_c in this model is affected by both the external magnetic field and the surrounding temperature. Relationship between the critical current density J_c, the external magnetic field **B** and the ambient temperature T is expressed as follow,

$$\begin{cases} J_c(B,T) = \dfrac{k}{B_0 + B_l} = J_{c0}(T) \cdot \dfrac{1}{1 + \dfrac{B_l}{B_0}} \\ J_{c0}(T) = \dfrac{k}{B_0} \end{cases}$$

Equation 2. 18

Here B_l is the local magnetic flux density, both k and B_0 are the temperature-dependent parameters for the superconducting materials [121].

2.4.1.3   Norris' model for AC loss calculation

W. T. Norris proposed a method of calculating AC losses of type-II superconductors in 1969 [122]. This model employed the Bean's model, assuming that the critical current density J_c is a constant that is independent of magnetic field. The AC loss calculation equations obtained from Norris' research can be applied to tapes with cross-sections of rectangles, ellipses and circles. Since the CORC cable studied in this research uses ReBCO tapes, here give the AC loss calculation equation for a rectangle ReBCO tape;

$$Q = \mu_0 I_c^2 L_n \qquad\qquad \text{Equation 2. 19}$$

Here Q is the AC loss, I_c is the critical current of the tape. L_n is a parameter that depends on the transport current of the tape, it is called the loss factor. Value of L_n is listed in Norris' original paper.

However, due to the high width/thickness ratio (aspect ratio), the ReBCO tape needs a more precise formulation to calculate the AC loss. For this reason, Brandt improved Norris's calculation for single ReBCO tapes in [123]. He explained a new method to simultaneously calculate the current distribution of the tape when the current is changing. Calculation of the AC loss of a single ReBCO tape in Brandt's research is expressed as;

$$\begin{cases} Q = \dfrac{\mu_0 I_{max}^2}{\pi} f_n\left(\dfrac{I_0}{I_{max}}\right) \\ f_n(x) = (1-x)\ln(1-x) + (1+x)\ln(1+x) - x^2 \end{cases} \qquad \text{Equation 2. 20}$$

2.4.2   Integral methods

One of the main advantages of the integral equation methods is that there is no need to specify boundary conditions. It was applied to magnet design as well as to accelerator and Tokamak magnets, for this method helps to assess the influence of eddy current on the design of these devices [124]. Modelling of superconductors using integral methods is mainly about minimizing the magnetic energy in the superconducting domain. The integral method specifically defines the trying current distribution among the entire superconducting domain. The integrated parameters (including the magnetic flux density B and the magnetic vector potential A) are used to calculate the total energy within the superconducting area. Combined

with the mathematical optimization algorithms, the integral method can be used to characterize the optimal current distributions of superconductors.

By applying this method, John R Clem *et al.* (2007) estimated the AC losses of a finite stack of thin YBCO tapes [125]. He made two assumptions for the proposed numerical model. Firstly, each superconducting tape is anisotropic, homogenous and carries the same amount of transport current. The critical current penetrates the superconducting tape along its axial. The second assumption is Bean's approximation, which assumes that the penetration depth of each tape is independent of the magnetic field, i.e. is a constant.

Weijia Yuan *et al.* proposed a new model based on Clem's anisotropic homogeneous-medium approximation to calculate the AC losses, distribution of field and current, and value of I_c of HTS superconducting tapes [126, 127]. Instead of Bean's assumption, this model uses the assumption of Kim-Anderson model to allow the variation of critical current density, J_c, with the magnetic field, B. The model was verified with experimental results. Accuracy and computation speed were both improved by this new numerical method. Yuan's model was further modified to simulate superconducting coils with cylindrical geometry [126].

E. Pardo *et al.* [128, 129] proposed a numerical method based on the minimum magnetic energy variation (MMEV) and successfully modelled YBCO (with aspect ratio up to 10000) pancake coils with up to 200 turns. Functional of the J formulation is minimized while the transport current in each tape is constrained [130]. $A \cdot J$ was applied to obtained the whole energy in the superconducting domain. Current value that generated the least energy was considered as the sign of stable operating state. The AC losses and current distribution calculated using this method were validated by experimental results.

The thickness of the YBCO superconducting layer is usually smaller than 1 μm, which is thin enough to be considered as a thin sheet. L. Prigozhin was the first to propose a variation formulation of the Kim-Anderson model for calculating the current distribution of bulk superconductors [130]. Later in 2011, this model was extended to simulate the coated conductors [131].

Another advantage of the integral methods is the high efficiency. By applying the critical current state, the highly non-linear iterations caused by the E-J power law in differential methods are successfully avoided. It dramatically shortens the computation time. Also, since the integral methods avoid the global meshes by calculating the points of interest only, the efficiency is improved effectively. This makes the integral method a great way for the simulation of future power applications involving the use of ReBCO tapes.

2.4.3   Differential methods

All differential methods are proposed based on Ampere's law, which can express the relationship between the magnetic field and the current source. The finite element method (FEM) is also applied to these methods to calculate the current distribution by solving partial differential equations (PDEs). The FEM can be implemented by transforming the Maxwell's equations into various formats according to the need for different variables. It is the most general and most developed method to solve the field problems, including calculating the magnetic field, current distribution and AC loss of HTSs. By far, there are three sets of formulas that are widely used for modelling; the A-V formulation [132, 133]; the T-Ω formulation [134, 135]; and the H-formulation. These formulations are named according to their state variables that is solved by the formula. Before applying these formulations to numerical models, boundary conditions; initial values and the resistances of HTS materials need to be predefined in advance. As mentioned above, a superconductor has a *V-I* relation that is shown in Figure 2. 4, which means that the high-temperature superconductors are characterized by the highly non-linear *E-J* power law. The resistance of the superconducting materials can be calculated as follow by using E-J power law;

$$\rho = \frac{E_c}{J_c} \left(\frac{J}{J_c} \right)^{n-1}$$

Equation 2. 21

2.4.3.1   The A-V formulation

The A-V formulation is a mature differential method for simulating all conventional materials and some of the superconductors [136]. Normally, a single scalar potential is preferred as the

state variable for formulations rather than a vector with three components. However, for the magnetic vector potential, **A**, although it generally should have three components, it is more often act as a scalar in most of the practical problems. The vector potential of **B** is defined by **A** as follow;

$$\begin{cases} \mathbf{B} = \nabla \times \mathbf{A} \\ \nabla \cdot \mathbf{A} = 0 \end{cases}$$

Equation 2. 22

Combined with Faraday's law, above equation can be rewritten as;

$$\frac{\partial \mathbf{B}}{\partial t} = -\nabla \times \mathbf{E} = \nabla \times \frac{\partial \mathbf{A}}{\partial t}$$

Equation 2. 23

The arbitrary electric scalar potential, V, is introduced as the voltage gradient of the electric field **E**;

$$\mathbf{E} = -\nabla V - \frac{\partial \mathbf{A}}{\partial t}$$

Equation 2. 24

According to the relevant constitutive equation, $\mathbf{J} = \sigma \mathbf{E}$ and the Maxwell's equation $\nabla \times \mathbf{H} = \mathbf{J}$, the control equation of A-V formulation is calculated as follows;

$$\nabla \times \left(\frac{1}{\mu_0} \nabla \times \mathbf{A} \right) = -\sigma \frac{\partial \mathbf{A}}{\partial t} - \nabla \cdot V$$

Equation 2. 25

Moreover, the second equation of A-V formulation is obtained by considering $\nabla \cdot \mathbf{J} = 0$;

$$\nabla \sigma \left(\frac{\partial \mathbf{A}}{\partial t} + \nabla V \right) = 0$$

Equation 2. 26

In the A-V formulation, the magnetic vector potential A and the electrostatic potential V are state variables. As a scalar field that is related to the electric field E, V can be ignored in many cases [137, 138].

2.4.3.2   The T-Ω formulation

The T-Ω formulation is quite similar with the A-V formulation. The state variables here is the current vector potential T and the scalar magnetic potential Ω. They are defined as

$$\mathbf{J} = \nabla \times \mathbf{H}$$

Equation 2. 27

42

and,

$$\mathbf{H} = \mathbf{T} - \nabla \Omega$$

Equation 2. 28

respectively. The scalar magnetic potential Ω is similar with the static surface charges that determine the electric scalar potential V in the $A\text{-}V$ formulation. It is calculated by associating it with the magnetic surface poles. Now, since

$$\nabla \times \mathbf{E} = -\frac{\partial \mathbf{B}}{\partial t}$$

Equation 2. 29

The control PDE of the T-Ω formulation is obtained;

$$\nabla \times \left(\rho \nabla \times \mathbf{T} \right) = -\mu_0 \left(\frac{\partial \mathbf{T}}{\partial t} - \nabla \left(\frac{\partial \Omega}{\partial t} \right) \right)$$

Equation 2. 30

And since

$$\nabla \cdot \mathbf{B} = 0$$

Equation 2. 31

$$\nabla \mu \left(\mathbf{T} - \nabla \Omega \right) = 0$$

Equation 2. 32

Above formulation indicates that the contouring current vector potential $\mathbf{T}$ provides the streamlines of current in 2D view [136]. In the cases when the ferromagnetic materials do not appear, the scalar magnetic potential is zero, thus Equation 2. 32 can be ignored. Then, this formulation is considered as a formulation that only involves the magnetic flux density $\mathbf{H}$. It is well-known that more variables mean more corresponding equations; which will eventually increase the computation time by a factor of more than ten. Thus, compared with the $\mathbf{A}\text{-}V$ formulation, the T-Ω formulation has a considerable advantage on shortening the computation time. Besides, Amemiya *et al.* combined the T-Ω formulation with the $\mathbf{E}\text{-}\mathbf{J}$ characteristic power law to successfully calculate the AC losses of HTS materials [139, 140].

2.4.3.3   The H formulation

The magnetic field strength $\mathbf{H}$ is the state variable used to solve the Maxwell's equations in this method. According to Faraday's law,

$$\nabla \times \mathbf{E} = -\mu_0 \frac{\partial \mathbf{H}}{\partial t} \qquad \text{Equation 2. 33}$$

Usually, this method is applied to a 2D geometry, where $\mathbf{H}$ is perpendicular to the x-y plane while the superconducting tapes/wires is assumed to have infinite length [141]. Thus, $\mathbf{H}$ can be considered having two components, H_x and H_y. Equation 2. 33 can be rewritten as,

$$\begin{bmatrix} \dfrac{\partial E_z}{\partial y} \\ -\dfrac{\partial E_z}{\partial x} \end{bmatrix} = -\mu_0 \begin{bmatrix} \dfrac{\partial H_x}{\partial t} \\ \dfrac{\partial H_y}{\partial t} \end{bmatrix} \qquad \text{Equation 2. 34}$$

Applying the E-J power law to Equation 2. 34,

$$\begin{bmatrix} \dfrac{\partial \left(E_c \left(\dfrac{J}{J_c} \right)^n \right)}{\partial y} \\ -\dfrac{\partial \left(E_c \left(\dfrac{J}{J_c} \right)^n \right)}{\partial x} \end{bmatrix} = -\mu_0 \begin{bmatrix} \dfrac{\partial H_x}{\partial t} \\ \dfrac{\partial H_y}{\partial t} \end{bmatrix} \qquad \text{Equation 2. 35}$$

The displacement current can be ignored in problems involving quasi-static approximation. Thus, based on the Ampere's law, we obtained;

$$\mathbf{J} = \frac{\partial H_y}{\partial x} - \frac{\partial H_x}{\partial y} \qquad \text{Equation 2. 36}$$

The control equation for the H-formulation is then obtained;

$$\begin{bmatrix} \dfrac{\partial \left(E_c \left(\dfrac{\frac{\partial H_y}{\partial x} - \frac{\partial H_x}{\partial y}}{J_c} \right)^n \right)}{\partial y} \\ -\dfrac{\partial \left(E_c \left(\dfrac{\frac{\partial H_y}{\partial x} - \frac{\partial H_x}{\partial y}}{J_c} \right)^n \right)}{\partial x} \end{bmatrix} = -\mu_0 \begin{bmatrix} \dfrac{\partial H_x}{\partial t} \\ \dfrac{\partial H_y}{\partial t} \end{bmatrix} \qquad \text{Equation 2. 37}$$

44

Turning Equation 2. 37 into the general partial differential equation form gives following formulation;

$$\nabla \times \left(\rho \nabla \times \mathbf{H} \right) + \mu_0 \frac{\partial \mathbf{H}}{\partial t} = 0 \qquad \text{Equation 2. 38}$$

Implementation of the H-formulation in COMSOL Multiphysics provides a new approach of numerical magnetization simulation [142]. The H-formulation model was then validated by comparing the AC loss calculation of the model with experimental data [143]. Then the H-based model was improved to fit in complicated geometries as well as materials [144, 145].

Above differential methods have all been widely and successfully implemented on numerical modelling to calculate the current distribution. However, as YBCO materials are becoming powerful candidates for future electric devices, natural drawbacks of these methods limit the possibility for them to be applied to simulation involving YBCO conductors. The YBCO material has an aspect ratio that is larger than 4000. The dramatic variation of current density also requires extreme fine meshes to obtain accurate distribution of current. Furthermore, the boundary conditions needed by the differential methods further complicated the meshes. When simulating practical engineering devices, more than hundreds of YBCO tapes are wound or twisted together in order to produce the magnetic field as expected. The highly non-linear characteristic of superconductors dramatically increases the computation time of the model. To deal with these realistic-related simulation problems, a new set of formulation, the T-A formulation, was proposed by Huiming Zhang *et al.* in 2016 [146]. Introduction of this formulation is given in Chapter 3.

Chapter 3. AC loss calculation of HTS CORC cable

To date, three-dimensional (3D) modelling of CORC cable is still a great challenge, for the helical geometry makes the boundary condition difficult to set up. The twisted flat tape shape leads to numerous meshing elements even within a single pitch length, which eventually results in increasing hardware requirement for a computer to cope with the computation.

Previous simulation research regarding the CORC cable are mostly done based on the two-dimensional (2D) cross-section approximation. Though several formulations, including the H-formulation, the A-V formulation and the T-Ω formulation, have been available and implemented in various commercial finite element method (FEM) software to simulate applications constructed using 2G HTS materials, considerably errors still remain in the simulation results, when it comes to the modelling of complex geometry or large-scale applications.

This chapter studies the AC loss of the CORC cable numerically. A novel 3D CORC cable model is proposed based on the T-A formulation. The basic geometry of this 3D CORC model is given in Figure 3. 1. Validity of the model is done by comparing the simulation results with other research group's experimental data. The mechanism of AC loss within the CORC cable is studied and discussed in detail. Afterwards, an Advanced 2D T-A model is built to reduce the computation time while maintaining the accuracy of simulation results.
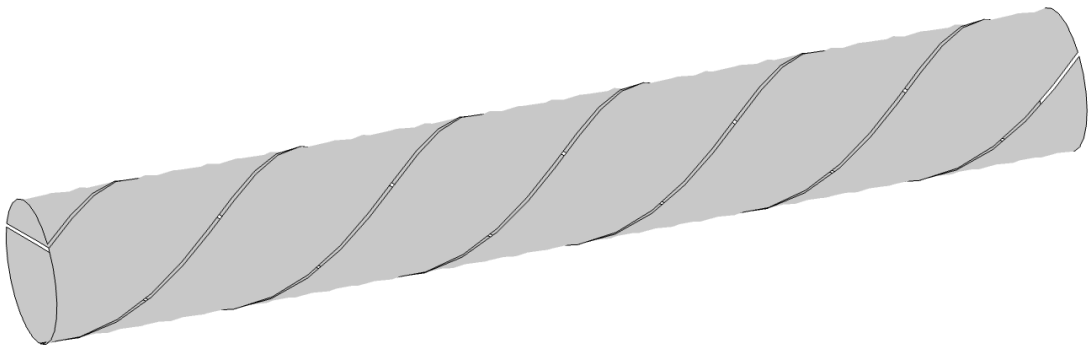
Figure 3. 1 Structure of the novel 3D T-A model for a single-layer CORC cable.

3.1 A novel 3D T-A model

3.1.1 Introduction of the T-A formulation

The 2G HTS tapes, especially the ReBCO tapes have quite high aspect ratio (which equals width/thickness). For instance, a commercial ReBCO tape produced by the SuNAM Company has a width of 4 mm, while the thickness of the tape is only 0.1 mm. The ReBCO layer itself is even thinner, which only has a thickness of $1\mu m$. Modelling of the CORC cable wound with ReBCO tapes could be difficult, for the unique geometry and high aspect ratio of tapes lead to numerous mesh elements and poor convergence.

The newly proposed T-A formulation [146, 147] is used as a solving equation for this 3D CORC cable model. The basic assumption of this formulation is to treat the the superconducting coated conductor as an infinitely thin sheet, in which case the thickness is reasonably neglected. The thin sheet approximation of the T-A formulation is given in Figure 3. 2. The current vector potential **T** and the magnetic vector potential **A** are the two state variables. The current vector potential **T** is applied to the superconducting region to solve the current density distribution of coated conductors. Definition of this state variable can be expressed as,

$$\nabla \times \mathbf{T} = \mathbf{J} \qquad \text{Equation 3. 1}$$

where **J** represents the current density vector with a unit of *A/m²*. Due to the thin sheet assumption of the superconducting tapes, the transport current only flows tangentially along the tapes, which means that the current vector potential **T** is always perpendicular to the tape's wide surface. Thus, combined with the normal unit vector to the tape surface, **n**, as can be seen in Equation 3. 2,

$$\mathbf{n} = \begin{bmatrix} n_x \\ n_y \\ n_z \end{bmatrix} \qquad \text{Equation 3. 2}$$

expression of **T** can be rewritten as,

$$\nabla \times (T \cdot \mathbf{n}) = \mathbf{J} \qquad \text{Equation 3. 3}$$

$$\begin{bmatrix} \dfrac{\partial(T \cdot n_z)}{\partial y} - \dfrac{\partial(T \cdot n_y)}{\partial z} \\[2ex] \dfrac{\partial(T \cdot n_x)}{\partial z} - \dfrac{\partial(T \cdot n_z)}{\partial z} \\[2ex] \dfrac{\partial(T \cdot n_y)}{\partial x} - \dfrac{\partial(T \cdot n_x)}{\partial y} \end{bmatrix} = \begin{bmatrix} J_x \\[1ex] J_y \\[1ex] J_z \end{bmatrix} \qquad \text{Equation 3. 4}$$

Here, the scalar T is the magnitude of **T**. ReBCO coated conductors are constrained by the E-J power law, which expresses the nonlinear relationship between the electric field **E** and the current density **J**,

$$\mathbf{E}(\mathbf{J}) = E_0 \left(\frac{|\mathbf{J}|}{J_c(\mathbf{B})} \right)^n \cdot \frac{\mathbf{J}}{J_c(\mathbf{B})} \qquad \text{Equation 3. 5}$$

The constant value n is taken as 31, $E_0 = 1 \times e^{-4}$ V/m, **B** is the magnetic flux density, **J** is the transport current density flowing in the superconducting layer, and J_c is the critical current density of the tapes and is set to be a constant to implement the T-A formulation. Thus, according to the Maxwell's equation, the governing equation of the ReBCO coated conductors is obtained as,

$$\nabla \times \mathbf{E}(\nabla \times (T \cdot \mathbf{n})) + \frac{\partial \mathbf{B}}{\partial t} = 0 \qquad \text{Equation 3. 6}$$

The magnetic field B in Equation 3. 6 is solved using the magnetic vector potential **A**, which is the state variable that is applied to the whole model domain. The governing equation for the traditional A-formulation can be derived from Ampere's law as follow,

$$\begin{cases} \nabla \times \nabla \times \mathbf{A} = \mu \mathbf{J} \\ \nabla \times \mathbf{A} = \mathbf{B} \end{cases} \qquad \text{Equation 3. 7}$$

where μ is the magnetic permeability. Consider a transport current **J**$_{\textbf{trans}}$ that only flows in the superconducting tapes and can be obtained from Equation 3. 3 using the T-formulation. Boundary condition of the transport current can thus be defined as,

$$(\mathbf{H_2} - \mathbf{H_1}) \times \mathbf{n} = \mathbf{J}_{trans} \qquad \text{Equation 3. 8}$$

where H_1 and H_2 are the magnetic fields on the left and right edges of the superconducting tapes. When it comes to the simulation of applying external magnetic field to the cable model, simply

impose a magnetic field B=($B_0 \sin(2\pi ft)$ 0 0) as a boundary condition on the outmost boundary of the model domain [15].

The AC loss induced in the superconducting layer can then be calculated by,

$$Q = 2\int_{T/2}^{T} dt \int_{\Omega} \mathbf{E} \cdot \mathbf{J} d\Omega$$

Equation 3. 9

Where Ω represents the region of HTS materials in the model, the unit of Q is Joules/cycle.

In conclusion, the T-A formulation is mainly about coupling and solving two state variables, the current vector potential **T**, and the magnetic vector potential **A**. This set of formulation is applied to the 3D model built in COMSOL Multiphysics, in the aim of reducing the huge number of mesh elements, shortening computation time as well as getting precise simulation results.
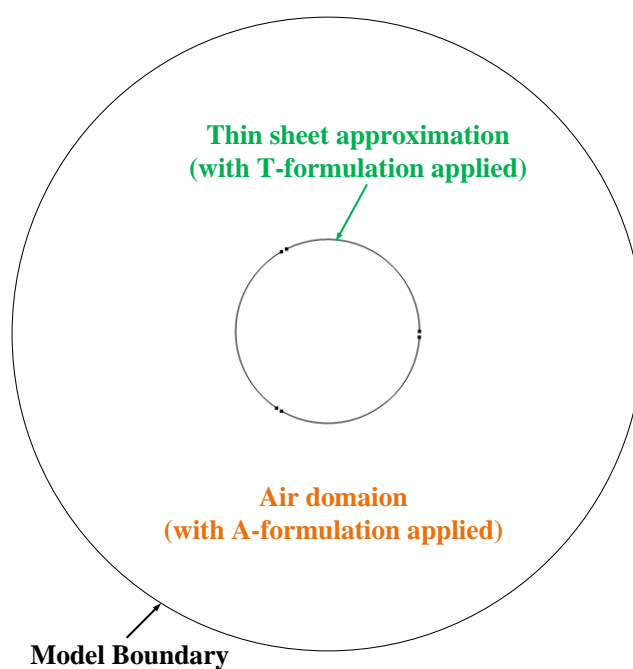
Figure 3. 2 Thin sheet approximation of T-A formulation in cross section of CORC cable model.

Based on the T-A formulation, a novel 3D T-A model was established for CORC cable simulation in this chapter. Two basic ReBCO CORC cable samples are designed and simulated. The first cable sample is a single-layer ReBCO CORC cable with a full pitch length. For convenience, it is labelled as 'Cable A' in following research work. Another cable sample has

two layers with the same winding direction. It is called 'Cable B'. More detailed specification and physical properties of both samples are given in Table 3. 1.

Table 3. 1 Specification of two CORC cable samples.

Parameter	Cable A	Cable B
Number of layers	1	2
Number of tapes per layer	3	3
Diameter of layers	5.14 mm	5.14 / 5.28 mm
Winding direction	/	Same
Winding angle	2°/5°/10°/20°/30°/40°	40°
Length of pitch	19 mm	19 mm
I_c of ReBCO tape, @ 77 K	150 A / 100 A	150 A / 100 A

3.1.2 Validation of a 2D T-A based CORC model

Firstly, to fully prove the validity of the proposed T-A formulation, a simple two-dimensional (2D) CORC cable model based on the T-A formulation was proposed to model Cable A. A reference 2D model that is based on the *H*-formulation was built. Parameters and physical properties applied to both models are exactly the same. As a mature numerical modelling method, the well-validated H-formulation has been proved to be sufficient and reliable enough for most of the 2D numerical modelling [147]. Results obtained from the T-A based model were then compared with those computed using the *H*-formulation.

Figure 3. 3 presents the geometry of the single-layer CORC cable sample that is built based on the *H*-formulation and the T-A formulation respectively. For simplicity, only the superconducting layers of the ReBCO tapes are simulated in both models. It is clearly shown in Figure 3.2 (a) that each tape in the *H*-formulation model has a cross section, as a thickness of 100 μm still applies to the ReBCO tapes. Meanwhile, the T-A formulation model, by applying the thin sheet approximation to ignore the thickness of the tape, reasonably transforms the cross section of each ReBCO tape into an infinitely thin line.

(a)

(b)
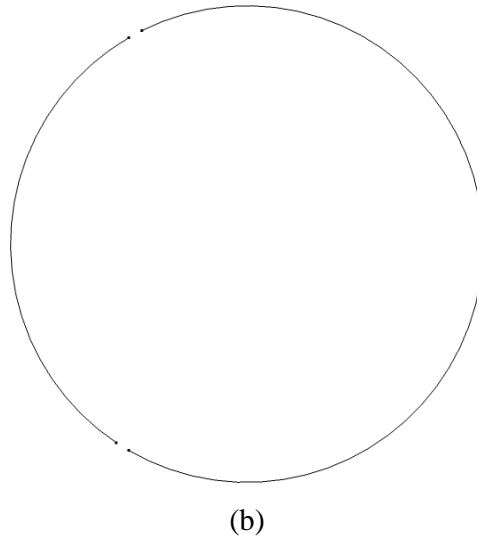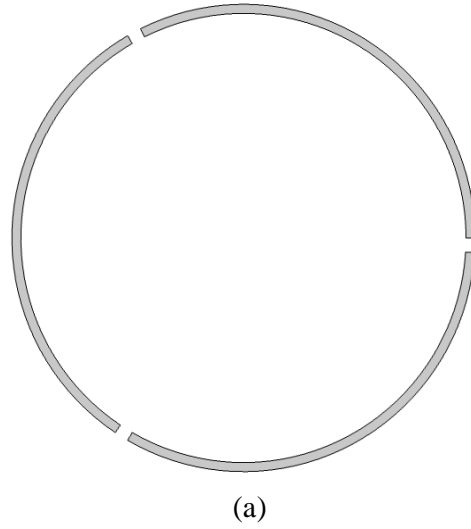
Figure 3. 3 The cross section of the single-layer CORC cable (Cable A) (a) based on the H-formulation; and (b) based on the T-A formulation respectively. Winding angle (θ) for this CORC cable sample is 40°.

3.1.2.1   AC transport loss

The validation is first carried out considering a self-field environment, which means there is no external magnetic field in any direction. A sine-wave AC transport current is applied to both models with a magnitude of 120 A, while the critical current I_c of each tape is 150 A in this case. Frequency f of the applied current is set to be 50 Hz and the voltage criterion of the electric field E is 10^{-4} V/m (which equals to 1 μm/cm). To determine the anisotropy of the

ReBCO tapes, the modified Kim-Anderson model was used in following study [63-65, 148]. It can be expressed as follows,

$$J_c(\mathbf{B})=J_c(B_\parallel, B_\perp)=\frac{J_c(0)}{\left(1+\dfrac{\sqrt{k^2\left|B_\parallel\right|^2+\left|B_\perp\right|^2}}{B_0}\right)^\alpha}$$

Equation 3. 10

Here, $B_{/\!/}$ and $B_\perp$ are the parallel and perpendicular components of the local magnetic field for the curved surface respectively. They are implemented to the model using following equations,

$$B_\perp=\frac{\partial B\cdot n_x}{\partial x}+\frac{\partial B\cdot n_y}{\partial y}+\frac{\partial B\cdot n_z}{\partial z}$$

Equation 3. 11

$$B_\parallel=\sqrt{\left(\frac{\partial B\cdot n_z}{\partial y}-\frac{\partial B\cdot n_y}{\partial z}\right)^2+\left(\frac{\partial B\cdot n_x}{\partial z}-\frac{\partial B\cdot n_z}{\partial x}\right)^2+\left(\frac{\partial B\cdot n_y}{\partial x}-\frac{\partial B\cdot n_x}{\partial y}\right)^2}$$

Equation 3. 12

The shape parameters B_0, k, and b in Equation 3.10 represents the anisotropic characteristics of the tapes used in this research and are all constants. $B_0=0.1017$ T, $\alpha=0.7636$, and $k=0.05869$. These values are decided or calculated from the measured parameters of the ReBCO tapes produced in SuNAM company at an operating temperature of 70 K. For both models, the AC loss of the CORC cable sample is then calculated based on Equation 3.9.

Figure 3. 4(a) provides the sinusoidal wave of transport AC losses for a full-cycle time, here is 0.02 seconds, from the H-based and the T-A based 2D model respectively. Waveform of the applied transport current I_{op} is shown in Figure 3. 3(b). Compared with that obtained from the H-based model, the transport AC loss obtained from the T-A based model only has slightly higher values when the magnitude of I_{op} gradually increases. It clearly shows that a well agreement has been achieved between the simulation results obtained from these two models.
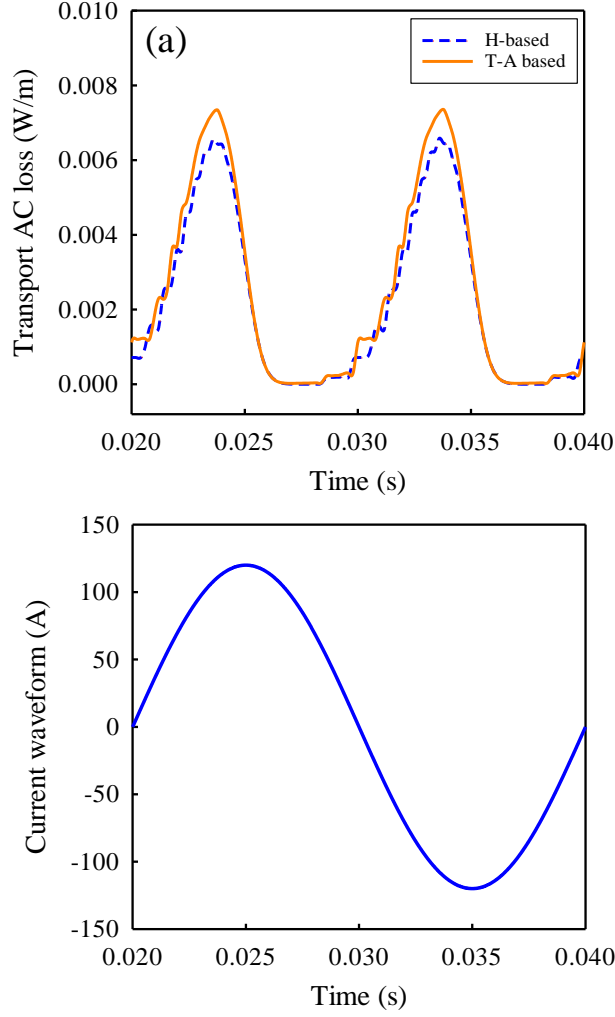
Figure 3. 4 The transport AC losses for a full-cycle time of the 2D H- and T-A based models respectively; I_{op} (the applied transport current) = 120 A, I_c = 150 A, f = 50 Hz.

3.1.2.2 Magnetization loss

The proposed T-A based model is then validated with the existence of an external magnetic field. Same cable sample structure is utilized in both the T-A and the H model. All parameters remain the same, except that there is no transport current applied to the cable in this case. Here, value of the external magnetic field is 20.5 mT. The AC losses obtained from both models are shown in Figure 3. 5, which shows that simulation results from both models present agreeable trends of magnetization losses for a full-cycle time. Same as above, the T-A based model shows a slightly higher result compared with the H model.

This difference between the results of the H- and T-A formulation models might be caused by different meshing methods used for two models. For the T-A based 2D model, the Distribution node was used to specify the distribution of mesh elements along each tape. Each tape was divided into a fixed value of elements, in this case, 60. Rest of the model was meshed using free triangular elements. The total number of elements was 6096. The H based 2D model, on the other hand, uses Mapped mesh on the ReBCO tapes. 50 elements were distributed on each one of the tapes with an element ratio of 2. The total number of elements for this model was 6664, which is obviously higher than that of the T-A based model. For a better comparison, the relative error (%) of the magnetization AC loss against time is calculated using the equation below,

$$\text{Relative error (\%)} = \frac{\left|W_{TA} - W_H\right|}{W_{TA}} \times 100 \qquad \text{Equation 3. 13}$$

where W_{TA} is the transport loss from the T-A based model, while W_H is the transport loss from the H-based model. Relative error in half-cycle time duration is plotted in Figure 3. 6, from which the error of the T-A model with respect to that of the H model is restricted within 20% or below, which is considered to be acceptable in this research. It proved that the proposed T-A based model works well to simulate the dynamic electromagnetic characteristics of the 2G HTS CORC cable in two-dimensional space.
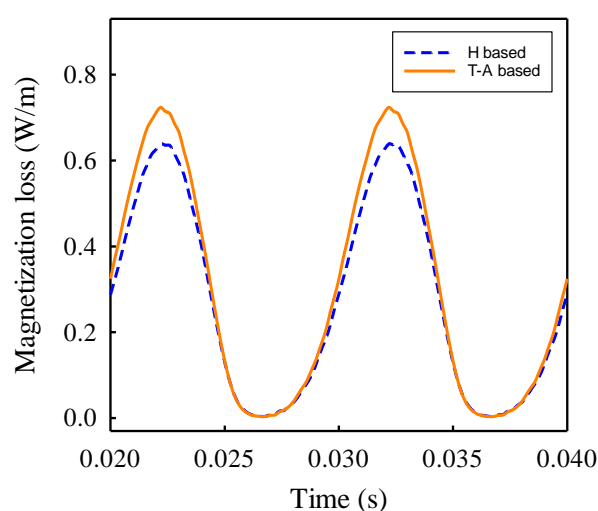
Figure 3. 5 The magnetization losses for a full-cycle time of the 2D H- and T-A based models respectively; B_{ext} (the external magnetic field) = 20.5 mT, I_c = 150 A, f = 50 Hz.

54
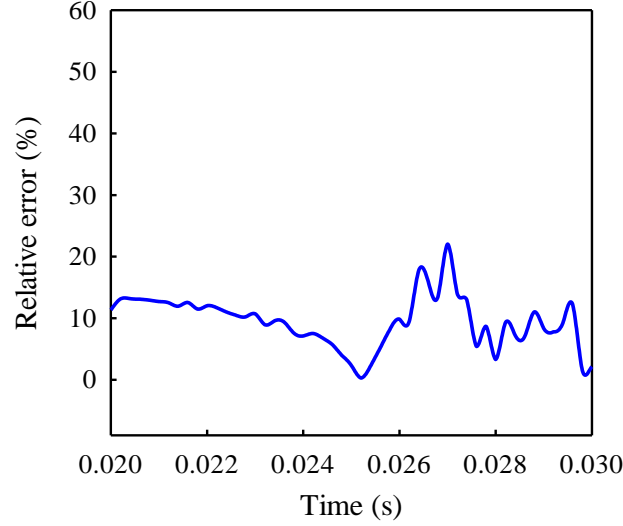
Figure 3. 6 Relative error (%) for half-cycle time of the values calculated in the T-A model with respect to those simulated in the H model.

3.1.3   The 3D T-A model simulation compared to measurement

Main advantage of the T-A formulation, i.e. the thin-sheet approximation to reduce the mesh elements as well as reduce the calculation time, is more obviously reflected in a three-dimensional space. To prove the validity of the aforementioned T-A CORC cable model in 3D space, AC losses obtained from the model has been compared with those published in [9]. Measurement data of CORC cable's magnetization loss is provided by Dr. Francesco Grilli from the Karlsruhe Institute of Technology (KIT). Note that validation of the 3D T-A CORC model has already been published in [15].

Two cable samples are simulated in this case study, with 2 and 3 layers respectively. Both of them have 3 ReBCO tapes in each layer, which means the total number of tapes is 6 and 9 respectively. ReBCO tapes used for the measurement are 4 mm wide and have the same thickness, which is about 0.1 mm. Thickness of the ReBCO layer is set to be 1 μm. The ReBCO tape uses Hastelloy as its substrate, and copper stabilizers are mounted on both sides of the tape. The tape has a critical current of 100 A at 77 K in self-field. Both ends of the cable use open terminations to prevent coupling current from inducing between tapes [149, 150]. Detailed geometry and physical properties about the cable samples are given in Table 3. 2. According to the analysis in [9], the ReBCO tapes with copper at their edges generate high coupling losses, which is unwanted. Thus, in

the simulation process, we used ReBCO tapes with cut edges instead. Also, only the superconducting ReBCO layers are simulated in the cable model, which means there will be no electrical coupling between individual tapes. Different external magnetic fields were applied to these two cable samples. The magnetization AC loss obtained from 3D simulation was compared with measurement data from experiments. Results are plotted in Figure 3. 7. The calculated magnetization loss slightly differs from the measured loss only at the presence of low external magnetic fields. The overall simulation results for two CORC cable samples are in well agreement with measurement data, which validates the accuracy and reliability of the proposed 3D T-A CORC model. In the following study, this model is used to systematically study the electromagnetic behaviours of the CORC cable.

Table 3. 2 Specification of the two cable Samples.

Parameter	Sample B	Sample C
Number of layers	2	3
Number of tapes in each layer	3	3
Radius of each layer (mm)	2.57 / 2.64	2.57 / 2.64 / 2.71
Winding angle (°)	45	45
Width of ReBCO tape (mm)	4	4
Thickness of ReBCO tape (μm)	100	100
Critical current of each tape (A)	100	100
Frequency (Hz)	130	130
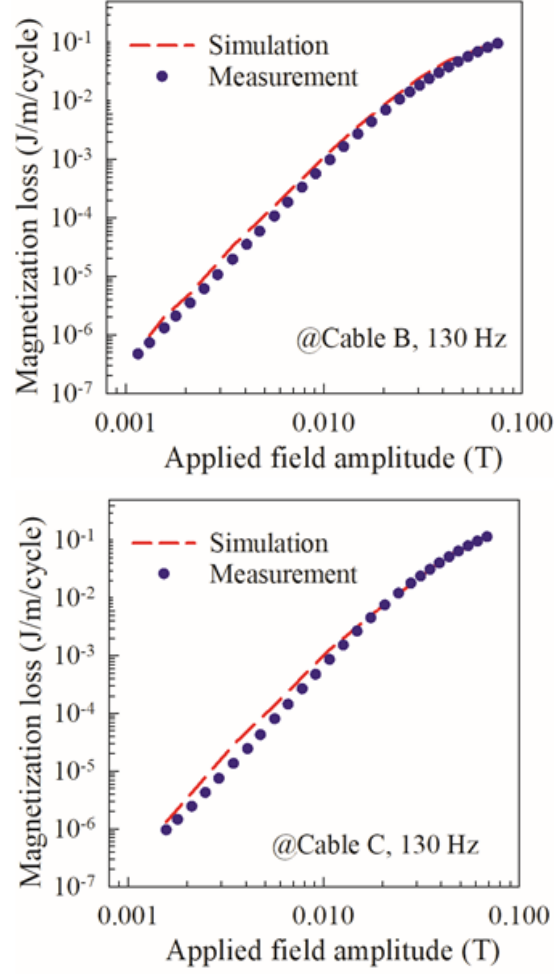
Figure 3. 7 Comparison of magnetization loss of Cable Sample B and Cable Sample C between the simulation results and the measurement data. Unit: J/cycle/m of cable length.

3.2 AC loss calculation for two CORC cable samples

This section aims at presenting a systematic study of the electromagnetic behaviours of two specific CORC cable samples. The AC losses, including the transport loss generated by various transport currents and the magnetization loss induced by alternating background fields, are calculated. The current density distribution as well as the magnetic field distribution is presented, too.

Specification and physical properties of both samples are given in Table 3. 3. One is a single-layer CORC cable that is labelled as 'Cable A'. The other sample is a double-layer CORC cable, which is called 'Cable B'. Specification of the superconducting tapes used in this research is given by SuNAM company. For both samples, each layer is constructed from 3

ReBCO tapes with a width of 4 mm and a thickness of 0.1 mm. Thickness of the superconducting layer in the ReBCO tape is 1 μm. Substrate of the ReBCO tape is Hastelloy, and copper is used as the stabilizer on both top and bottom of the tape. Critical current of the ReBCO tape is 150 A at 77 K under self-field. For convenience, in Cable B, both layers have same winding direction. The air gaps are perfectly aligned between layers, which means the gaps in the inner layer match well with that in the outer layer. To simplify the simulation, only the superconducting layer within the ReBCO tape is modelled. This approximation is made due to the relatively low resistivity of the superconducting layer, compared with other layers of the ReBCO coated conductor. The superconducting layers are separated by air, since there is no electrical coupling between layers and air [149].

Figure 3. 8 presents the basic structure of Cable A with a winding angle of 40° in the 3D T-A model. Radius of this cable sample is 2.57 mm. When a transport current is applied to each tape of the cable, it flows within the tape surface along the direction pointed out using the red arrows. The black arrows show the external magnetic field that is applied to the CORC cable. Using this model, both the transport AC loss and the magnetization AC loss is calculated for the two cable samples, i.e. Cable A and Cable B.

Table 3. 3 Specification of the two CORC cable samples

Parameters	Cable A	Cable B
Number of layers	1	2
Number of tapes per layer	3	3
Diameter of layers (mm)	5.14	5.14 / 5.28
Winding direction	/	Same
Winding angle (°)	2°/5°/10°/20°/30°/40°	40°
Pitch (mm)	19	19
I_c of ReBCO tape, @77 K (A)	150 / 100	150 / 100

Red arrow: direction of transport current

Black arrow: External magnetic field
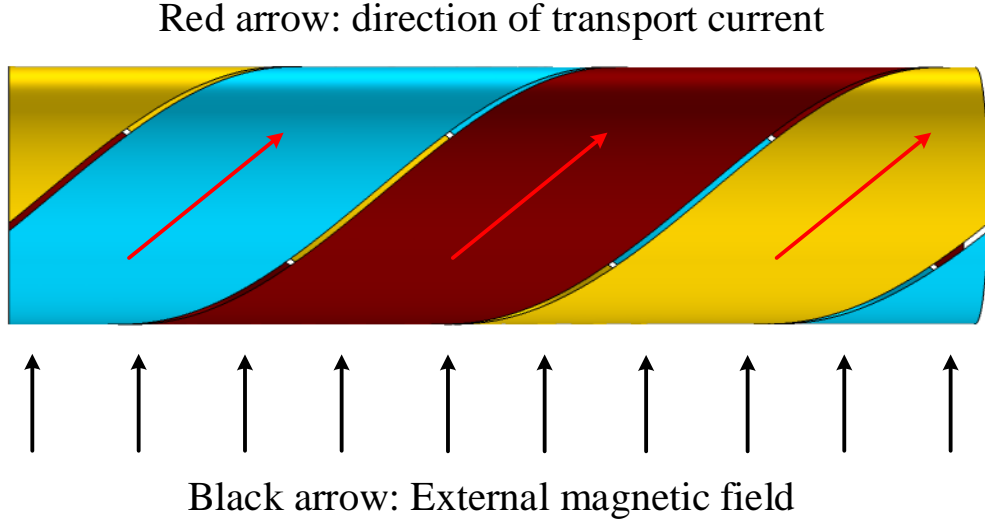
Figure 3. 8 Structure of the single-layer CORC cable.

3.2.1 The transport AC loss

Study of the transport AC loss is carried out using the single-layer CORC cable model. The critical current I_c of the ReBCO tape is 150 A in this case. A fixed value of transport current (from 40 A to 120 A) is first applied to each tape simultaneously in Cable A, while the external background field does not exist. The simulation was run at two different frequencies, 50 Hz and 130 Hz, for the aim of analysing the influence of frequency on the AC losses. The transport AC loss in per unit length of the cable under one cycle time (J/cycle/m) is obtained by using the surface integration function. Figure 3. 9 presents the calculated transport AC losses under various transport currents at a frequency of 50 Hz and 130 Hz respectively. From the overall trend of the losses, when the transport current I_{op} is low, i.e. 40 A or 60 A, the increase of the transport current can only slightly increase the transport AC losses. However, when the value of I_{op} reaches 50% of the critical current I_c (150 A), a slight rise of I_{op} leads to a significant increase of the transport AC losses. On the other hand, with low transport current applied, the losses generated under two frequencies are almost the same. It is only when the transport current is closer to the critical value that the loss generated under 50 Hz is slightly higher than that under 130 Hz. This indicates that the transport AC losses of single-layer CORC cable is almost frequency independent.

Additionally, to provide a comprehensive comparison among transport AC losses generated under different transport currents, detailed simulation results of Cable A are provided. The left

column in Figure 3. 10 presents the current density distribution of Cable A when a transport current of 120 A is applied, while the right column shows the distribution of the current density with I_{op}=80 A. The colour bar is for both cases. At a quarter cycle and three-quarter cycle, the current density in the middle region of each tape, which is also called the 'subcritical region' in Cable A, with I_{op}=120 A reaches 300 MA/m², while a transport current of 80 A only provides current density of around 200 MA/m². The highest current density appears at the edge of ReBCO tape, with the value of 395.8 MA/m² for I_{op}= 120 A and 387.8 MA/m² for I_{op}= 80 A. Comparison of the current densities in Cable A under different transport currents indicates that for a single-layer CORC cable, higher applied transport current results in higher current density, which finally leads to higher transport AC loss.
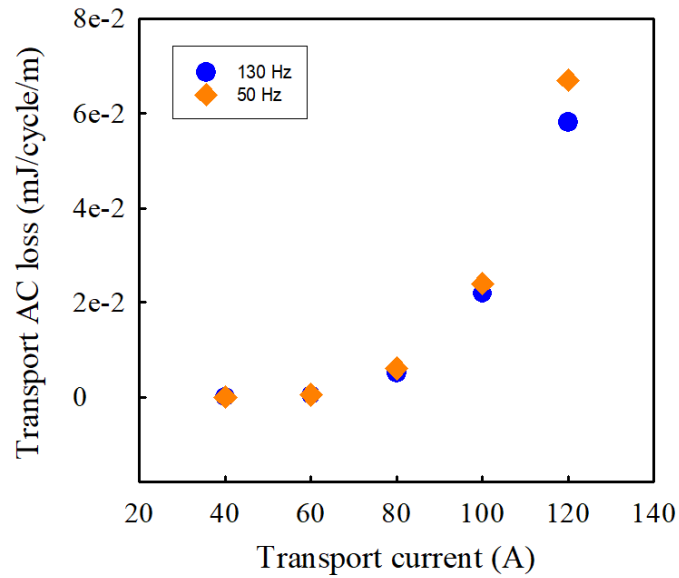
Figure 3. 9 Transport AC losses (mJ/cycle/m) of Cable A under various transport currents (40, 60, 80, 100, and 120 A) in per unit length of the cable for a full cycle time. The frequency of the current is 50 Hz and 130 Hz respectively. Winding angle (θ) is 40°.

(a) I_{op} = 120 A   (b) I_{op} = 80 A

t = T/4

t = 2T/4

t = 3T/4

t = T

$\times 10^8$ (A/m^2)
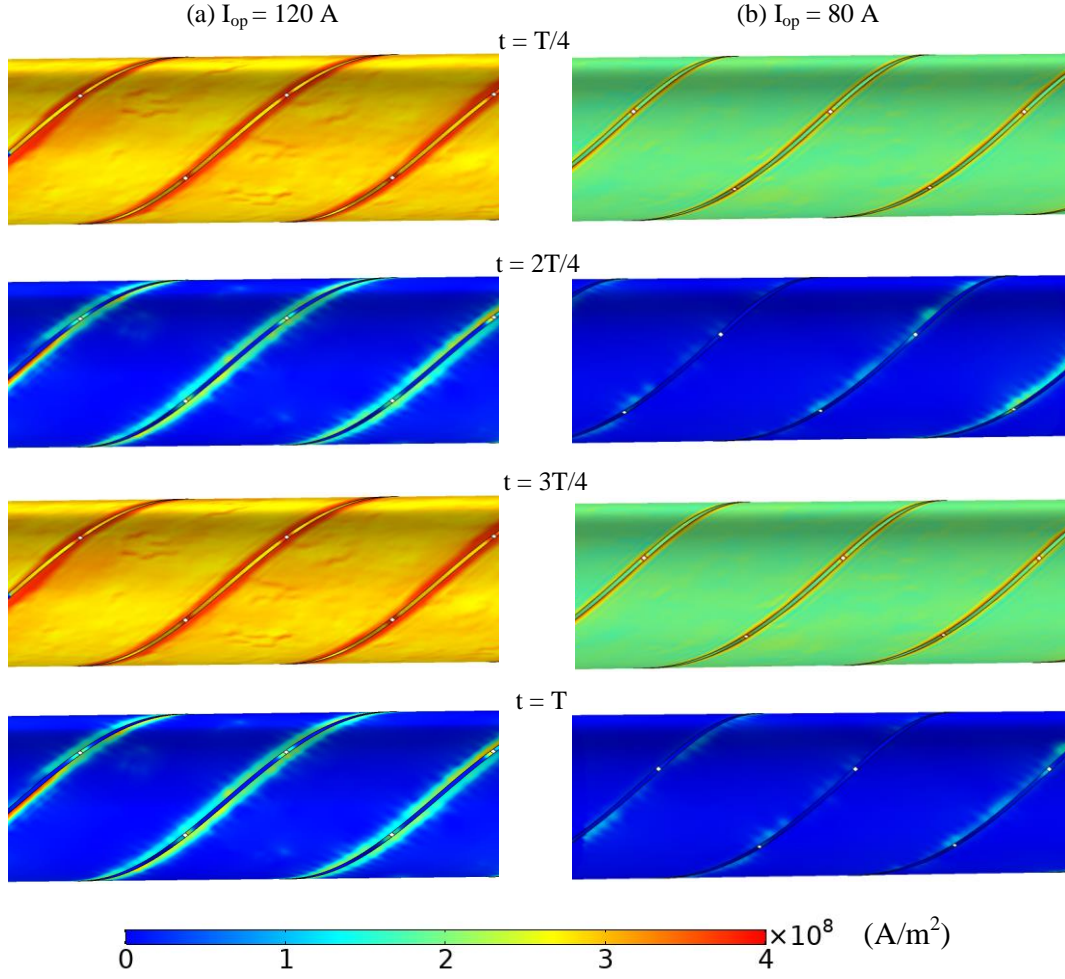
Figure 3. 10 Distribution of the current density (A/m²) of Cable A with (a) I_{op} = 120 A; and (b) I_{op} = 80 A for a full-cycle time. f = 130 Hz, B_{ext} = 0 T, θ = 40°.

3.2.2 The magnetization AC loss

Different magnitudes of the external magnetic field are applied to both Cable A and Cable B to calculate the magnetization AC losses. No transport current is applied in this section. The frequency is fixed at 130 Hz, while the critical current I_c of the ReBCO tape is 100 A now. Figure 3. 11 shows the magnetization losses in both Cable A and Cable B that are calculated under the external magnetic field of which has a magnitude from 1.56 mT to up to 67.1 mT. It clearly shows that the magnetization AC loss increases with the increase of magnitude of the external magnetic field in both single-layer CORC cable and double-layer CORC cable. Moreover, a nearly linear magnetization AC loss increase is observed at the high field region –

over 20.5 mT in this case – which indicates the dependency of magnetization loss of CORC cable on the magnitude of external magnetic field [149]. From Figure 3. 11, an apparent crossover of the magnetization losses is observed between the magnetization losses generated in Cable A and Cable B with the increase of external magnetic field. The turning point, in this case, is at an external magnetic field of 20.5 mT. To understand this phenomenon, we focused on the distribution of current density, as well as the current flowing direction, in both cable samples.

Figure 3. 12 presents the distribution of the induced current density on one of the ReBCO tapes for a pitch length in Cable A. Since the CORC cable structure has a symmetric geometry, the other two tapes have the same current density distribution with the one plotted in the figure. The black arrow plotted on the tape surface shows the flowing direction of the current density. Within one pitch length of Cable A, at t = T/4, two magnetization current loops are induced on the areas of tape surface that are perpendicular to the external magnetic field. Most of the magnetization losses are thus generated in these areas, of which is perpendicular to the transverse magnetic field. These two current loops, having opposite flowing directions, encounter and cancel each other at the tape areas that are parallel to the applied external magnetic field. Thus, these areas have much lower current densities compared with that are perpendicular to the transverse field. This also leads to lower magnetization losses generated in these areas. The current density distribution at t = 3T/4 is almost the same with that at the quarter cycle, only with the current flowing in a reversed direction compared with the quarter cycle situation.

Meanwhile, the current density distribution of Cable B for a full-cycle time is also given in Figure 3. 13, calculated at 130 Hz. Distribution on the inner layer and outer layer are extracted respectively. For a more intuitive comparison, only one tape per layer is shown here. Clearly, the current density at a quarter cycle in the outer layer of Cable B is much higher than that in the inner layer. This is the result of the field shielding effect, of which is related to the coverage rate of the ReBCO tapes between layers [151]. The coverage rate can be expressed as follow,

$$R_{coverage} = \frac{S_{overlapped}}{S_{inner}} \times 100\% \qquad \qquad \text{Equation 3. 14}$$

62

Since two layers of Cable B are in the same winding direction and are perfectly aligned with each other, the inner layer is almost fully covered by the outer layer, which means the overlapped area of two layers are quite large. The coverage rate of Cable B is high enough to form a strong shielding effect. Thus, the external magnetic field lines in the inner layer is partly screened by the outer layer of ReBCO tapes. This phenomenon also explains the lower magnetization loss of Cable B compared with Cable A under low magnetic field. However, from Figure 3. 13, it is clear that at $B_{ext} = 20.5$ mT, the outer layer of Cable B is close to a full penetration state. Increase of magnitude of the external field leads to the full penetration state, under which the shielding effect is weaker, thus resulting in higher magnetization losses. Figure 3. 14 and Figure 3. 15 present the distribution of the magnetic flux density of both Cable A and Cable B at $B_{ext} = 20.5$ mT. It can be clearly seen that the penetration in Cable A is much more obvious than that in Cable B. Moreover, for the double-layer cable, the penetration of field in the outer layer is deeper than that in the inner layer, which further proves the shielding effect.

In conclusion, adjacent current loops with opposite flowing directions are induced on tape areas that are perpendicular to the external magnetic field, lowering the current density and magnetization loss of CORC cable. At low external magnetic field – lower than 20.5 mT in this case – the magnetization loss of double-layer CORC cable is lower than that of single-layer CORC cable, due to the strong shielding effect considerably screens the magnetic field in the inner layer. At high field region (when the field is above 20.5 mT), the CORC cable is in full penetration state, the shielding effect is weaker and results in higher magnetization loss in double-layer case, compared with the single-layer cable.
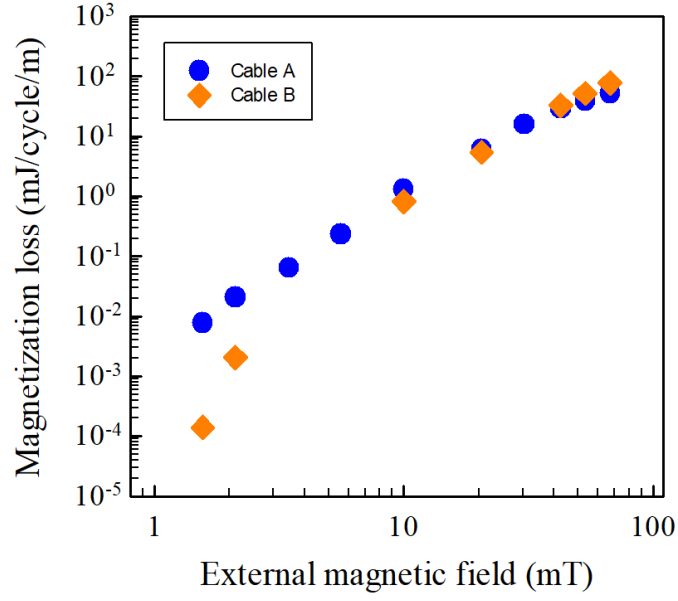
Figure 3. 11 Magnetization losses (J/cycle/m) generated in Cable A and Cable B under external magnetic field (B_{ext}) varies from 1.56 mT to 67.1 mT. I_{op} = 0 A, f = 130 Hz.
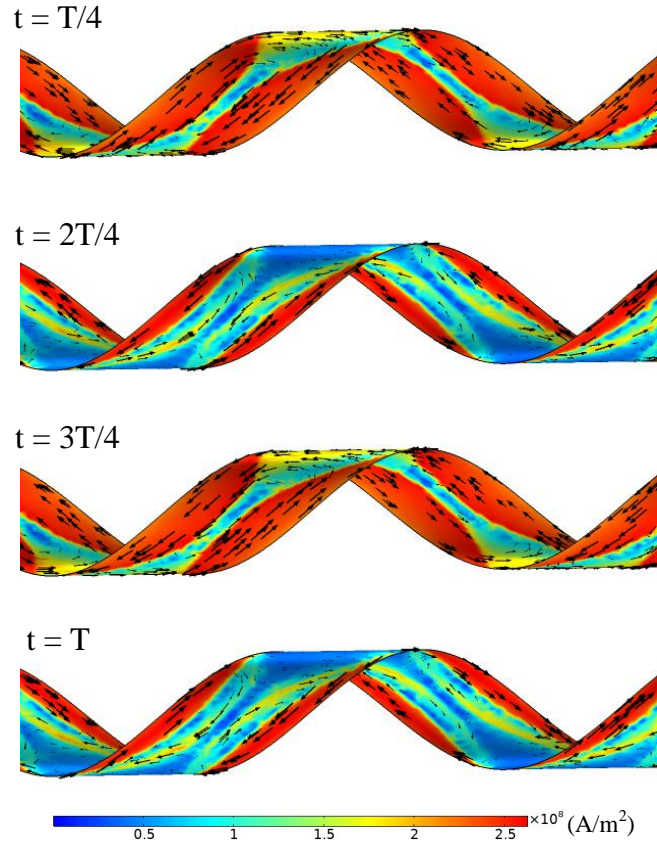
Figure 3. 12 Distribution of the induced current density on one of the ReBCO tapes in the single-layer CORC cable (Cable A) for a full-cycle time. The external magnetic field B_{ext} = 20.5 mT. I_{op} = 0 A, f = 130 Hz.
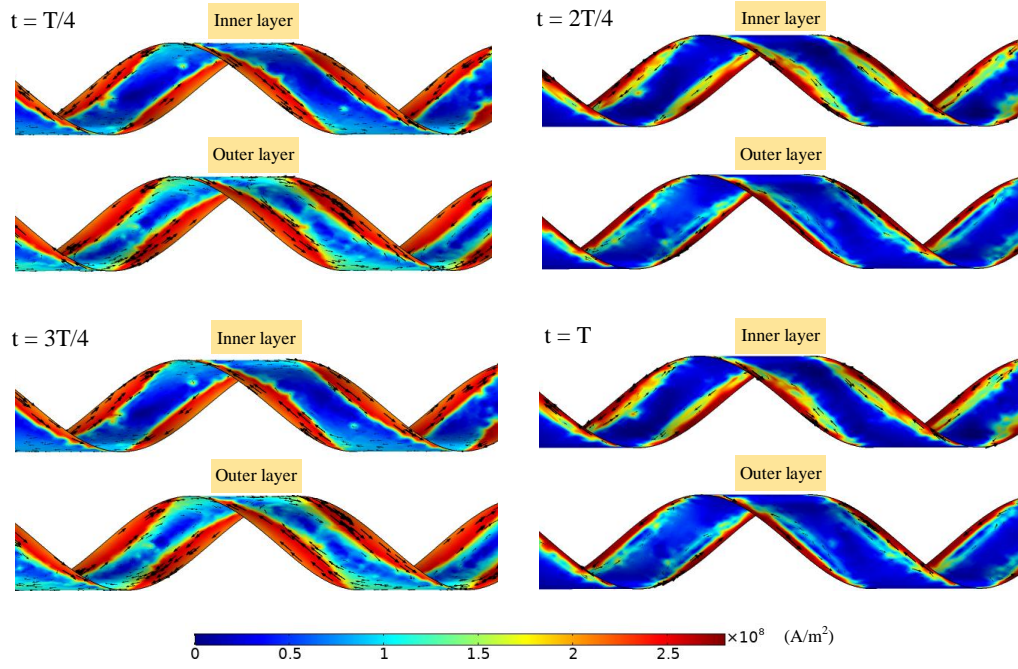
Figure 3. 13 Distribution of the induced current density on one of the ReBCO tapes in the double-layer CORC cable (Cable B) for a full-cycle time. Distribution on the inner and the outer layer is presented respectively. The external magnetic field $B_{ext} = 20.5$ mT. $I_{op} = 0$ A, $f = 130$ Hz.
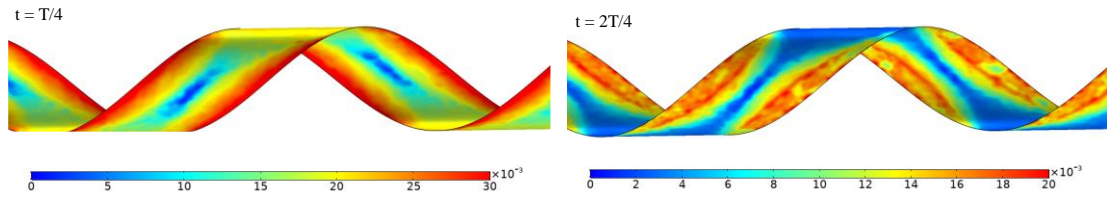
Figure 3. 14 Distribution of the magnetic flux density on one of the ReBCO tapes in the single-layer CORC cable (Cable A) for a half-cycle time. The external magnetic field $B_{ext} = 20.5$ mT. $I_{op} = 0$ A, $f = 130$ Hz.
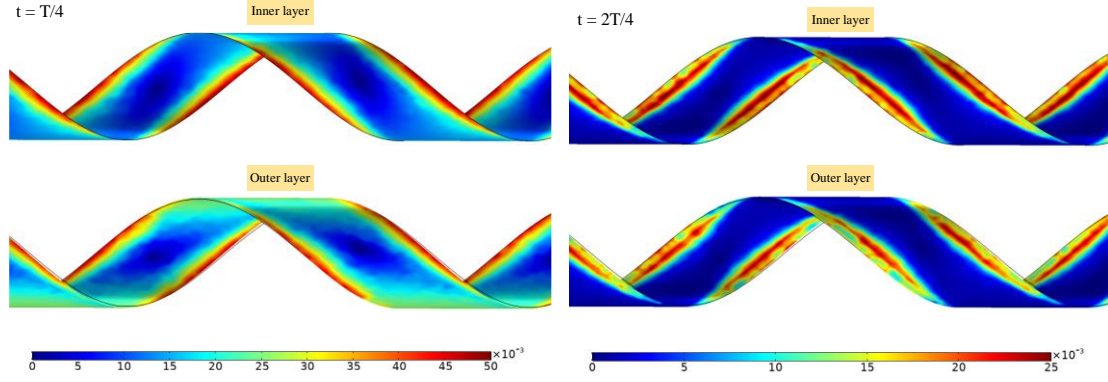
Figure 3. 15 Distribution of the magnetic flux density on one of the ReBCO tapes in the double-layer CORC cable (Cable B) for a half-cycle time. Distribution on the inner and the outer layer is presented respectively. The external magnetic field B_{ext} = 20.5 mT. I_{op} = 0 A, f = 130 Hz.

3.3 A novel 2D model

3.3.1 Three novel 2D T-A model for the AC loss calculation of CORC cable

Although applying the T-A formulation to the 3D model helps to precisely reproduce the complex geometry of CORC cable, and it effectively shortens the computation time, computation for a T-A 3D CORC model can still take days. Thus, an accurate and efficient T-A 2D CORC model is in need to further shorten the computation time as well as to get precise results. This section aims at establishing a novel 2D T-A based model for the simulation of CORC cable.

Helical geometry of CORC cable leads to components of transport current along the axial and horizontal direction of the cable. Meanwhile, size of the air gap between coated conductors, which is affected by winding angles, is also a key factor for 2D cable simulation, for the width of ReBCO tape on the horizontal direction of the cable varies with winding angle. By considering the transport current components as well as the dependence of the air gap between tapes on the winding angle, three novel 2D T-A models are proposed here.

Specifications of cable samples used in this section, Cable A and Cable B, are the same with Section 3.2. Critical current of the ReBCO tape is fixed at 150 A at 77 K in self-field. Construction of a 2D CORC cable model involved two main issues, spiral geometry of the CORC cable, and the

gap effect on the AC loss of the cable [152]. Since 2D simulation only models the cross section of the CORC cable, the spiral structure, as well as the full transposition of tapes, is not shown in the model. However, the transposition of tapes is one of the key factors that remarkably reduce AC loss generated in the CORC cable. Thus, to measure the AC loss using a 2D model, the winding geometry of tapes in the CORC cable has to be presented. The size of air gaps between ReBCO tapes, which will vary with the winding angle of the cable, also has an impact on AC loss of the CORC cable [152]. Considering these factors, three novel 2D T-A models are presented in this paper.

(a) *The Advanced 2D CORC cable model.* The novel advanced 2D model firstly considers the cross-sectional geometry of CORC cable. Width of each ReBCO tape in the horizontal direction of the cable varies with the winding angle θ. This also leads to change in size of the air gaps between ReBCO tapes. Taking this into consideration, width for each tape after the helical winding in the horizontal direction is redefined as,

$$\frac{W_1}{|\cos\theta|} = W_2 \qquad \text{Equation 3. 15}$$

where W_1 is the width of a straight ReBCO tape, and W_2 is the width of the tape in the horizontal direction of the cable after the winding fabrication. Cross-sectional geometry of this model is shown in Figure 3. 16 (a). The width of each single straight ReBCO tape used here is 4 mm, and the winding angle of the cable presented in Figure 3. 16 is 40°. Thus, from Equation 3.13, the tape width on the cross section of CORC cable in the Advanced 2D model is 5.22 mm after the winding fabrication. The size of air gaps between coated conductor is around 1.7 mm. The helicity of CORC cable also leads to components of transport current in both the axial and horizontal direction. Magnitude of these current components are affected by winding angle of the cable, which is considered in this model as well. Instead of directly applying a current density into z-direction (which is the conventional way to apply a transport current in a 2D model), the transport current density is decomposed into y- and z-components as follows,

$$J_{trans} = \begin{cases} J_z \sin\theta & \text{in } y \text{ direction} \\ J_z \cos\theta & \text{in } z \text{ direction} \end{cases} \qquad \text{Equation 3. 16}$$

Where J_z is the value of applied current density, while θ is the winding angle of the cable. This decomposition of the transport current is applied to the Advanced 2D model to represent the spiral structure of CORC cable. Cross sections of Cable A and Cable B in the 2D Advanced model are presented in Figure 3. 16 (a).

(b) *The Original 2D CORC cable model.* This model is built in a conventional way and serves as a reference. Influence of winding angle on the size of the air gap between coated conductors is ignored in this 2D model. Cross sections of Cable A and Cable B in the 2D Original model are presented in Figure 3. 16 (b). Width for each tape in the cross section of cable is 4 mm, which is the same with the straight ReBCO tape width. The size of the air gap between tapes is around 2.9 mm, which is much larger than that in the Advanced 2D T-A model. Difference in size of the air gap may eventually lead to different AC losses in the cable. This will be simulated and analysed later in detail. Two air gap sizes are classified into 'narrow gap' and 'wide gap'. Transport current density is directly applied into each ReBCO tape along z-direction only.

(c) *The Decomposed 2D CORC cable model.* Based on the single-variable method, same assumption is made to ignore the influence of winding on the size of air gap in this model. The cross-sectional geometry of this 2D model, as can be seen in Figure 3. 16 (b), is exactly the same with that of the Original 2D model. The only difference between the Decomposed and the Original 2D model is that the transport current is decomposed into y- and z-direction respectively in the Decomposed 2D model. For more intuitive comparison, differences of three 2D models are listed in Table 3. 4.

For comparison, the 3D T-A CORC cable model mentioned in Section 3.3 is used as a reference model to validate the results obtained from 2D models.

(a) The Advanced 2D model

(b) The Original & Decomposed 2D model
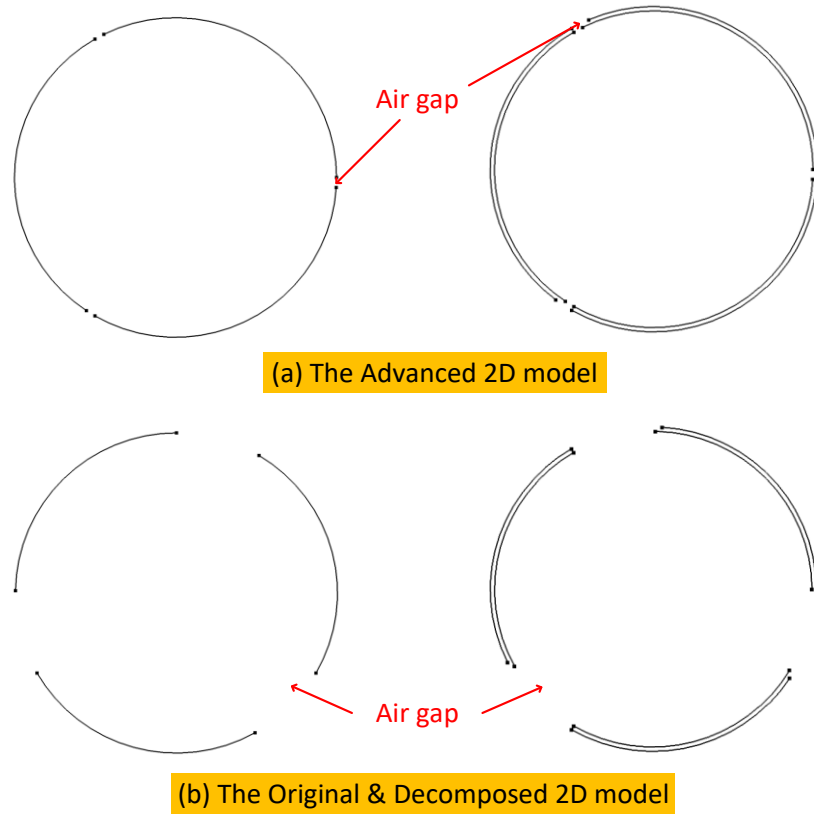
Figure 3. 16 Cross section of (a) the Advanced 2D model; and (b) the Original and the Decomposed 2D models. θ = 40°.

Table 3. 4 Comparison of the specifications of three 2D models.

	The Original 2D	The Decomposed 2D	The Advanced 2D
Transport current	Directly applied	Decomposed	Decomposed
Air gap	Wide gap	Wide gap	Narrow gap

3.3.2 Mesh optimization

In the aim of reducing the memory requirement during modelling process, as well as to fasten the computation time, an accurate and efficient mesh method is vital. A case study of simulating a single straight ReBCO tape in both 2D and 3D ways was proposed in this part of the research. It focuses on optimizing the meshing for ReBCO tapes to reduce the computation time, while achieving the best agreement between the 2D and 3D T-A CORC models.

The ReBCO tape used here is the same tape as which is used to construct the CORC cable, with all parameters mentioned above in Section 3.2. Basic geometry of the 3D and 2D straight tape model

is shown in Figure 3. 17 (a) and (b) respectively. A cylinder was used as the outer boundary of the 3D T-A model. The tape shape that is coloured in purple in Figure 3. 17 (a) is the straight ReBCO tape in the 3D T-A model, and it is turned into a thin line in the 2D cross-sectional T-A model. Width of the tape was divided into different numbers of mesh segments (20, 30, 40, 50 and 60) in both 2D and 3D models, while a fixed number of mesh segments was applied along the tape length in the 3D model. For convenience, the word 'segment' in the following study represents the number of mesh segments along the tape's width direction. Then, by calculating and comparing the AC losses obtaining from two models, ideal value(s) for the meshing of ReBCO tapes under various situation is obtained.
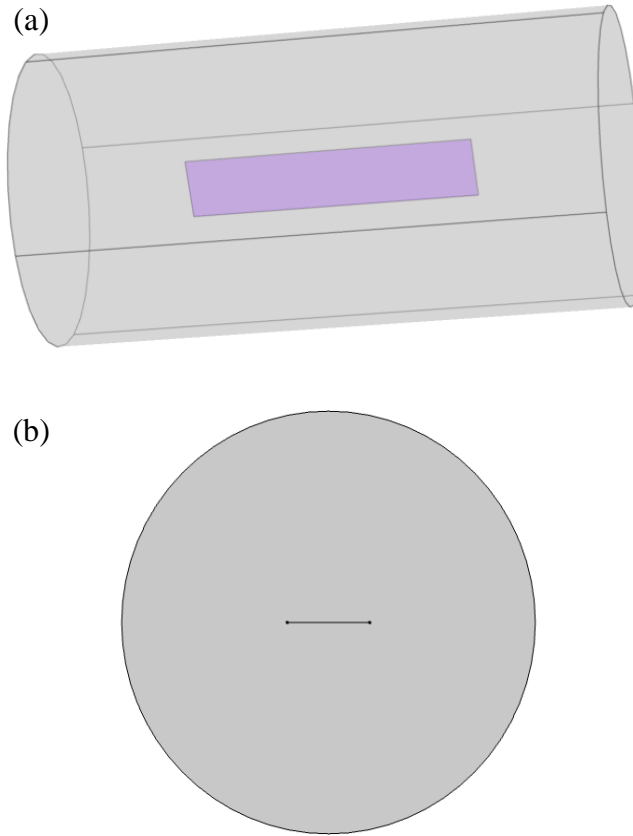
Figure 3. 17 Geometry of a single straight ReBCO tape in (a) the 3D T-A model; and (b) the 2D T-A model. The single straight ReBCO tape colored in purple in (a) the 3D model is turned into a thin line in (b) the 2D model.

Figure 3. *18* shows the transport loss of the ReBCO tape per cycle time under different transport currents in both 2D & 3D models. Different values of operating currents (I_{op} = 75, 90, 105, and 120 A) were applied to both models (Critical current I_c is 150 A in this case). It is clear that the losses

calculated from the 2D model is always a bit lower than that obtained from the 3D model, this means that the simplification of cable structure leads to lower calculated AC losses in 2D model. When the segment is 20 or 30, the coarse mesh leads to inaccurate value of loss, which is normally much larger than the actual loss generated in the cable. Relatively stable outcome can be achieved by increasing the mesh number to around 40 to 50 on the tape width. Table 3. 5 then lists the relative errors between the transport losses calculated in 2D and 3D models. For more intuitive comparison, the relative errors are also plotted in Figure 3. 19. It is obvious that low value of I_{op}/I_c leads to higher calculation error, while the relative error between 2D and 3D models in the case of $I_{op}/I_c = 0.8$ is reduced to no larger than 1%. From above analysis, 40 is a perfect number of segments for $I_{op}/I_c \leqslant$ 0.6 to minimize the relative error between 2D and 3D model, when segment equals 50 should be used for higher value of I_{op}/I_c, which is I_{op} larger than 105 A in this case.
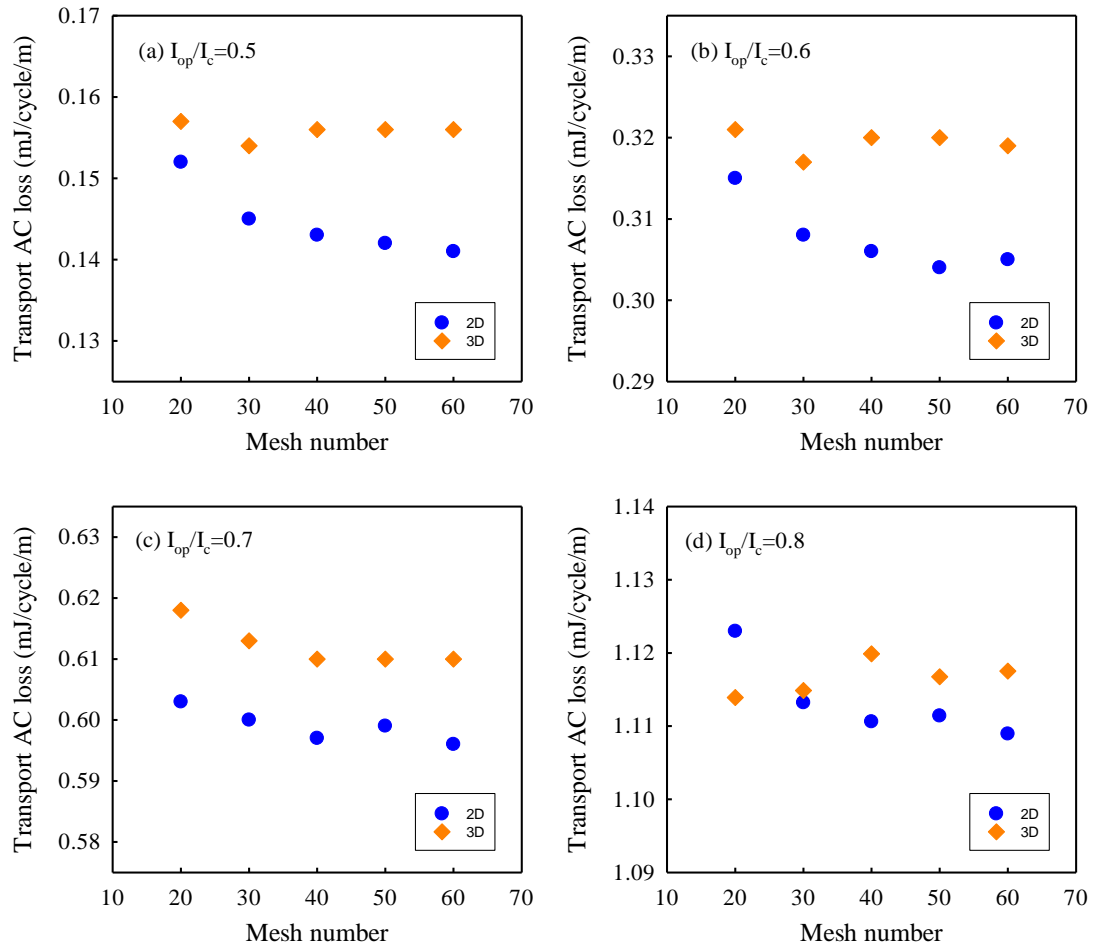
Figure 3. 18 Transport AC losses per cycle time of a single ReBCO tape under different transport currents (I_{op} = 75, 90, 105,120 A) against number of mesh segments along the tape width direction in both 2D and 3D models.

71

Table 3. 5 Relative errors of transport AC losses between 2D and 3D models, I_c = 150 A.

I_{op}/I_c Mesh No.	0.5	0.6	0.7	0.8
20	3.28%	1.87%	2.33%	0.81%
30	5.27%	2.84%	2.18%	0.15%
40	8.27%	4.38%	1.98%	0.83%
50	8.76%	5.00%	1.78%	0.48%
60	9.09%	4.51%	2.35%	0.77%
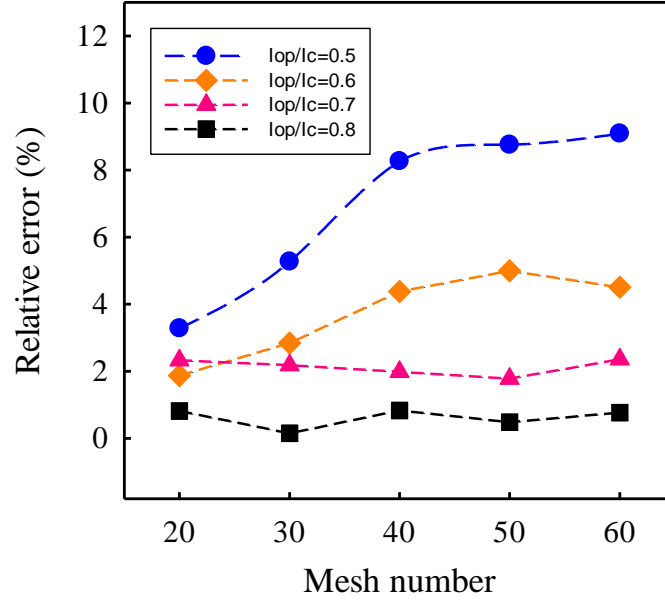
Figure 3. 19 Relative errors of transport AC losses between 2D and 3D models, I_c = 150 A.

Figure 3. 20 plots the magnetization loss of the tape per cycle time in both 2D and 3D models under external magnetic fields of 5mT, 10 mT, 20 mT, and 40 mT. When the external background fields are relatively low (compared with 40 mT in this case), from Figure 3. 20(a), (b) and (c), change of mesh from 20 to 30 leads to a sharp decline in magnetization losses obtained from 2D model, which means 20 is not fine enough for getting a precise result. Also, the relative errors of magnetization losses calculated from 2D and 3D models are listed in Table 3. 6 and presented in Figure 3. 21 as well. From Table 3. 6, when B_{ext} = 5 mT, mesh = 50 results in a relative error as small as 0.27% between 2D and 3D model. With larger external background fields (10, 20 and 40 mT in this case), mesh = 40 can effectively minimize the relative error between two models. Relative errors in Table 3. 6 also demonstrates that, under high external magnetic field, accuracy of the 2D model is almost the same with the 3D one, thus the total number of mesh can be accordingly reduced to fasten the calculation time.

This case study shows that the coarse mesh will eventually result in inaccurate loss value. However, finer mesh does not necessarily lead to more accurate result, as it might give rise to other problems such as abrupt gradient between time steps, endless computation time, or bad convergence. It is important to choose a proper value of mesh number to obtain precise simulation outcome. In following study on the 2D T-A CORC simulation, for low transport current or low external magnetic field, 50 is a proper value of mesh segments along the tape width direction, while for higher I_{op} or B_{ext}, 40 is a sufficient number of mesh segments that is fine enough for simulation of CORC cable. Figure 3. 22 plots the final mesh of the CORC cable in both 3D and 2D views.
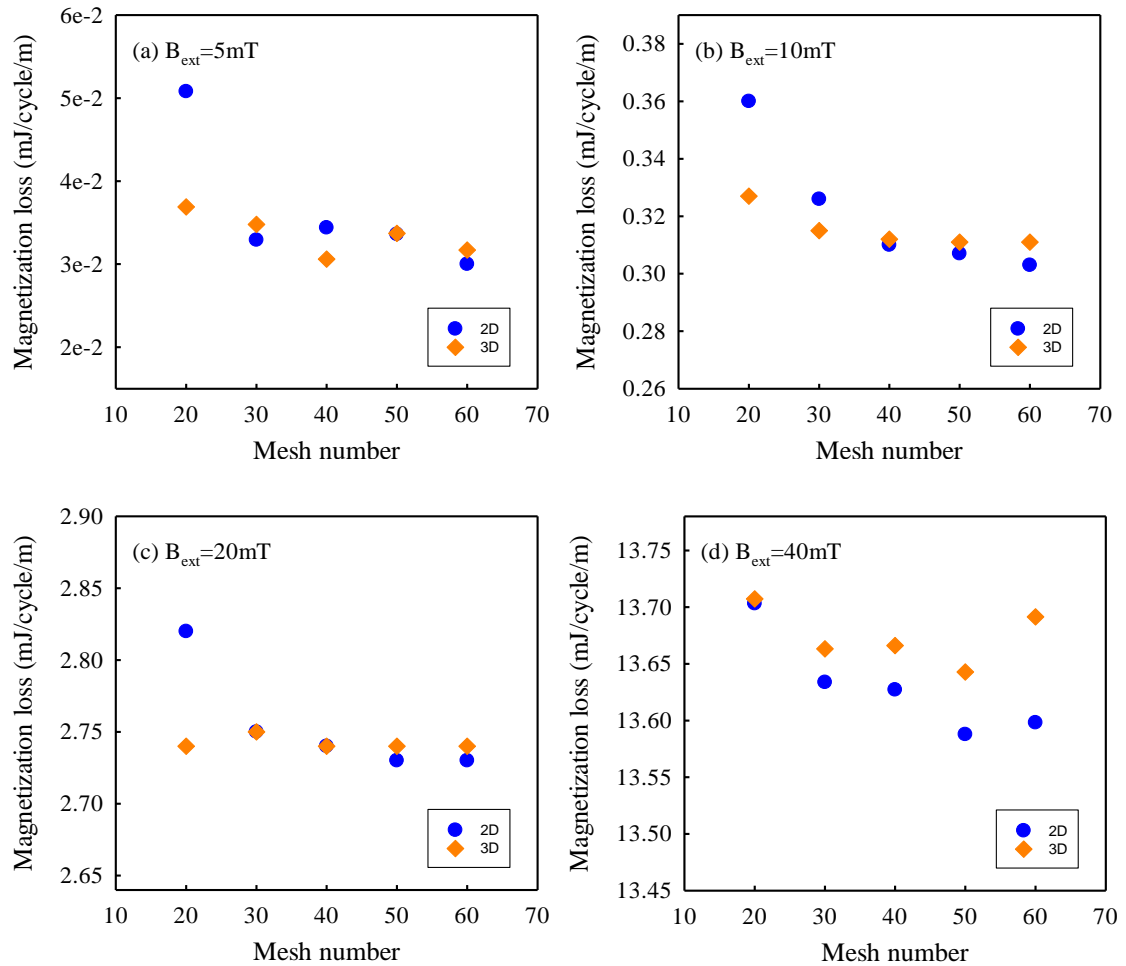
Figure 3. 20 Magnetization losses per cycle time of a single ReBCO tape under different external magnetic fields (B_{ext} = 5, 10, 20, 40 mT) against number of mesh segments along the tape width direction in both 2D and 3D models.

B_{ext} Mesh No.	5 mT	10 mT	20 mT	40 mT
20	27.46%	9.21%	2.84%	0.03%
30	5.77%	3.36%	0.18%	0.22%
40	11.07%	0.67%	0.05%	0.29%
50	0.27%	1.35%	0.33%	0.41%
60	5.74%	2.73%	0.66%	0.69%
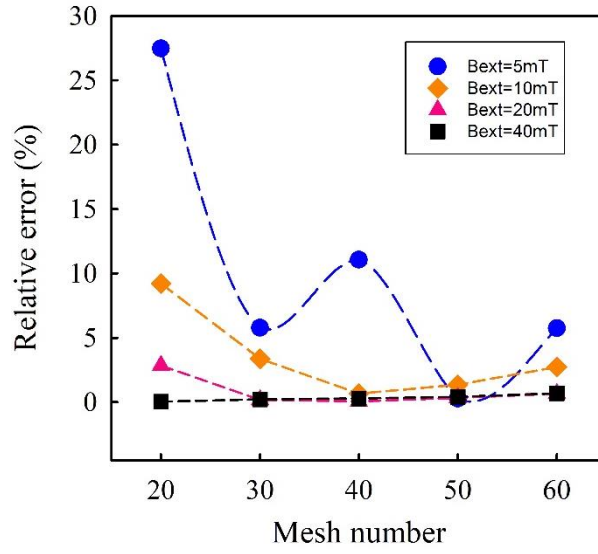
Figure 3. 21 Relative errors of magnetization losses between 2D and 3D models.

(a)

(b)
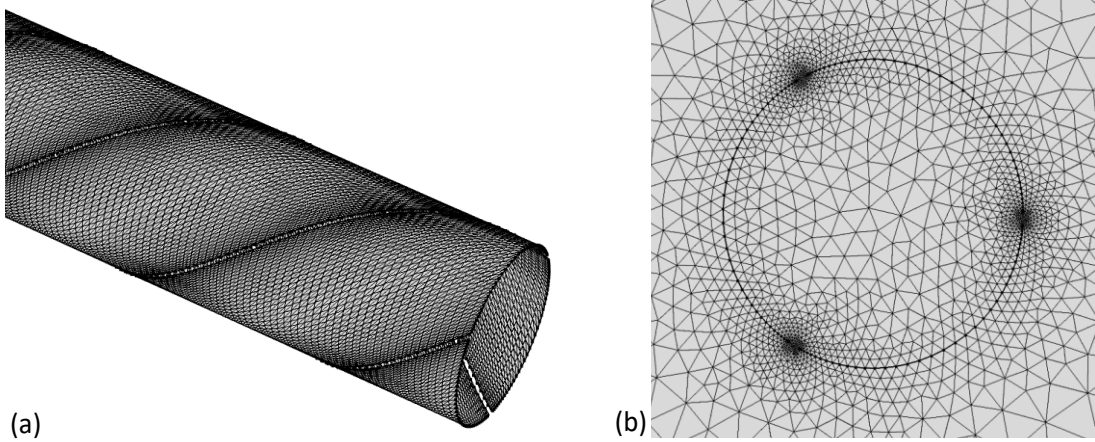
Figure 3. 22 Meshing of the CORC cable in (a) the 3D T-A model; and (b) the Advanced 2D

T-A model. Number of segments along the width direction is 40.

3.3.3 Results and discussion

3.3.3.1 AC transport loss

For a persuasive and qualitative comparison between the 2D and 3D models, for ReBCO tape with a critical current I_c of 150 A, magnitude of the applied transport current I_{op} is fixed at 120 A in this part of study, according to the mesh analysis above. It is to eliminate differences caused by the low rate of I_{op}/I_c between two models. Different winding angles (2, 5, 10, 20, 30 and 40 degrees) were applied to build the cable sample Cable A. The transport AC loss in per unit length of the cable under one cycle time (J/cycle/m) is calculated from the 3D model by using the surface integration function. Transport loss that is integrated in the 2D model, however, is in per unit length of the tape. Relationship between these two values can be expressed as follows,

$$Q_{tapes} = Q_{cable} \cos \theta \qquad \text{Equation 3. 17}$$

here, Q_{tapes} is the total energy loss in per unit tape's length that is generated from three tapes of the cable. Q_{cable} is the loss in per unit cable's length. θ represents the winding angle of the cable. Dependence of the transport loss for one AC cycle on the winding angle θ of Cable A is shown in Figure 3. 23.

Since the Original 2D model doesn't decompose the transport current as regards the winding angle, it can be considered as a straight-taped cable. Result from the original 2D model does not vary with the winding angle and is plotted as a straight dotted line for the purpose of reference. Value of loss that is available from the 3D model has been transferred into unit length of tape. From Figure 3. 23, when $\theta = 2°$, CORC cable can be approximated as a straight-taped cable without helical cabling structure. Thus, results from all 2D models agreed with each other well at this point. The highest transport losses, with a value of 1.2 mJ/cycle/m and 1.44 mJ/cycle /m, are produced in 2D and 3D cases respectively. With the increase of winding angle, loss produced by a transport current of 120 A in both the Decomposed and the Advanced 2D models are decreasing, which follows the trend of loss against winding angle in the 3D model. This is because the transposition among ReBCO tapes, which is much greater in a CORC cable with larger winding angle, can effectively reduce the AC loss. However, the transport AC loss in the

Decomposed 2D model decreases slowly with the increasing winding angle, from 1.21 mJ/cycle m^{-1} to 0.89 mJ/cycle/m. When $\theta = 40°$, value of loss in the Decomposed 2D model is almost an order of magnitude larger than that in the 3D model, which shows a lack of accuracy of this 2D model. Meanwhile, the reduction of transport AC loss in the Advanced 2D model is rapid, from 1.18 mJ/cycle/m to 0.04 mJ/cycle/m, which is similar to the transport AC loss trend in 3D case. Cause of this discrepancy is that, the Decomposed 2D model only considers the direction of helically flowing current, while the actual size of air gap after the winding fabrication is not presented in the model. This phenomenon indicates that, size of the air gap between tapes plays a more important role in the variation of AC loss in a CORC cable. The Advanced 2D CORC model well reproduces the overall trend of loss with the increase of winding angle obtained from the 3D model, while results of other 2D models are not in line with the 3D reference.

The distribution of normalized current density (J/J_{norm}) of Cable A in three 2D models is presented in Figure 3. 24. The distribution of current density in one of the tapes in Cable A in the 3D model is presented in Figure 3. 25. As explained above, since the CORC cable is symmetrical, the other two tapes share the same distribution of current density. Then, for a more intuitive comparison, three different cross sections are chosen along the axial direction of the 3D CORC cable model and are plotted in Figure 3. 25(b) to present the current density distribution in 2D view. As can be seen, the cross sections in both the Original and Decomposed 2D models have larger tape-to-tape air gaps compared with that in the Advanced 2D models, for these two models use the width of ReBCO tape without taking the winding into consideration. Also, the distributions of the current densities in these two 2D models are similar. Compared with the 3D case, they both have deeper penetration depth on both edges of the tape and lower current density in the middle of the tape. Differently, the current density distribution in the Advanced 2D model, as can be seen in Figure 3. 24(a), obviously displays the most consistent distribution with that in the 3D model. Combining above factors, the cause of such discrepancy in three 2D models is the size of air gaps between the tapes. Although the flowing direction of the transport current is considered in the Decomposed 2D model, the impractical tape-to-tape air gaps still lead to remarkable errors in the simulation results. The Advanced 2D

model, on the contrary, applying the practical size of air gaps to the model geometry, results in a good agreement between the 2D and 3D simulation.
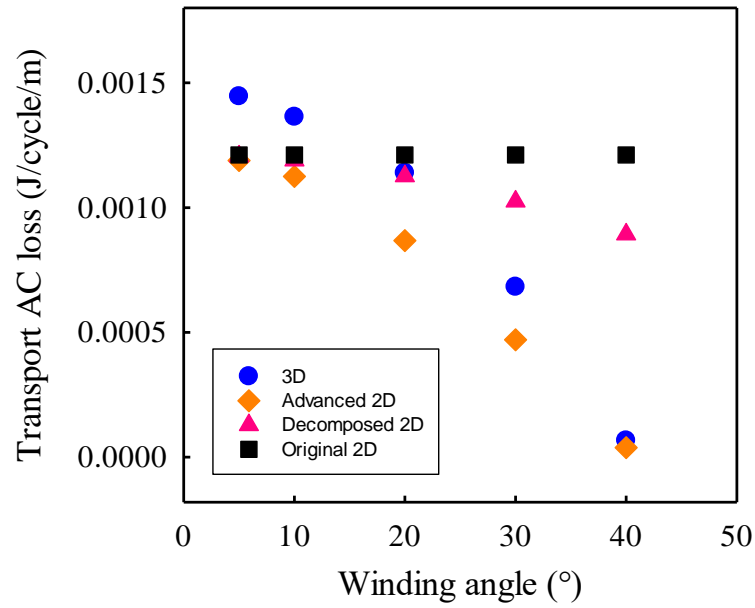
Figure 3. 23 Transport AC losses of Cable A for one AC cycle against different winding angle situations (θ = 2, 5, 10, 20, 30 and 40 degrees). I_{op} = 120 A, B_{ext} = 0 T, f = 50 Hz.

t=T/4

(a) Advanced 2D   (b) Original 2D   (c) Decomposed 2D
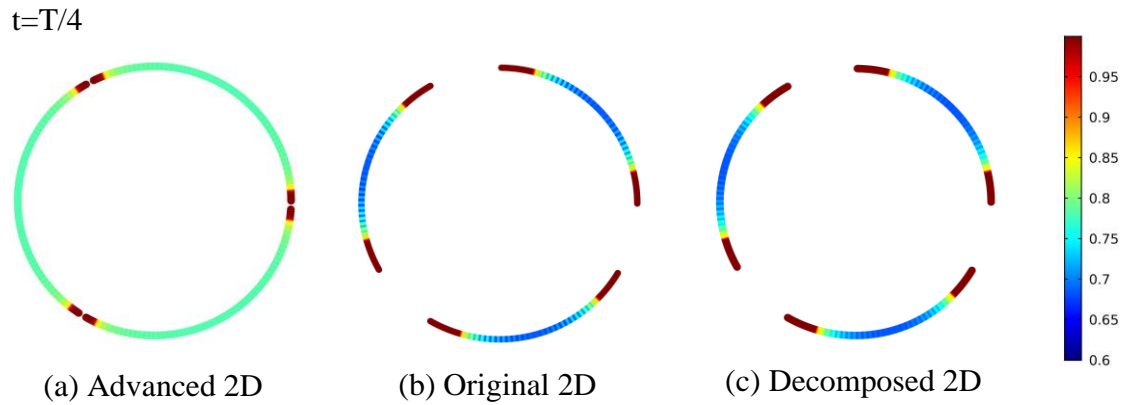
Figure 3. 24 Distribution of normalized current density (J/J_{norm}) of Cable A in the (a) Advanced; (b) Original; (c) Decomposed 2D models. t = T/4, θ = 40°, I_{op} = 120 A, f = 50 Hz, B_{ext} = 0 T.

77
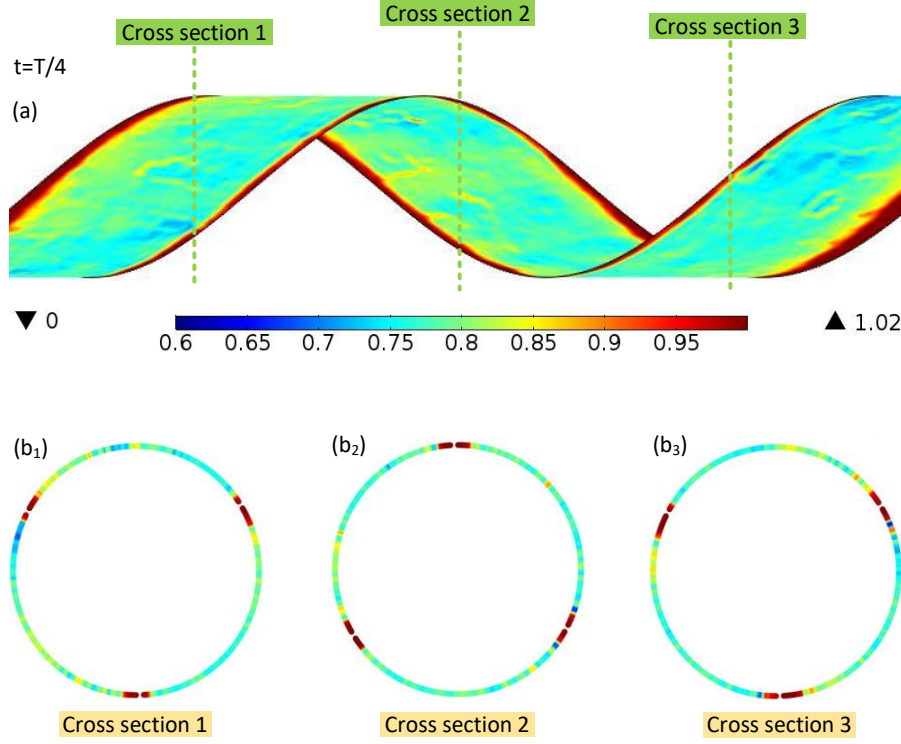
Figure 3. 25 Distribution of normalized current density (J/J_{norm}) of Cable A in (a) the 3D view of a single tape in the cable; (b) three cross-sections along the axial direction of the 3D model. $t = T/4$, $\theta = 40°$, $I_{op} = 120\ A$, $f = 50\ Hz$, $B_{ext} = 0\ T$.

3.3.3.2 Magnetization AC loss

In this section, we analysed the magnetization AC losses of both Cable A and Cable B under different background magnetic fields in 2D models. For the purpose of simplicity, only the external background field is applied to the cable samples, no transport current applied. Thus, the Decomposed 2D model, which only considers the decomposition of transport current, is not considered in this part of the research. Figure 3. 26 presents the magnetization AC loss against various background magnetic fields in two 2D models and a 3D model. It is obvious that when Cable A is under low magnetic field, i.e. lower than 30.4 mT, the Advanced 2D model outputs magnetization loss that better matches the result in the 3D model. The relative error between the Original 2D and 3D model reaches its highest value, 96.41%, at the lowest external field 1.56 mT, while the relative error between the Advanced 2D model and 3D one at this field is reduced to 85.71%. Then, although the loss generated in the Original 2D model becomes more consistent with

the increase of the external magnetic field, it still shows a relative error no less than 35.79%. Meanwhile, the Advanced 2D model has already managed to reduce the error to 3.27% only. Magnetization loss generated in Cable B shows a similar trend with the single-layer situation at a field lower than 30.4 mT, relative errors in Advanced 2D model are much lower than that in the Original 2D model. When Cable B is under a high external magnetic field, the ReBCO tapes in the cable experience almost fully penetration, the error caused under this field is thus unstable. When the field is above 67.1 mT, both 2D models generate almost the same magnetization loss with the 3D case.
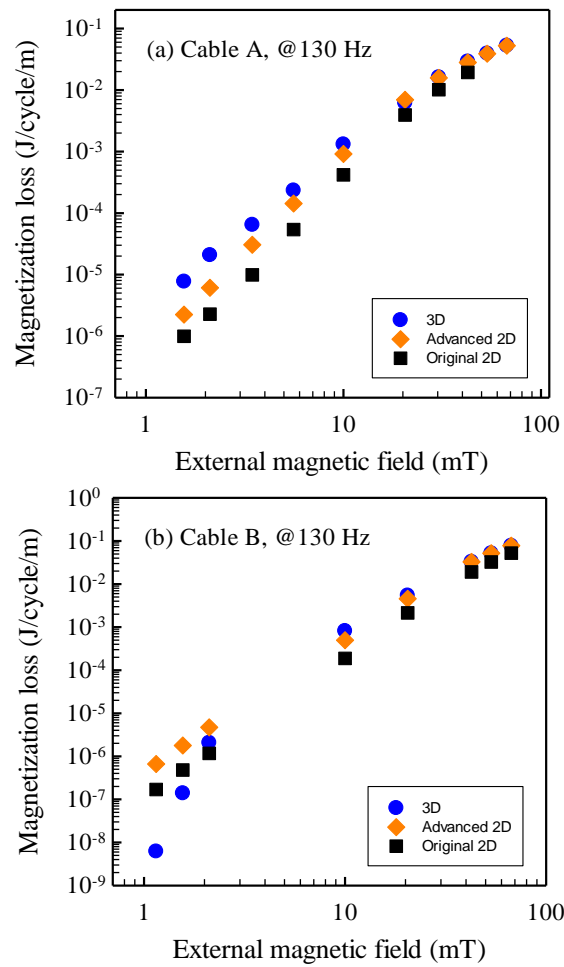
Figure 3. 26 Magnetization loss of (a) Cable A; and (b) Cable B against background magnetic fields. I_{op} = 0 A, B_{ext} = 1.15~67.1 mT, f = 130 Hz, θ = 40°.

The distribution of current density, as well as the distribution of the magnetic field of Cable A, in both 2D models and 3D models under an external magnetic field of 20.5 mT, is shown Figure 3. 27 and Figure 3. 28. At B_{ext} = 20.5 mT, the field penetration depth in the Original 2D

model does not agree with that in the 3D model, for more field lines penetrate through the larger air gaps (compared with the 3D one) instead of the ReBCO tapes, while in the 3D cases, the tape is almost fully penetrated due to the high magnetic field. On the other hand, the normalized current density in the Advanced 2D model shows a similar distribution with that in the 3D model, and penetration of magnetic field lines is almost the same as well. This means, for a single-layer CORC cable case, the Advanced 2D model can better simulate the AC loss performance in the cable.

Figure 3. 29 and Figure 3. 30 shows the comparison of current density distribution and magnetic field distribution in Cable B between the two 2D models and the 3D reference model. Since the air gaps between the adjacent layers in Cable B are perfectly aligned with each other, and two layers have same winding direction, the outer layer in Cable B has a strong shielding effect in the inner layer. Thus, the outer layer of Cable B experiences more flowing current compared with the inner layer. Also, under the same external field, penetration area in Cable B is much smaller compared with that in Cable A. The same with Cable A's case, the penetration depth in the Original 2D model does not agree with that in the 3D model. The Original 2D model also outputs lower normalized current density in the middle of each tape, while the normalized current density shown in Figure 3. 29(a) virtually agreed with the cross-section 2 in the middle of Figure 3. 30. Distribution of the magnetic field lines in the Advanced 2D model perfectly reproduces the 3D situation as well. From the above analysis, the accuracy and reliability of the Advanced 2D model are proved, while the Original and the Decomposed 2D model both show some major calculation errors due to the impractical cable geometry.

t=T/4

(a) Advanced 2D   (b) Original 2D
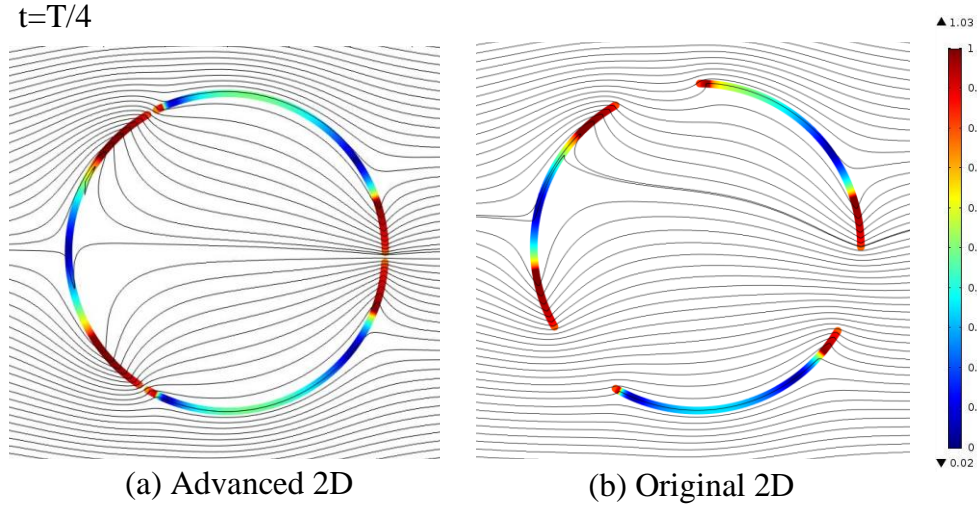
Figure 3. 27 Distribution of normalized current density and magnetic field lines of Cable A in

(a) the Advanced 2D model; (b) the Original 2D model. B_{ext} = 20.5 mT, f = 130 Hz, t = T/4.
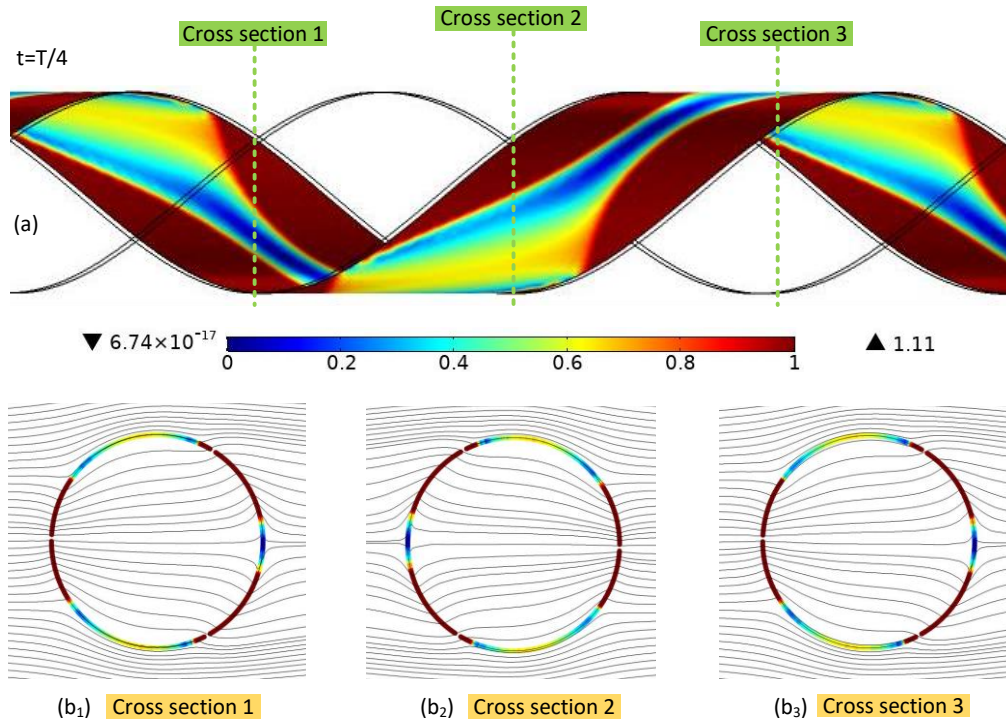
Figure 3. 28 (a) Distribution of current density in one of the ReBCO tapes in Cable A and (b)

distribution of normalized current density (J/J_{norm}) and magnetic field lines in three cross

sections along the axial direction of Cable A in the 3D model. B_{ext} = 20.5 mT, f = 130 Hz, t =

T/4.

81

t=T/4

(a) Advanced 2D   (b) Original 2D
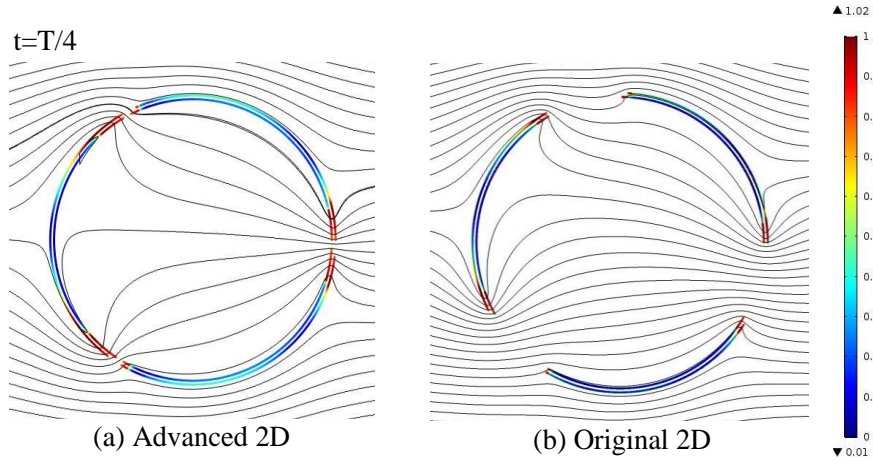
Figure 3. 29 Distribution of normalized current density and magnetic field lines of Cable B in

(a) the Advanced 2D model; (b) the Original 2D model. B_{ext} = 20.5 mT, f = 50 Hz, t = T/4.

Cross section 2

Cross section 1   Cross section 3

(a_1) Inner layer

(a_2) Outer layer

(b_1) Cross section 1   (b_2) Cross section 2   (b_3) Cross section 3
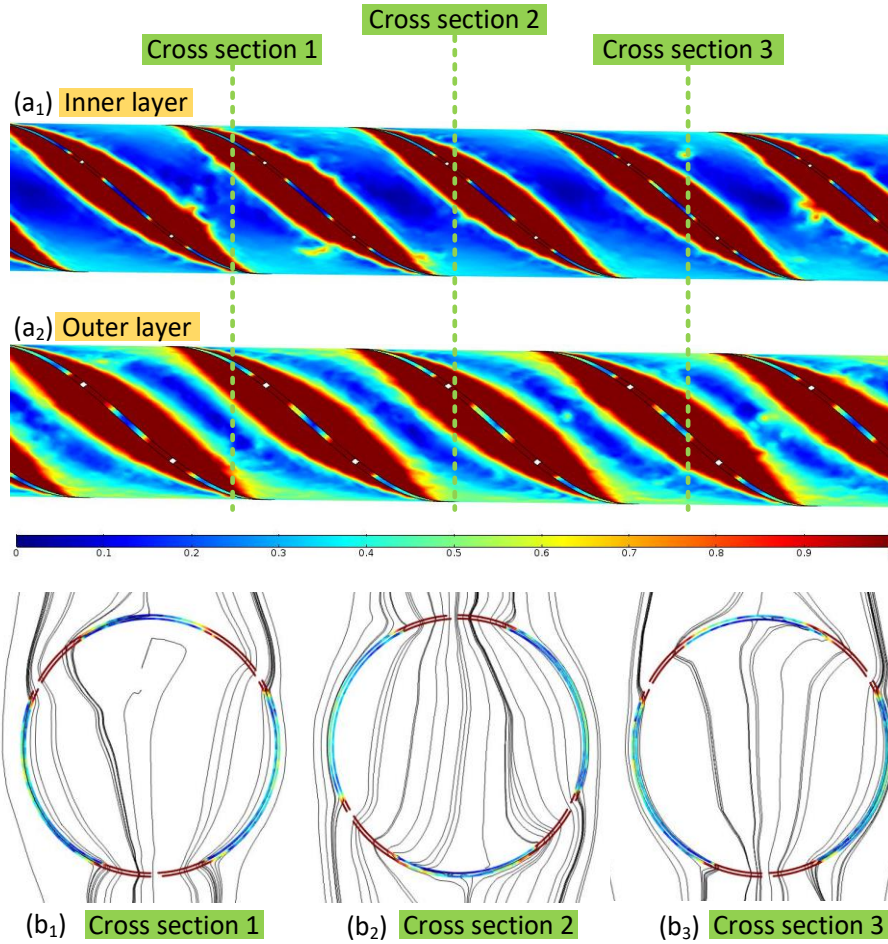
Figure 3. 30 (a) Distribution of current density in one of the ReBCO tapes in Cable B and (b)

distribution of normalized current density (J/J_{norm}) and magnetic field lines in three cross

sections along the axial direction of Cable B in the 3D model. B_{ext} = 20.5 mT, f = 50 Hz, t =

T/4.

3.3.3.3　Solution time of the 2D models

To prove the efficiency of the newly proposed 2D model, we then compare the solution time of 2D and 3D models. Table 3. 7 shows the model specification and solution time for Cable A in 2D and 3D CORC models under a transport current of 120 A. As presented previously in Figure 3. 22, in 2D models, each ReBCO tape line is divided into 40 or 50 mesh segments; then the whole geometry (along with the air space) is meshed using free triangular elements. In the 3D model, the ReBCO tape uses free tetrahedral meshing, with the width of tape meshed to 40 segments. The mesh elements in the Advanced 2D model are slightly higher than that in the other two 2D models. The solution time of the Advanced 2D model is longer than that of the other two 2D models. However, it still dramatically shortens the computation time of the CORC cable, from days to less than half-hour, compared with the 3D model.

Model specification and solution time for Cable A under an external magnetic field of 20.5 mT are presented in Table 3. 8.Mesh elements in the Advanced 2D model are slightly higher than that in the Original 2D model, and the solution time is significantly reduced. Thus, a conclusion can be made that the novel Advanced 2D T-A model successfully manages to simulate the AC loss of multi-layer CORC cable accurately, meanwhile considerably shortened the solution time compared with the 3D model. Thus, it is perfect to use the Advanced 2D model for AC loss calculation.

Table 3. 7 Model specification and solution time for Cable A when transport current is applied.

	Advanced 2D	Original 2D	Decomposed 2D	3D T-A model
Number of elements	6096	3546	3546	372828
Transport current (I_c=150 A)	120 A	120 A	120 A	120 A
Time interval	0.06s	0.06s	0.06s	0.06s
Solution time	1757 s	505 s	641 s	1 day 37 mins

Table 3. 8 Model specification and solution time for Cable A when external magnetic field is applied.

	Original 2D	Advanced 2D	3D T-A model
Number of elements	3546	3958	372828
Background field	20.5 mT	20.5 mT	20.5 mT
Time interval	0.023 s	0.023 s	0.023 s
Solution time	589 s	530 s	1 day 9 hours 42 mins

3.4 Summary

Chapter 3 proposed two brand-new CORC cable models that are built based on the T-A formulation: a 3D T-A CORC model and an Advanced 2D T-A models. Starting from the introduction of a new set of formulation, the T-A formulation, a novel 3D T-A model was proposed in the first part of this chapter. To first valid the T-A formulation, we built a simple 2D CORC model based on the T-A formulation and the well-validated H-formulation respectively. Comparison between the AC loss obtained from these two models proved that the T-A based model outputs the same simulation results with the H-based model. Then, we applied to T-A formulation to a 3D model, in the aim of solving the modelling difficulty caused by the high aspect ratio of the ReBCO tape, as well as reducing the computation time. The 3D T-A model is then validated by comparing the calculation results with previously-published experimental data. The calculated magnetization AC loss well agreed with the measurement, which well proved that this 3D T-A model is a powerful simulation tool for the AC loss calculation of the CORC cable. Using this 3D T-A model, we then further analysed the AC loss, including the transport AC loss and the magnetization AC loss of two CORC cable samples; a single-layer CORC cable and a double-layer CORC cable. The influence of winding angle on the AC loss of cable was then studied in details. Results show that the AC loss decreases with the increase of winding angle. To further shorten the solution time of the CORC cable model and simplifying the simulation, we proposed three different 2D T-A models for the AC loss calculation of the CORC cable. After the mesh optimization, we calculated both the transport AC loss and the magnetization AC loss using three 2D models and compared the results with that

obtained from the 3D model. The conclusion is made that, the Advanced 2D model, by considering the direction of flowing transport current as well as the dependence of air gap between tapes on the winding angle, manages to accurately and efficiently simulate multi-layer CORC cables. Also, another important conclusion is that the air gap between ReBCO tapes has a great impact on AC loss of CORC cable, thus the size of the air gap between tapes must be accurate and practical during the modelling process.

Chapter 4. Quench behaviour analysis of CORC cable

4.1 Introduction of quenching

Quenching, as a local overheating phenomenon, is one of the most severe faults that could happen during the operation process of superconducting devices. It often appears as a resistive state transition in superconducting magnets. When quench happens, the temperature and voltage both increase, the electromagnetic forces are induced, and the cryogen pressure increases due to the generated Joule heat [153]. This phenomenon is usually caused by an accidentally occurring local hotspot on the magnet. There are several factors, including varying applied magnetic field, external heat disturbance and operating transport current, that can induce a local hotspot on a superconductor [154]. To illustrate the process of quenching, we choose the case when the operating current is locally larger than the current threshold (I_c) of the superconducting magnet, due to which that causes rapid temperature rise. Normally, when there is only a slight temperature disturbance, for instance, a local temperature that is above the bath temperature, the induced heat will flow along the magnet and dissipate into cryogen bath, eventually chilling the temperature disturbance on the magnet. However, when a certain temperature rise appears, the considerable amount of circulating current in the magnet rapidly creates Joule heat on a certain hotspot, forcing the overheated region back into normal resistive state, this region is thus called 'the normal zone' in magnet [22, 155]. If this local temperature rise is large enough, it can also lead to a possible chain reaction to raise the temperature of the surrounding regions to an extent that these regions are transited into the normal state as well [156]. This may eventually drive the whole superconductors into quench, even leading to irreversible damage. The whole process of quenching only takes a few seconds, depending on the size of the superconducting devices. The entire superconductor then losses its superconductivity and becomes a normal conductor [25]. Needless to say, quenching is a significant risk that cannot be ignored during the operation of superconducting devices. It is of vital importance to understand the quench behaviour of superconductors, in order to detect a quench rapidly and protect the superconducting magnet from burning out. However, the quench detection and protection must be a part of the construction of a safely designed magnet system, rather than to be added as an

individual part, for the protection of quench involves some main design parameters of the whole system.

The normal zone propagation velocity v_p (NZPV) is one of the useful parameters that characterize the quench behaviour of a superconductor. It is also called 'quench propagation velocity'. As mentioned above, the overheated local region, in which a superconductor transits into normal resistive state, is defined as 'normal zone'. The NZPV represents the speed that the normal zone propagates along the superconductor with, following the temperature rise that generates Joule heat [157]. This velocity increases with increasing current. It also depends on the geometry and physical properties of the magnet, as well as the cooling bath conditions. Generally, high propagation velocity means that the area of normal zone enlarges fast along the magnet, dissipating the generated Joule heat to reduce the possibility of quench-induced damage [157]. Thus, for the construction of a superconducting magnet, a high NZPV is a desirable feature. Numerous studies were carried out regarding the NZPV of low temperature superconductors, such as NbTi and Nb$_3$Sn [157, 158]. However, material properties of high temperature superconductors are quite different from the LTS, and the temperature range is wider in HTS. Thus, the normal zone propagation phenomenon in HTS is much more complicated, compared with the LTS case. Research has been conducted to analyse the NZPV in HTS in both experimental and numerical ways [17, 159].

Another characteristic used to describe the quench behaviour is the minimum quench energy ε_e (MQE). Definition of the MQE is the minimum value of heat energy, which causes a disturbance that leads to an infinite expansion of normal zone in a superconducting magnet. Value of the MQE is affected by many factors, including the characteristics of the superconductors, the cooling bath conditions, and the heat pulse that is imposed on the conductor to induce hotspot.

Numerous researches have been conducted to study the quench behaviour of superconducting magnets. Researchers started with single tape/wire situation. The quench behaviour of a single commercial Ag/Bi-2212 wire was studied experimentally in [160]. The outcome shows that the I_c degradation of Ag/Bi-2212 wire largely depends on the temperature of the local hotspot. A new quench detection method that is based on the voltage-tap is proposed and applied to a solenoid which is constructed using Ag/Bi-2212 wire [161]. The analysis shows that methods that effectively enhance the thermal coupling between layers are preferred in the design of superconducting magnet.

The thermal stability and quench behaviour of YBCO CCs at 4.2 K in self-field was experimentally investigated in [162]. This HTS material is proved to have better stability than MgB$_2$. It also has slower NZPV and higher MQE, compared with the LTS conductors. Another result is that the I_c of the superconductors also has a great influence on the quench behaviour of YBCO CCs.

There are several numerical studies related to the quench behaviour analysis as well. An experimentally validated 3D model was proposed to study the influence of the design parameters on the quench behaviour of YBCO coated conductors (CCs) [163]. The simulation results prove that thickness, as well as the thermal conductivity of the stabilizer, is of great importance on the quench behaviour of YBCO CCs, and the thickness of the YBCO layer affects the NZPV.

However, the quench behaviour of CORC cable is quite different from above researches, not only for the geometry of CORC cable is complicated, but also because the ReBCO tapes in the same layer are soldered together using copper leads, which means there are terminal contact resistances (TCRs) between individual tapes and the cable terminations. Some research have proved that the inhomogeneous TCRs significantly influence the current distribution and redistribution among tapes in the cable, eventually affecting the quench behaviour of CORC cable [164, 165]. In the process of the hotspot-induced quench, the flowing transport current in each individual tape is forced out by heating and is redistributed to other tapes through the terminal contact resistances. Thus, it is important to optimize the TCRs in CORC cable, in the aim of preventing quenching and increasing stability. However, the current distribution and redistribution in the CORC cable during a quench are difficult to measure. Thus, there is so far only a few research that experimentally study the quench behaviour of a ReBCO CORC cable [164, 166].

Quenching will generate highly non-linear Joule heat in the CORC cable. It could be tough and costly to perform a realistic experiment on quench behaviour analysis of CORC cable. Thus, analysis of the quenching often requires numerical solutions [167]. However, most of the present simulation works focus only on the electromagnetic behaviours of CORC cable [15, 134, 168-170], for the quench modelling involves multi-physics coupling problems that are difficult to tackle with. Therefore, a modelling tool is essential to numerically study the quench behaviour of CORC cable.

4.2 A novel 3D quench model

We proposed a novel 3D quench model in the aim of simulating the quench behaviour of CORC cable. The HTS CORC cable model studied in this chapter is based on the sample cable in [9, 15, 165, 171]. It is a single-layer cable wound with three ReBCO tapes and winding angle of this cable is still 40°. The ReBCO tape used to wind the cable has the same parameters with that in Chapter 3, with a width of 4 mm and a thickness of 0.1 mm. As mentioned in Section 3.1.3, according to the specification of the tape used in this study, the critical current I_c here is 100 A at self-field in 77 K. The operation temperature is set to be 70 K during the simulation process, under which the I_c is around 148 A. More physical properties of the ReBCO tape, including the thermal and electric conductivity, the I-V characteristic curves, and the heat capacity, are obtained from [172]. Detailed specifications of this quench cable model can be seen in Table 4. 1. To properly simulate a local hotspot, we impose a heat pulse on one of the three ReBCO tapes. The geometry of this 3D CORC cable quench model is presented in Figure 4. 1. The heating area (where the heat pulse is imposed on) is also shown in the graph as a parallelogrammatic zone. Size of this heating area is around 26.11 mm^2 [165]. The tape that we impose a heat pulse on to induce a local hotspot is named as 'Tape 1', while the other tapes in the same layer are called 'Tape 2' and 'Tape 3' respectively.

Table 4. 1 Specifications of the CORC cable quench model

	Parameters	Value / Quantity
CORC cable	Inner radius (mm)	2.6
	Winding angle (°)	40
	Pitch length (mm)	19 mm
	Operating current (A)	360
	Tapes per layer	3
ReBCO tapes	Width/Thickness (mm)	4 / 0.1
	Critical current (A)	100 A @ 77 K, 148 A @ 70 K
	Operating current (A)	120
	Thickness of Hastelloy substrate (μm)	50
	Thickness of Copper stabilizer (μm)	20
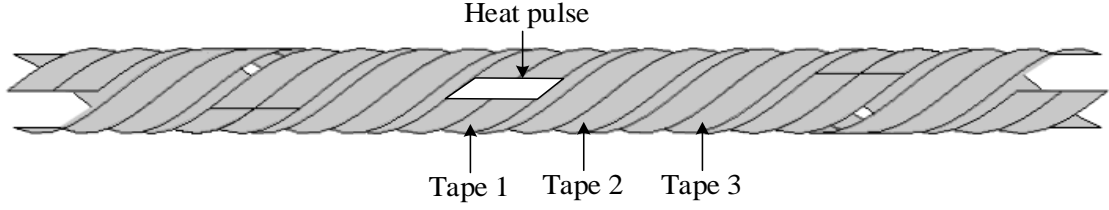
Figure 4. 1 Structure of the single-layer CORC cable. The tape that we impose a heat pulse on to induce a local hotspot is named as 'Tape 1', while the other two tapes are called 'Tape 2' and 'Tape 3' respectively. The white parallelogrammatic area on Tape 1 shows where the heater is added to [173].

4.2.1 Thin sheet approximation

As mentioned in Section 3.2.1, since this quench model is T-A based as well, the thin sheet approximation still applies to ignore any variation of field or temperature along the thickness direction of ReBCO tapes. What differs from the generation of AC loss is that, when a quench happens, there is always current sharing between the superconducting layer and the Copper stabilizer layer. This phenomenon of current sharing needs to be carefully considered during the simulation process.

We gave the cross-section of SuperPower's ReBCO tape that is used in this part of research in Figure 4. 2. There are metallic layers, including the Copper stabilizer and Hastelloy substrate, on both sides of the superconducting ReBCO layer. These layers have much higher resistivity compared with the superconducting layer. Thus, when the ReBCO tape is working under normal superconducting state, the transport current only flows in the superconducting layer. Since we need to consider the thermal behaviour of the ReBCO superconductors in this part of study, the E-J power law is rewritten to include the temperature in;

$$\mathbf{E}(\mathbf{J}) = E_0 \left(\frac{|\mathbf{J}|}{J_c(\mathbf{B}, T_h)} \right)^n \cdot \frac{\mathbf{J}}{J_c(\mathbf{B}, T_h)} \qquad \text{Equation 4. 1}$$

Here, the constant value n and critical electric field E_0 are 31 and $1 \times e^{-4}$ V/m respectively. $\mathbf{B}$ is the background magnetic flux density (background field), $\mathbf{J}$ is the transport current inside the ReBCO

tape, and T_h is the temperature of the ReBCO tape. The critical current density J_c of the ReBCO tape relies on both **B** and T_h.

However, when a local hotspot-induced quench happens, the resistance of the superconducting layer increases rapidly, for the area on the tape gradually turns into normal zone starting from the hotspot. Part of the transport current is then forced out from the superconducting layer and then flows into these metallic layers. Since there is current in the metallic layers as well, we now need to take two parts of resistances into consideration; the resistance in the superconducting layer (R_{su}) and the resistance in the metallic layers (R_{met}). The ReBCO conductor can be considered as an equivalent circuit that has two resistances that is parallel to each other [172, 174, 175]. The equivalent electric circuit is plotted in Figure 4. 3. Based on the Kirchhoff's law, the governing equation of the equivalent electric circuit is expressed as follow,

$$\begin{cases} I_{tot} = I_{su} + I_{met} \\ E_0 \left(\dfrac{I_{su}}{I_c(B,T_h)} \right)^n - I_{met} R_{met}(T_h) = 0 \end{cases}$$

Equation 4. 2

Here I_{tot} represents the overall current that flows in the ReBCO tape, I_{su} is the transport current that only flows in the superconducting layer, and I_{met} is the transport that flows into the metallic layers. T_h here is 77 K. ρ_{met} here represents the resistivity of the metallic layers in ReBCO tape, and it is practically the same as the resistivity of the copper stabilizing layer [174]. It is calculated as follow [174],

$$\rho_{met}(T_h) = \rho_{copper}(300K)\left[1 + 0.0039(T_h - 300)\right]$$

Equation 4. 3

The ρ_{copper} is the resistivity of copper. Under AC conditions, the value of ρ_{copper} varies with the transport current in the tape.

The E-J power law during the quenching can then be rewritten as,

$$\begin{cases} J = \dfrac{I_{tot}}{S_c} \\[2ex] J_{su} = \dfrac{I_{su}}{S_c} \\[2ex] J_{met} = \dfrac{I_{met}}{S_c} \\[2ex] E(J) = \dfrac{J - J_{su}}{\sigma_{met}(T_h)} \end{cases}$$

Equation 4. 4

Where J is the total engineering current density of the ReBCO tape, J_{su} is the current density that flows in the superconducting layer, and J_{met} is the current density flowing in the metallic layers. Sc here represents the cross section of the ReBCO tape.

According to the basic principle of superconductivity, the critical current of the superconductor is related to both the temperature and the magnetic field. Their relationship can be expressed using following equations;

$$J_{cT}(T_h) = \begin{cases} \left(\dfrac{T_c - T_h}{T_c - T_o}\right)^{\alpha} & \text{if } T_h < T_c \\[2ex] 0 & \text{if } T_h \geq T_c \end{cases}$$

Equation 4. 5

$$J_{cB}(B,\theta) = J_{cB}(B_{\parallel}, B_{\perp}) = \dfrac{J_{c0}}{\left[1 + \dfrac{\sqrt{(k|B_{\parallel}|)^2 + |B_{\perp}|^2}}{B_0}\right]^{\beta}}$$

Equation 4. 6

In Equation 4.5, J_{cT} here illustrate the dependency of the critical current density on the temperature. The critical temperature of the ReBCO tape T_c is 92 K. The operating temperature T_o is 77 K. α represents the influence of temperature and has a value of 1~2 [163]. In Equation 4.6, J_{cB} is the dependency of the critical current density on the external magnetic field. $B_{\parallel}$ and $B_{\perp}$ represent the parallel and perpendicular components of the magnetic field. Their values are given by the A-formulation module. The shape parameters that characterize the field anisotropy of the ReBCO tape are; k=0.0605, β=0.758, B_0=103 mT. Combined Equation 4.5 and Equation 4.6, we have the dependency of the critical current density on both the magnetic field and temperature;

$$\mathbf{J_c}(\mathbf{B}, T_h) = J_{cT}(T_h) \cdot J_{cB}(B_{\parallel}, B_{\perp})$$

Equation 4. 7

Where I_{c0} = 100 A is the critical current of ReBCO tape at 77 K under self-field situation.
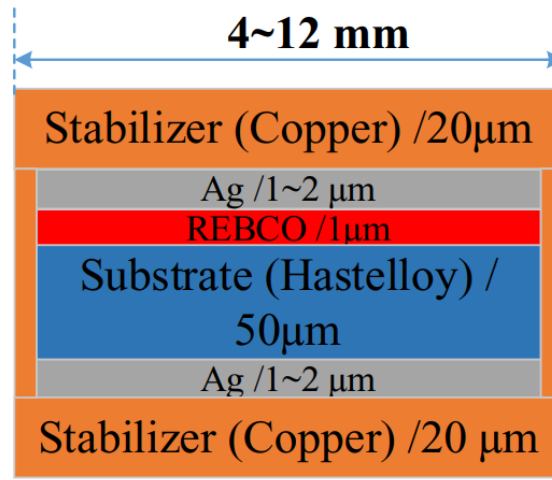
Figure 4. 2 Cross section of the ReBCO tape made in SuperPower [165].
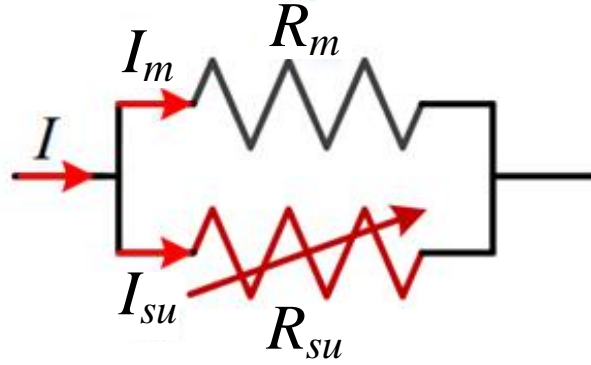
Figure 4. 3 The equivalent circuit for the ReBCO tape [165].

4.2.2   The Multi-physics properties of the model

We coupled four independent modules in COMSOL Multiphysics to build this multi-physics time-dependent 3D quench model; the T-formulation module, the A-formulation module, a heat transfer in thin shell module and an equivalent circuit module. Equations of these four modules are solved simultaneously. Introduction of these four modules are as follow,

Numerical algorithm of the 3D quench model is presented in Figure 4. 4.
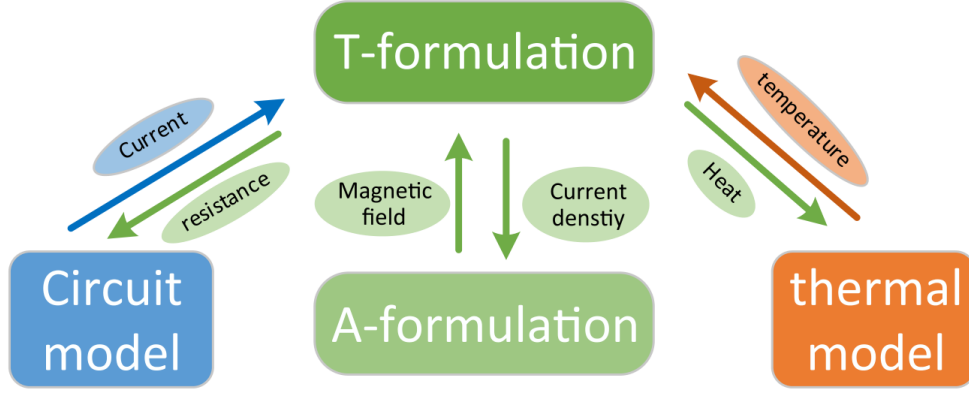
Figure 4. 4 The numerical algorithm of the 3D CORC cable quench model with four modules coupled [165].

a) The T-formulation module

This module only applies to the superconducting layer of the ReBCO tape. It enables the calculation of the current density distribution in the superconducting coated conductor. Based on the aforementioned thin sheet approximation, the thickness of the tape is ignored, which means that there is no current component that is normal to the tape surface. By applying this assumption, the transport current can only flow tangentially to the tape surface. Definition equations of the current vector potential $\mathbf{T}$, as well as the scalar variable T, are listed in Chapter 3, from Equation 3.1 to Equation 3.4. The governing equation of this module can then be derived using the scalar variable T, combined with the Faraday's law and the E-J power law;

$$\nabla \times \mathbf{E}(\mathbf{J}) = \nabla \times \mathbf{E}(\nabla \times (T \cdot \mathbf{n})) = -\frac{\partial \mathbf{B}}{\partial t} \qquad \text{Equation 4. 8}$$

Notice that the magnetic field $\mathbf{B}$ is not solved using the iteration of Equation 4.7. It is not obtained from this T-formulation module, thus is not directly coupled to the scalar variable T. The matrix of magnetic flux density $\mathbf{B}$ is given by the A-formulation module.

The transport current can be imposed on the ReBCO tape by adding a specific boundary condition on every edge of the superconducting layer. Expression of this boundary condition is as follow [146, 147],

$$T_l - T_r = \frac{I_x}{d} \qquad \text{Equation 4. 9}$$

For better understanding, we use a graph, Figure 4. 5, to present the relationship between the T-formulation module and the A-formulation module in the model domain. T_1 and T_r in the equation are the scalars of the current vector potential **T** on the left and right edge of the tape respectively. I_x (x = 1, 2, 3) is the transport current in the n-th ReBCO tape of the CORC cable. Value of I_x will be given by the equivalent circuit module. This will be discussed later in the equivalent circuit module part. d represents the thickness of the ReBCO tape.
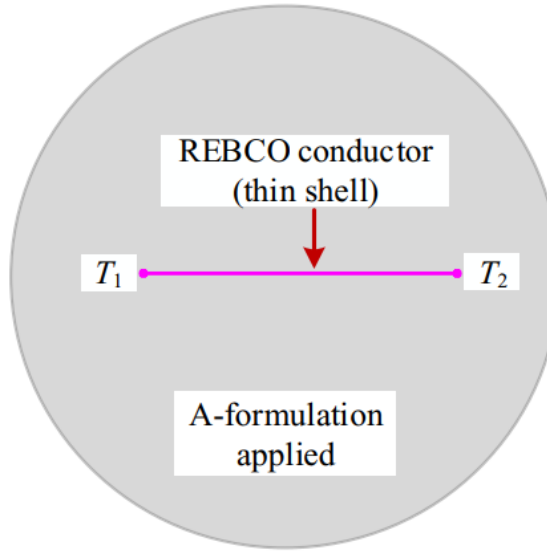
Figure 4. 5 Boundary condition of the T-formulation module and its relationship to the A-formulation module.

b) *The A-formulation module*

This module applies to the whole model domain, including the superconducting layer and the remaining air space. Definition of the magnetic vector potential A is expressed in Equation 3.7, Chapter 3. The boundary condition to impose the surface transport current in this module is defined in Equation 3.8, Chapter 3. This module enables the calculation of the magnetic field distribution in the whole model domain. The matrix of magnetic field **B** calculated using this module will then be returned to the T-formulation module, thus coupling these two modules.

c) *The heat transfer in thin shell module*

The temperature of the ReBCO tapes is obtained by this heat transfer module. The ReBCO coated conductor has an ultra-thin thickness. Compared with the superconducting layer, the metallic layers in the ReBCO conductor have relatively high thermal conductivity. Combined the two factors, it is reasonable to ignore the temperature variation on the vertical direction to the tape surface. Thus, the assumption is made that the ReBCO coated conductor has a uniform temperature distribution on the vertical direction of the conductor surface. In another word, the thin sheet approximation we made in the T-A formulation still applies to the heat transfer model.

The ReBCO coated conductor, as a solid that has uniform temperature distribution on the thickness direction of the conductor, has following governing equation in this heat transfer in thin shell module,

$$\begin{cases} \rho C_p \dfrac{\partial T_h}{\partial t} + \nabla \cdot \mathbf{q} = Q_s + Q_p \\ \mathbf{q} = -k \nabla T_h \end{cases} \qquad \text{Equation 4. 10}$$

ρ is the thermodynamic density and C_p is the heat capacity at a constant pressure of the coated conductor. Q_s represents the Joule heat that is generated by the transport current flowing in the metallic layers. Q_p is the heat pulse that we imposed in the ReBCO coated conductor to cause the local hotspot. k is the equivalent homogenous thermal conductivity of the coated conductor under heat condition.

We consider k and C_p as two parallel thermal resistances. Thus, the following formulations are used to calculate their values,

$$k = \frac{k_1 S_1 + k_2 S_2}{S_1 + S_2} \qquad \text{Equation 4. 11}$$

$$C_p = \frac{C_{p1} m_1 + C_{p2} m_2}{m_1 + m_2} \qquad \text{Equation 4. 12}$$

In Equation 4.11, k_1 and k_2 represent the thermal conductivity of the Hastelloy substrate and Copper stabilizer of ReBCO tape, S_1 and S_2 mean the areas of the cross-section of these metallic layers. Similarly, in Equation 4.12, C_{p1} and m_1 are the thermal capacity

and mass of the Hastelloy substrate, while C_{p2} and m_2 are the thermal capacity and mass of the Copper stabilizer. The COMSOL material library has the thermal parameters of the Copper stabilizer, and we choose the thermal parameters of the Hastelloy substrate based on data in [176]. Values of k and C_p under a range of temperatures are presented in Figure 4. 6.
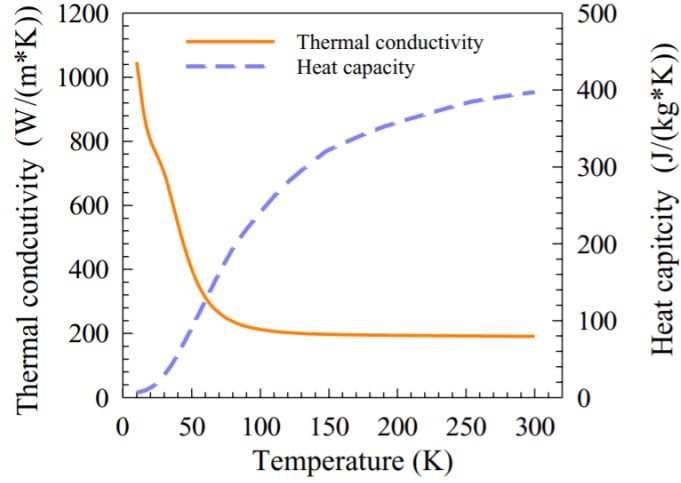
Figure 4. 6 The equivalent heat capacity k and thermal conductivity C_p of the ReBCO coated conductors against temperature.

The gradient (∇) of the temperature T_h includes two components, one is the tangential component (∇_t) and the other one is the normal component (∇_n). Their expressions are as follows,

$$\begin{cases} \nabla_n T_h = (\nabla T_h \cdot \mathbf{n})\mathbf{n} \\ \nabla_t T_h = \nabla T_h - (\nabla T_h \cdot \mathbf{n})\mathbf{n} \end{cases}$$

Equation 4. 13

$\mathbf{n}$ here is the unit vector potential normal to the surface of the coated conductor. Then Equation 4.10 is then revised as follow,

$$\begin{cases} \rho C_p \dfrac{\partial T_h}{\partial t} + \nabla \cdot \mathbf{q} = Q_s + Q_p \\ \mathbf{q} = -k\nabla_n \cdot (\nabla_n T_h) - k\nabla_t \cdot (\nabla_t T_h) \end{cases}$$

Equation 4. 14

Since the thin sheet approximation is applied to this module, we can ignore the normal component of ∇T_h and only consider the tangential component of the coated conductor.

The final governing equation for a superconducting coated conductor in a heat transfer module is thus as follow,

$$\begin{cases} \rho C_p \dfrac{\partial T_h}{\partial t} + \nabla \cdot \mathbf{q} = \dfrac{Q_s + Q_p}{d} \\ \mathbf{q} = -k \nabla_t \cdot \left(\nabla_t T_h \right) \end{cases}$$

Equation 4. 15

where d is thickness of the ReBCO coated conductor.

Considering the continuity and insulation, a boundary condition for cooling is applied to the ReBCO tape surface with expression as follow,

$$\begin{cases} -\mathbf{n} \cdot \mathbf{q} = h(T_h - T_a) \\ q = -k \nabla_t \cdot (\nabla_t T_h) \end{cases}$$

Equation 4. 16

Here, T_a is the ambient temperature; h is the heat transfer coefficient. The time constant of a thermal system is always dramatically longer than the duration of a quench in ReBCO coated conductors. Thus, we applied an adiabatic boundary condition to the ReBCO tapes in this quenching study, which means $h = 0$.

d) *Equivalent circuit module*

An equivalent circuit module is used to represent the single-layer CORC cable when a quench happens. It is coupled to the other three modules for the calculation of the current redistribution among three ReBCO tapes. The equivalent circuit used in this module is presented in Figure 4. 7. Each ReBCO tape in the cable is divided into three separate components. R_{tx} (x=1, 2, 3) is the terminal contact resistance (TCR), which is also called 'terminal soldering resistance'; $R_{tape,x}$ (x=1, 2, 3) is the total resistance of the x-th tape; and an inductance. According to experiments in previous research work [164], value of the TRC varies from 0.1 $\mu\Omega$ to 200 $\mu\Omega$. The governing equation for this equivalent circuit module is,

$$\begin{cases} U_x = I_x(R_{t,x} + R_{tape,x}) + \sum_{n=1}^{3} \frac{dI_n}{dt} M_{x,n} \quad (x=1, 2, 3) \\ U_1 = U_2 = U_3 \\ I_{op} = I_1 + I_2 + I_3 \\ R_{tape,x} = \frac{R_{su,x} \cdot R_{met,x}}{R_{su,x} + R_{met,x}} \end{cases}$$

Equation 4. 17

Here U_x and I_x are the voltage and current of the x-th ReBCO tape in the CORC cable. Vaule of I_x calculated using this equivalent circuit module will then returned to the T-formulation module, coupling these two modules. I_{op} is the total operating current inside the cable. $R_{su,x}$ here is the resistance of the superconducting layer, while $R_{met,x}$ is the resistance of the metallic layers. $R_{su,x}$ is obtained using the E-J power law formulation, and $R_{met,x}$ is calculated using Equation 4.3. $M_{x,n}$ represents the mutual inductance between the x-th ReBCO tape and the n-th tape. When $x = n$, it also represents the self-inductance. The three ReBCO tapes used are identical, and the CORC cable has a symmetric structure. Thus, the sum of self- and mutual-inductance of each tape is the same. This means three ReBCO tapes share the same inductive voltage during the operation process.

The resistance of the tape itself (R_{tape}) and the terminal contact resistance R_t play important roles in the current redistribution among three ReBCO tapes during quenching. The voltage of the terminal contact is different from the total tape voltage, and is named as 'contact voltage'. Several experiments have shown that when a local quench happens, no current will be redistributed and flow into the pressed contact joints, as the resistance of the pressed joints is too high, compared with the soldered terminal contact resistance. In the real situation where a CORC cable is always constructed with hundreds of ReBCO tapes, when a local quench occurs and one of these tapes starts to redistribute current, the redistributed current will be completely absorbed by other tapes. Normally, the operating current is below the critical value or sometimes goes a bit over. Thus, for a local hotspot-induced quench, no current will be redistributed through the pressed contact joints into the metallic core of the CORC cable. For this reason, we do

not consider the influence of the metallic cores on the current redistribution during a quench.
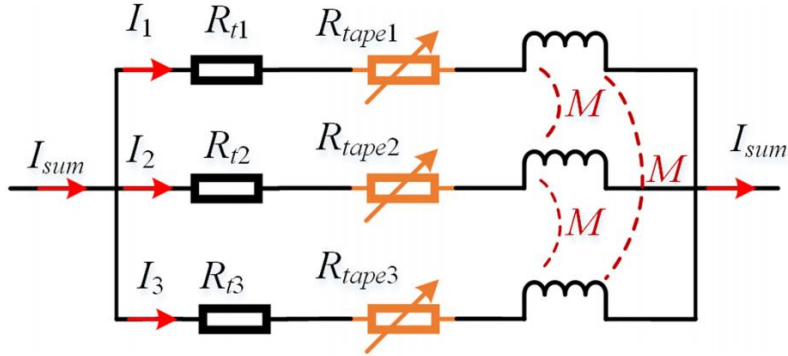
Figure 4. 7 The equivalent circuit for the single-layer CORC cable wound by 3 ReBCO tapes [165].

4.3 Influence of uniform terminal contact resistance

4.3.1   A hotspot-induced quench

To start with, a series of simulations was conducted with different terminal contact resistances and various heat pulses imposed on Tape 1. For a simple variable study, we started with the assumption that the terminal contact resistances (TCRs) of three ReBCO tapes are uniform, which means, for a single-layer CORC cable that is constructed using three ReBCO tapes, each tape has the same value of TCR. As mentioned before, no cooling power is considered here. First step of the simulation is to give the CORC cable a flowing current. A transport current of 120 A is imposed on each ReBCO tape to ramp the total transport current in the CORC cable to 360 A. This ramping process takes 1.2 seconds. The second step is to impose an external heat pulse on Tape 1. This extra heat source is added to the model using the heat transfer module. Duration of this heat pulse is 100 milliseconds. During this period, the heating power is considered to be constant. Notice that for simplicity, any heat generated in the TCRs is ignored in this part of the analyses.

The temperature on the hotspot under different TCRs (R_t) with a heat pulse of 183 mJ imposed on Tape 1 was presented in Figure 4. 8. In the duration of imposing the heat pulse, the temperature of the hotspot dramatically increases. A peak value of around 100 K is achieved at t=100 ms, which is the end of the heat pulse. This heat pulse then induced a normal zone, which

then further propagated to surrounding areas. From this graph, when the value of TCR is lower than 20 μΩ, after the heat pulse is turned off, the temperature of the hotspot gradually falls to an acceptable range, lower than 85 K here. Thus, the normal zone finally recovers from quenching and returns to the superconducting state. However, if the value of TCR goes beyond a certain range, i.e. $R_t \geq 50$ μΩ, then there will be no recovery on the ReBCO tape. After a slight temperature decrease with the heat pulse turning off, the temperature of hotspot keeps increasing, eventually causing quench on the tape.
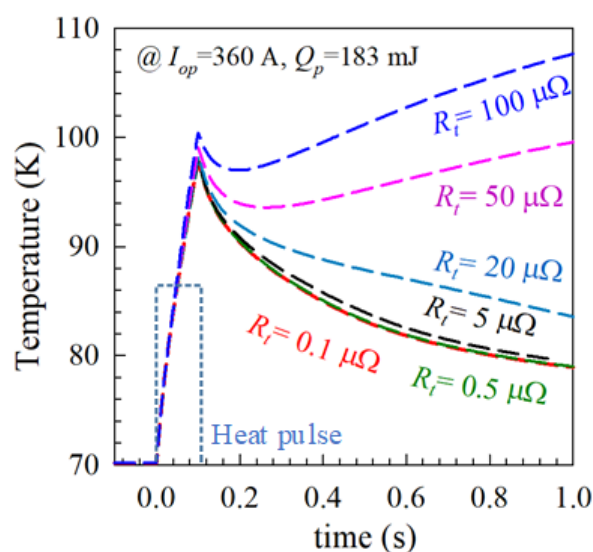
Figure 4. 8 Temperature (K) of the hotspot with a heat pulse of 183 mJ imposed on Tape 1.

TCRs = 0.1μΩ - 100μΩ.

Change of the current and voltage of each tape is plotted in Figure 4. 9. The voltage here only represents the voltage on the ReBCO tape, the TCR is not included here. The whole process of the hotspot-induced quench has two obvious stages; the first stage, Stage I, is when the heat pulse is imposed on Tape 1, i.e. $t = 0 \sim 100$ ms. Stage II is the time duration when the heat pulse is turned off, i.e. $t > 100$ ms.

For Stage I, the current in Tape 1 drops sharply, for the applied heat pulse causing immediate temperature rise on the tape. The current that is forced out from Tape 1 is redistributed and absorbed by the other two tapes; this explains the current rise on Tape 2&3. There are two main factors affects the redistribution of the current; the terminal contact resistance TCR and the critical current I_c of ReBCO tape.

In cases when R_t = 0.1 or 5 μΩ, during t = 0~28 ms, the current in Tape 2&3 is below 148 A, the tape's operating under the superconducting state with almost zero resistance. Even a slight voltage rise causes a considerable current redistribution among tapes. After 28 ms, an overcurrent exists on both Tape 2&3, the tape voltage increases dramatically. This sharp voltage rise effectively prevents further current redistribution from Tape 1 into other tapes, slowing down the decrease of current in Tape 1. At the point when the heat pulse is turned off, i.e. t =100 ms, the temperature on the hotspot reaches around 100 K, generating a certain range of normal zone on the surface of Tape 1. At this point, the current in Tape 1 is 40 A, while an overcurrent of 160 A still flows in Tape 2 & 3. The voltage of Tape 1 is almost the same as the other tapes when R_t = 0.1 μΩ. The normal zone in Tape 1 and the overcurrent in the other two tapes together cause the voltage to rise to 6 mV. Thus, the contact voltage (the voltage of the terminal contact resistance) of Tape 1 is 4 μV, while the contact voltage of the other two tapes both reaches 16 μV. The voltage of TCRs is quite small compared with the tape voltage itself. With the increase of TCRs, the contact voltage will take more proportion compared with the tape voltage. When R_t reaches 5 μΩ, the voltage on Tape 1 shows an obvious difference with the voltage of the other tapes, which also means that with the increase of TCR, i.e. larger than 5 μΩ, its influence on the current redistribution is more obvious. When the TCR reaches 20 μΩ, this difference between the voltage of Tape 1 and the other two tapes are even larger. With R_t=100 μΩ, the contact voltage of Tape 1 at t =100 ms is 6 mV, while the tape voltage is 12 mV. The contact voltage of Tape 2 & 3 is around 14.8 mV. The lowest current of Tape 1 only decreases to around 60 A when the heat pulse is turned off. The high terminal contact resistance obviously prevents the current redistribution among tapes, thus leading to higher tape voltage and higher temperature on the hotspot. Thus, the conclusion is that the higher TCRs may eventually cause a higher risk of quenching.

After 100 ms, the quenching process enters stage II. When TCR of this CORC cable is lower than 20 μΩ, current and voltage of each tape gradually return to their initial values, as the heat generated will be extracted by the cooling systems of the cable. Figure 4. 10 presents the normal zone propagation for the duration of 1000 ms. From Figure 4. 10 (a), the size of the normal zone grows smaller follows the disappear of the heat pulse, finally disappears as well. The cable eventually recovers from the quench. However, when TCR is high enough, in this case larger than

100 μΩ, the tape voltage increases rapidly as the normal zone propagates along the tape, which certainly induces an unrecoverable quench on Tape 1, as can be seen in Figure 4. 10 (b). This enlarging quench area may eventually damage the whole tape. The current in Tape 1 continuously flows out through the TCR and be redistributed into other two tapes, causing overcurrent in Tape 2 & 3. This also raises the possibility to induce another quench on these two tapes.
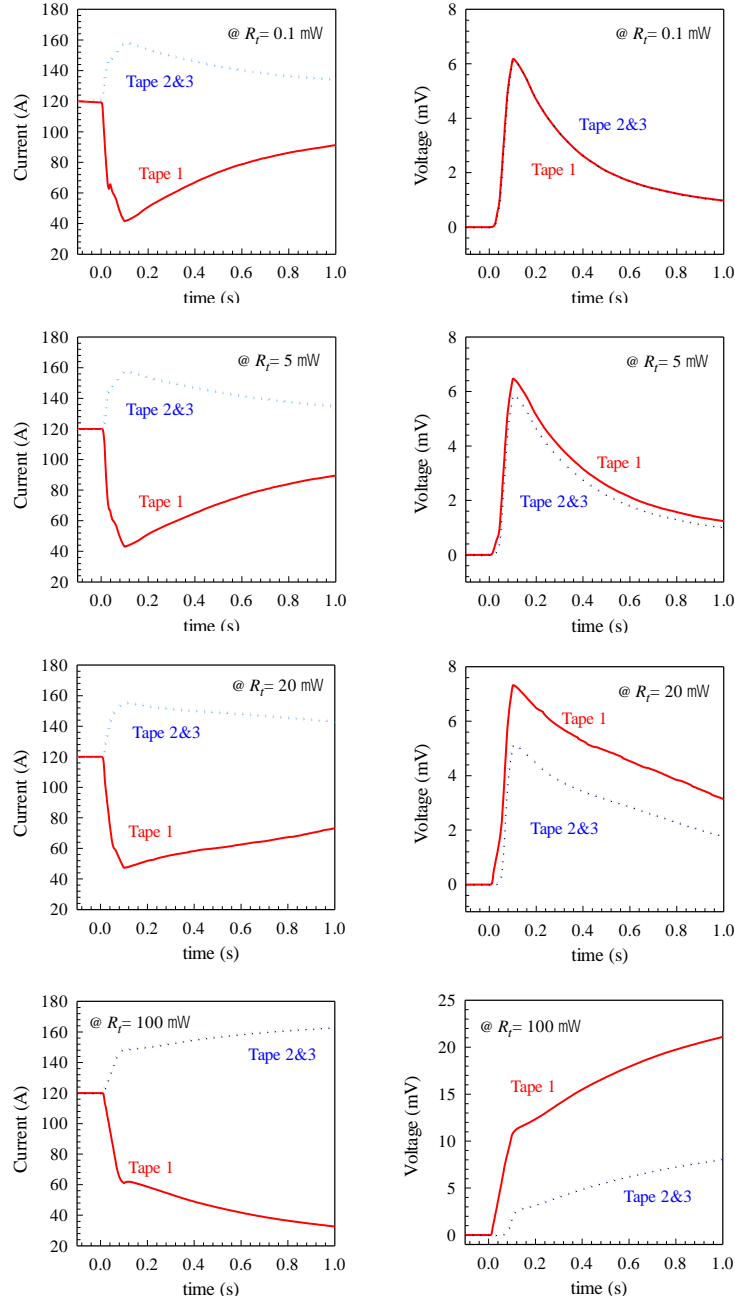
Figure 4. 9 Change of current and voltage of each ReBCO tape under various TCRs. A heat pulse of 183 mJ is applied to Tape 1. The other two tapes with no hotspot are called 'Tape2' and 'Tape3' respectively.

t=28 ms (Stage I)

t=28 ms (Stage I)

t=100 ms (Stage II)

t=100 ms (Stage II)

t=500 ms (Stage II)

t=500 ms (Stage II)

t=1000 ms (Stage II)

t=1000 ms (Stage II)

(a) R_t = 0.1 μΩ

(b) R_t = 100 μΩ

70   75   80   85   90
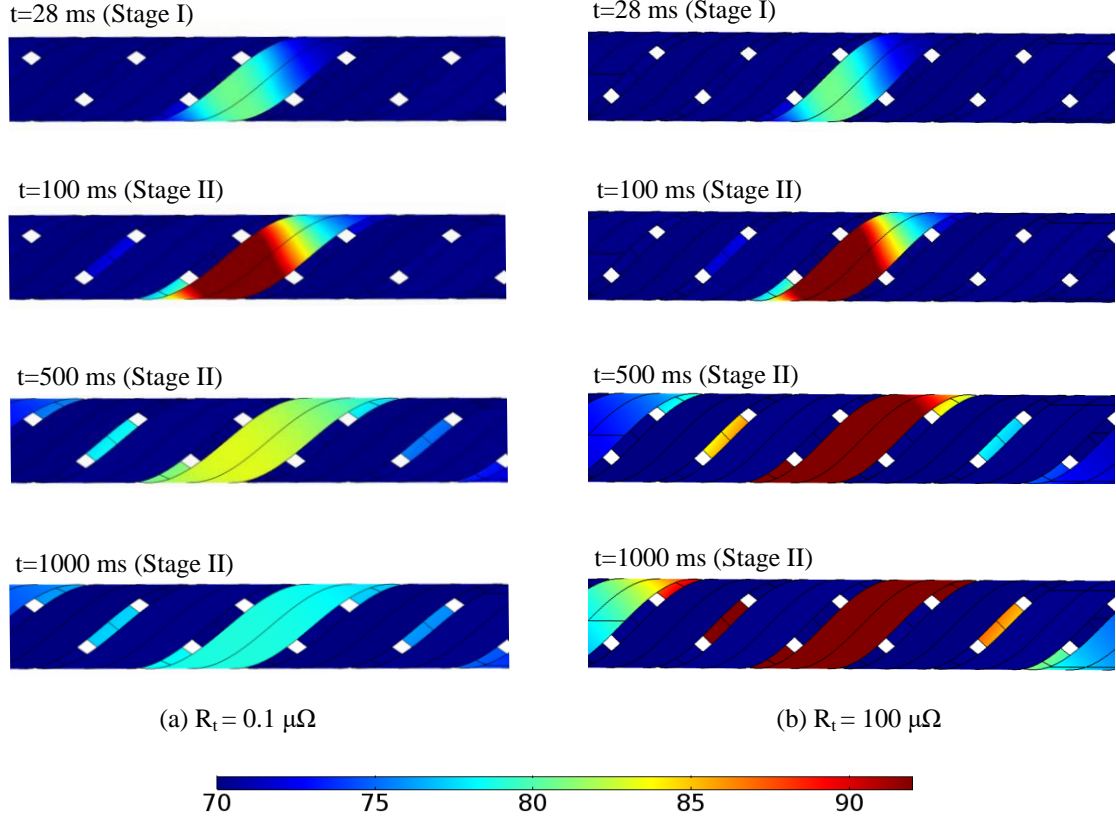
Figure 4. 10 Normal zone propagation on Tape 1 with a heat pulse of 183 mJ. The terminal contact resistance is (a) R_t = 0.1 μΩ; (b) R_t =100 μΩ.

4.3.2   Minimum quench energy (MQE)

The stability of a superconductor can be defined in terms of the 'minimum quench energy' (MQE). It is the lowest value of a heat pulse that is sufficient enough to cause a quench on the superconductor. The minimum quench energy was calculated under various terminal contact resistances. The result is plotted in Figure 4. 11. Dependence of MQE on TCRs can be divided into three stages. When R_t is low enough, i.e. lower than 5 μΩ, the MQE decreases slowly and gradually with the increase of TCRs. The second stage is when 5 μΩ $\leq R_t \leq$ 100 μΩ. During this stage, a rapid decrease of MQE occurs when there is a slight increase of TCR. Then the MQE is down to a minimum value. The third stage is when Rt is larger than 100 μΩ, in which the MQE shows no further reduction even the TCR still increases.

104
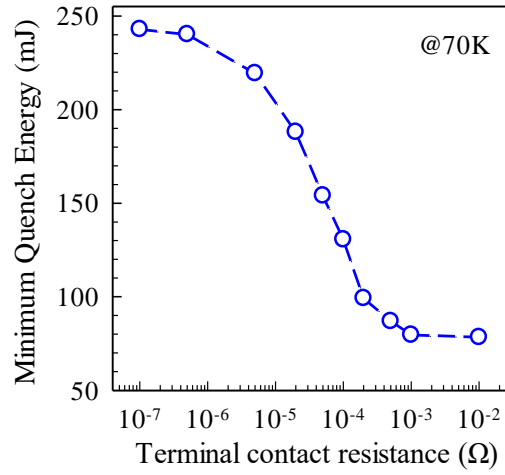
Figure 4. 11 The dependence of MQE on TCRs.

Three typical values of TCRs are chosen to present the variation of current and temperature of each tape during the quenching process. The same heat pulse energy of 243 mJ is applied to each case. In Figure 4. 12 (a) and (b), the current redistribution and temperature on the hotspot are nearly identical in two cases. This also proves that with terminal contact resistance that is low enough, the performance of quench is much less affected by the value of TCRs. A different situation occurs when R_t = 500 μΩ. Under this level of terminal contact resistance, it is nearly impossible for the current to flow out from Tape 1 through TCR, thus the current redistribution among tapes is weak. From Figure 4. 12 (c_1), the percentage of the current redistributed to the other two tapes only reaches around 9% at t = 100 ms. When R_t = 500 μΩ, the MQE is 87 mJ. We also calculated the MQE when the terminal contact resistance is infinite, which presents the single ReBCO tape situation. The MQE is 78 mJ, which shows no obvious increase compared with the 500μΩ case. This indicates that although the CORC cable is constructed by many parallel-wound ReBCO tape, when the TCR is too large, i.e. larger than 500 μΩ, the thermal behaviour of the cable is no better than the single tape situation.

Also, From Figure 4. 12, though low TCR results in strong current redistribution among tapes, which helps to prevent inducing quench, it also leads to overcurrent on the other two tapes. This overcurrent may cause heat accumulation, leading to a dramatic rise of temperature on Tape 2&3. This results in overcurrent quench on Tape 2&3. However, the temperature rise also causes an increase in tape resistances of Tape 2&3. Once the resistances of Tape 2&3 are

higher, the redistributed current is forced to flow back to Tape 1. In Figure 4. 12(a) and (b), after 3 seconds, the current of Tape 1 shows a dramatic increase while the temperature is still high. Thus, all three ReBCO tapes are eventually quenched. On the other hand, with high terminal contact resistance, the hotspot-induced current redistribution and temperature rise have little influence on the other two tapes. The current is hard to be redistributed to Tape 2&3, thus a slight current rise will not induce overcurrent quench on these tapes. Notice that, although a slight over current operation is induced on Tape 2 & 3, which causes a very small heat production on those two tapes, the temperature of Tape 2&3, as can be seen in Figure 4. 12(c_2), does not rise. Reason for this is that the quenching happens too fast (within 0.5-1 seconds) on the tape with hotspot, and the temperature rise on normal tapes is too tiny to be observed. Meanwhile, the temperature of Tape 1 increases dramatically. This indicates that under high TCRs, the quench happens fast but only damages the tape with hotspot. Rest of the tapes will not be affected by this hotspot.
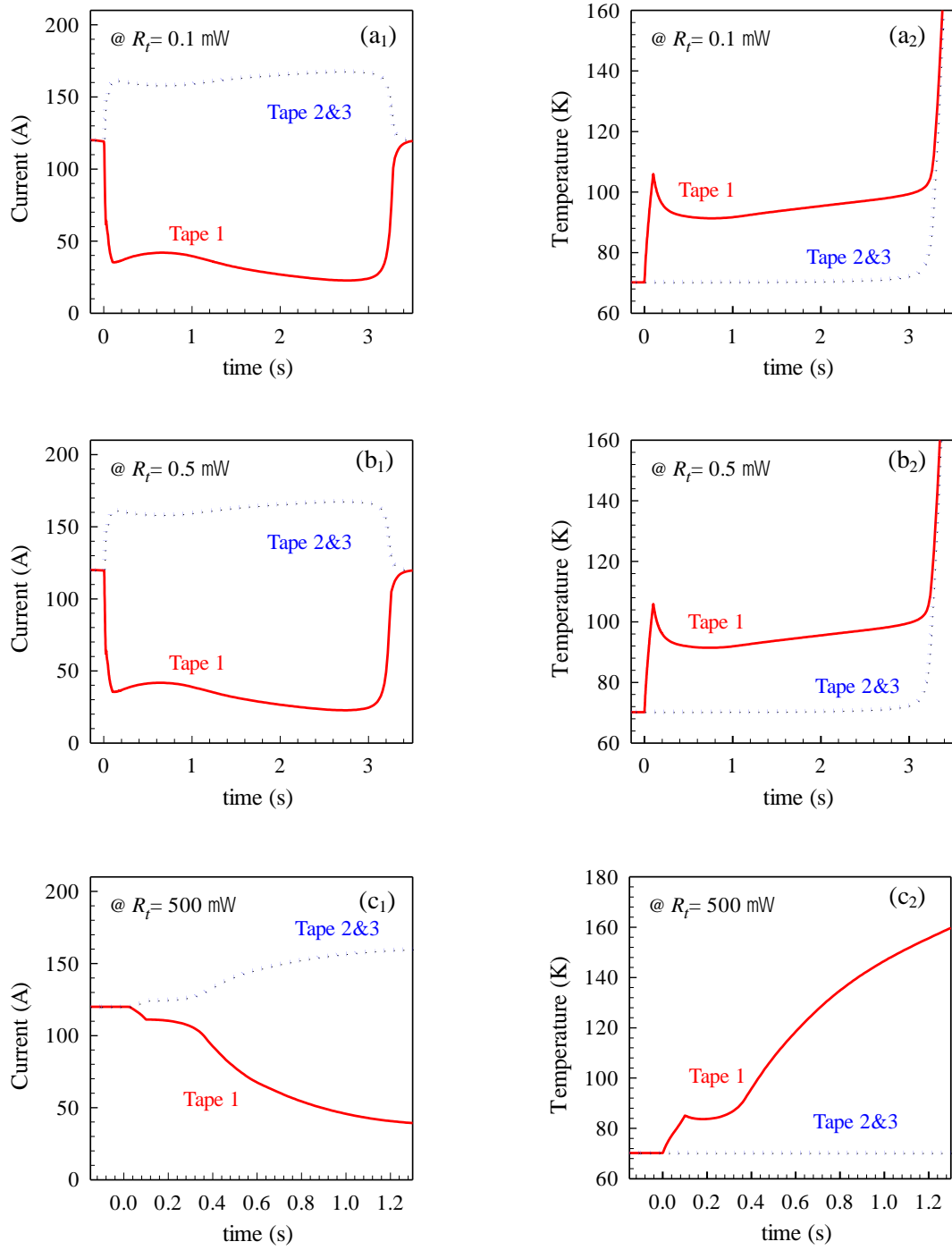
Figure 4. 12 The current and temperature of each tape during a hotspot-induced quench operation under various terminal contact resistance R_t. (a) $R_t = 0.1\ \mu\Omega$; (b) $R_t = 0.5\ \mu\Omega$; and (c) $R_t = 500\ \mu\Omega$. The heat pulse energy Q_p is 243 mJ.

The factors that might cause quench in all ReBCO tapes were then discussed. We chose the case when $R_t = 0.5\ \mu\Omega$, $Q_p = 243$ mJ, and $I_{op} = 120$ A in each tape. A hotspot-induced quench

occurs on Tape 1 and overcurrent quenches occur on Tape 2&3. The applied current I_{op} was then reduced to 100 A and increase the heat pulse energy to 261 mJ. The current variation and temperature rise in each tape are presented in Figure 4. 13. The current of Tape 1 is decreased to almost zero, while current of the other two tapes is still lower than its critical current. It clearly shows that, even with a higher heat pulse imposed on Tape 1, the lower transport current effectively prevents the other two tapes from overcurrent quenches. It also eliminates the hotspot-induced quench on Tape 1. This proves that the transport current plays an important role in the thermal stability of CORC cable. Thus, with low TCRs, when the transport current is relatively high, a local hotspot-induced quench on one tape may cause overcurrent quench on other tapes. A proper value of transport current is of vital importance to prevent quench.
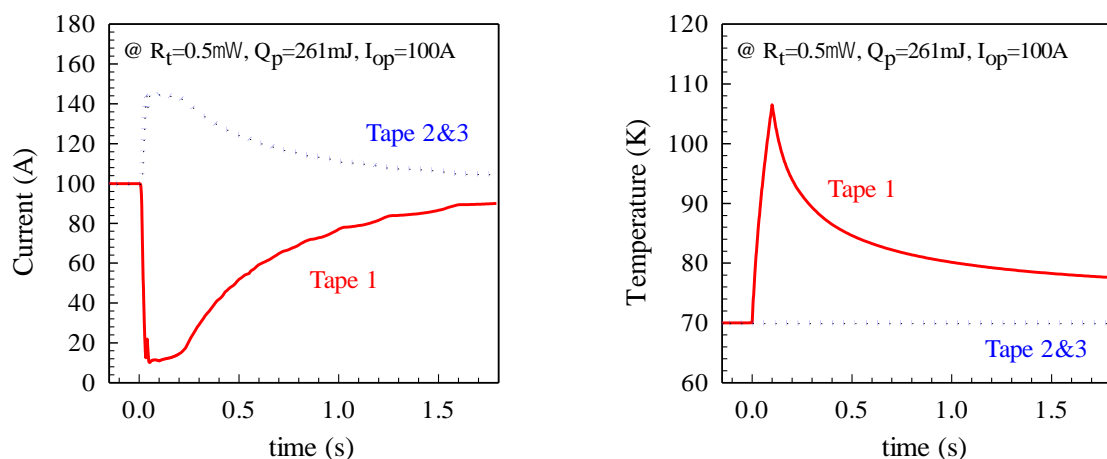
Figure 4. 13 Variation of current and temperature of each tape during a hotspot-induced quench. The terminal contact resistance is 0.5 μΩ, the heat pulse added on Tape 1 is 261 mJ, and the applied transport current I_{op} is 100 A.

4.4 Influence of non-uniform terminal contact resistance

In practical applications, it is nearly impossible for CORC cable to have totally uniform terminal contact resistances for each tape. The terminal contact resistance of each tape will, after all, differs from other tapes. Thus, we also need to analyse the influence of non-uniform terminal contact resistance on the quench behaviour of CORC cable, for it is closer to the realistic situations. Structure and the physical properties of the CORC cable studied in this

section is the same as Section 4.2.3. The operating temperature is still set to be 70 K, under which the I_c of the tape is 148 A. All model assumptions remain the same. A transport current of 120 A is applied to each tape to ramp the total flowing current of the CORC cable to 360 A. Different from the last section, since the terminal contact resistance is no longer uniform, the transport current of each tape is unevenly distributed. Ramping of the current takes 2 seconds. Then a heat pulse is still imposed on the 'Target tape', Tape 1, for 100 milliseconds. Tape 2&3 are labelled as 'normal tape' in this section. The values of the terminal contact resistances are 40 μΩ, 50 μΩ and 60 μΩ. The heat pulse was applied on each one of the tapes respectively to analyse these three different cases of the hotspot-induced quench. Three different cases were analysed: to impose a heat pulse on tape with $R_t = 40$ μΩ, to impose a heat pulse on tape with $R_t = 50$ μΩ, and to impose a heat pulse on tape with $R_t = 60$ μΩ. For convenience, the case when the heat pulse is applied to tape with $R_t = 40$ μΩ is called as 'Case 1', heat pulse imposed on tape with $R_t = 50$ μΩ is 'Case 2', and the one on $R_t = 60$ μΩ is 'Case 3'.

4.4.1 Case 1: Heat pulse imposed on tape with R$_t$=40 μΩ

In Case 1, various heat pulses are imposed on the target tape with $R_t = 40$ μΩ. The simulation results are extracted when the heat pulse energy is just about enough to cause a hotspot-induced quench on the target tape. The heat pulse energy that causes irreversible quench on CORC cable is 104.4 mJ. The current variation among tapes, the change of tape voltage, and the temperature rise on the target tape are shown in Figure 4. 14. Note that in all figures, the red line always represents the target tape (with hotspot induced), while the blue and black lines are values in two normal tapes (without hotspot induced). From Figure 4. 14(a₁), in Stage I, though the target tape has the highest transport current at the beginning, it rapidly drops to lower than 80 A after the heat pulse is turned off, while the other two tapes get the redistributed current and rise to 130 A and 150 A respectively. Around 43% of the transport current is redistributed to the other two tapes. At the same time, the voltage of the target tape increases to around 5 mV. The normal tape with an overcurrent of 150 A (I_c=148 A) shows a slight rise of tape voltage, while the voltage of the normal tape with higher R_t does not change with the heat pulse imposed. In Stage II, after a slight decrease in temperature on the target tape, it remains steady for a while, before suddenly increasing dramatically to

over 100 K after 3 seconds of operation. The rise of temperature forces more current out of the target tape and redistributes into normal tapes, leading to overcurrent quenches in both two normal tapes.

Figure 4. 14 Case 1: Variation of current, tape voltage and temperature of each tape during a hotspot-induced quench under terminal contact resistance of 40 μΩ.

4.4.2 Case 2: Heat pulse imposed on tape with R_t=50 μΩ

The quenching process of Case 2 is much smoother compared with the other two cases. In Stage I, obvious current redistribution as well as tape voltage rise is observed in three tapes immediately after the heat pulse is turned off. There is almost 50% of transport current being redistributed from the target tape to two normal tapes, causing overcurrent on both tapes. Though the percentage of current redistribution is quite high, the overcurrent on normal tapes still cause voltage rise, which prevents the current from further redistribution. In Stage II, after the heat pulse is pulled off, the transport current in the target tape keeps the trend to gradually decrease, eventually drops to less than 40 A at 3 seconds. Meanwhile, the transport current in normal tapes keeps rising to a value that is close to 160 A. After a slight decrease, the tape voltage of three tapes gradually increases. At 3 seconds, voltage of the target tape rises to 12.5 mV, while the other two tape voltages are 7 and 5 mV respectively. Similarly, the temperature of hotspot decreases a little before rising to over 100 K and quenching the target tape. During the whole quenching process, no sudden change occurs. Notice that when the hotspot is added on the tape with a moderate value of terminal contact resistance, it takes heat energy of 156.7 mJ to quench the target tape, which is much higher than Case 1.
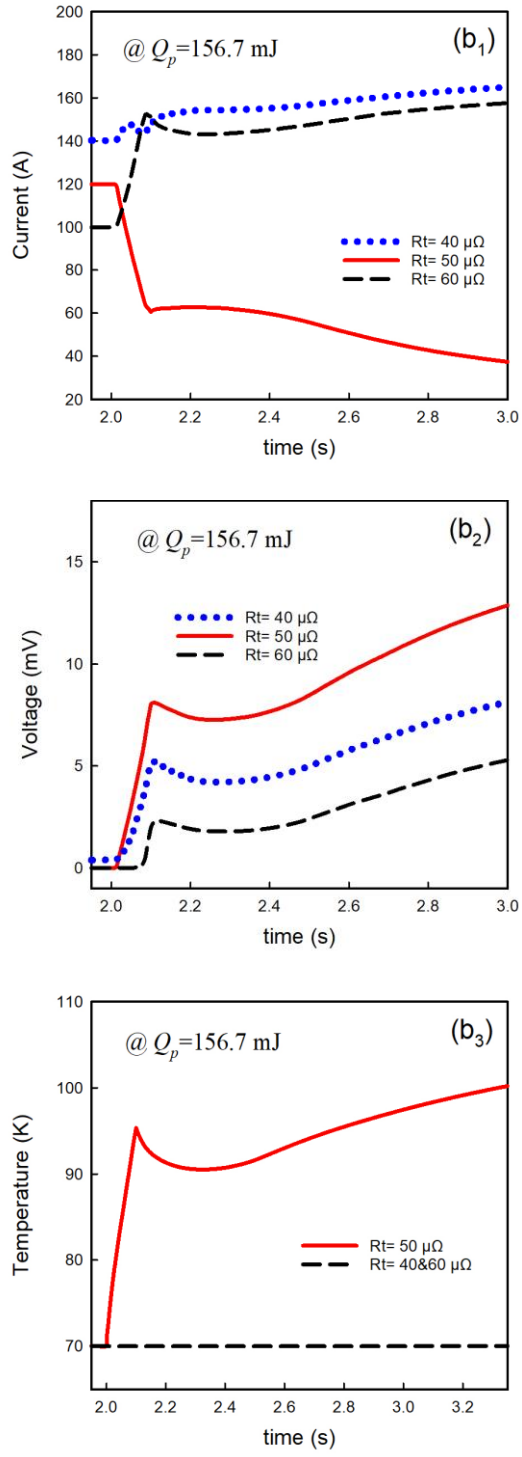
Figure 4. 15 Case 2: Variation of current, tape voltage and temperature of each tape during a hotspot-induced quench under terminal contact resistance of 50 μΩ.

4.4.3   Case 3: Heat pulse imposed on tape with R_t=60 μΩ

In this case, the current in the target tape only decreases to around 60 A during Stage I. This is because the TCR of the target tape is too high, which makes the current redistribution hard. There's also a sharp increase in the voltage of each tape during the heating duration. When the heat pulse is turned off, the temperature of the target tape rises to around 96 K. Then the quenching process of the CORC cable enters a steady-state for around 0.4 seconds, at which duration there is no obvious variation in current, voltage or temperature. After 2.4 seconds, the current is further redistributed to other tapes, causing more voltage rise on these two normal tapes. During the relatively steady state, the temperature of the hotspot decreases slightly to 90 K at 2.4 s, before rising to above 100 K. The voltage of the target tape reaches 13 mV in this case. The heat pulse energy that is required to quench the CORC cable, in this case, is not the highest one. The minimum quench energy is 122.7 mJ, which is higher than Case 1 but lower than Case 2.

Table 4. 2 presents the MQE in all three cases. In Case 1, the MQE is the lowest among all cases, for the tape has the lowest terminal contact resistance. This means that for CORC cable with non-uniform TCR, a hotspot on the tape with lowest TCR is most likely to induce a quench. Surprisingly, when heat energy was added on the tape with the highest R_t (60 μΩ), i.e. Case 3, the MQE is not the highest among all cases. The MQE is 122.7 mJ, which is the middle value among three MQEs. The highest MQE, 156.7 mJ in this case, occurs in Case 2. This result indicates that the MQE of tapes in a single-layer CORC cable depends on two main factors, the transport current flowing in the tape and the current redistribution among tapes through terminal contact resistance. High terminal contact resistance is, of course, not preferred, for it means hard current redistribution among tapes, which leads to a rapid tape voltage increase. It considerably reduces the thermal stability of the cable. However, low TCR also rises problem on thermal stability. A lower terminal contact resistance makes the current redistribution among tapes much easier. This can effectively increase the MQE. But, during the current ramping process, lower TCR also means higher transport current will be imposed on that tape. According to the aforementioned analysis, the tape with a higher transport current always has a lower value

of MQE. Combining these two factors together, the reason why Case 2 has the highest MQE is explained.

This section proves that for a single-layer CORC cable with non-uniform terminal contact resistance, the hotspot-induced quench is most unlikely to occur on the tape with moderate value of TCR. This tape will also have the best thermal stability among all tapes of the cable. The tape with the lowest TCR, on the other hand, has the worst thermal stability, for its MQE is the lowest among three tapes.

Table 4. 2 Minimum quench energies

Terminal Contact Resistance (μΩ)	Minimum Quench Energy (mJ)
40	104.4
50	156.7
60	122.7

This table gives the MQE of the CORC cable when a hotspot is induced on ReBCO tapes with terminal contact resistance of 40 μΩ, 50 μΩ and 60 μΩ respectively.
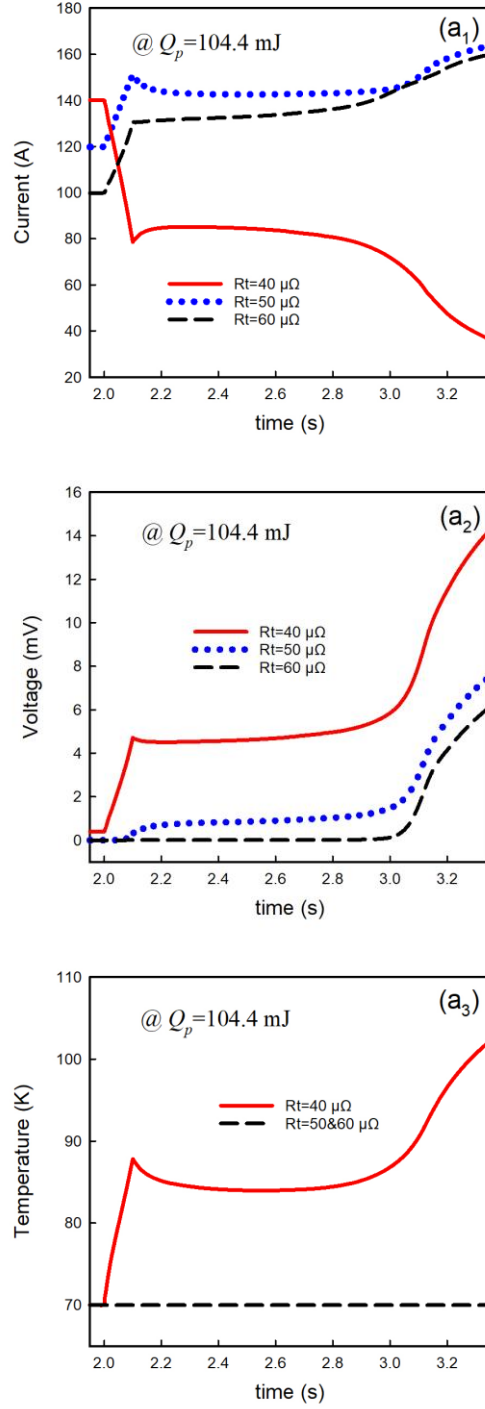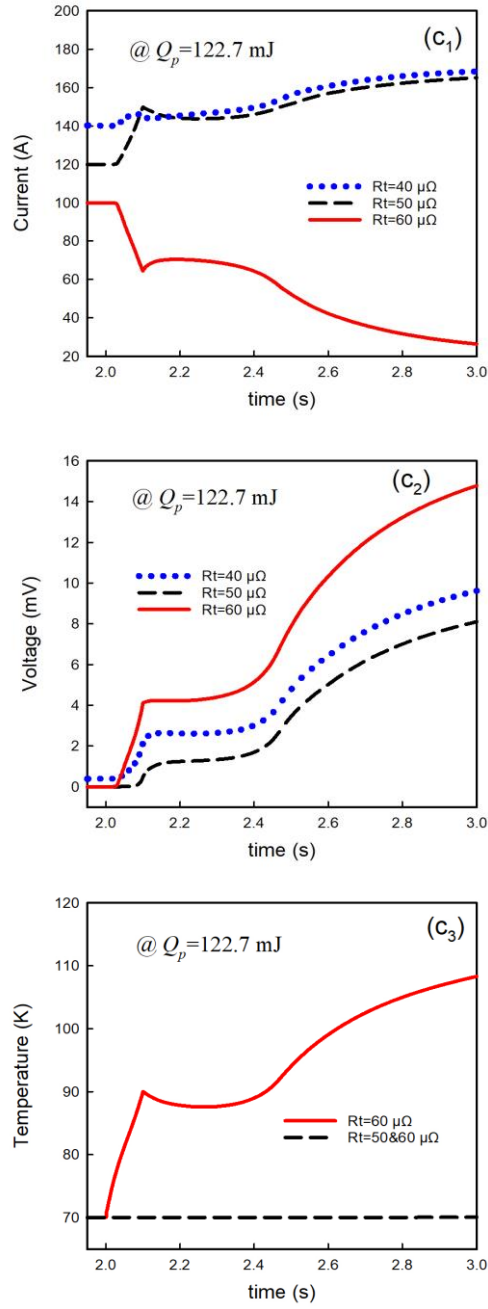
Figure 4. 16 Case 3: Variation of current, tape voltage and temperature of each tape during a hotspot-induced quench under terminal contact resistance of 60 μΩ.

4.5 Summary

This chapter thoroughly studied the quench behaviour of multi-layer CORC cables. A 3D T-A quench model was proposed for the analysis of quenching in CORC cables. Four different modules, the T-formulation module, the A-formulation module, the heat transfer in thin shell

module and the equivalent circuit module, were coupled together to form this quench model. Multi-physics properties of this quench model were introduced in details. To start with, the terminal contact resistance of each tape in the CORC cable was assumed to be ideally identical. The influence of uniform terminal contact resistance was studied by imposing an external heat pulse on one of the tapes in the cable to induce a hotspot-induced quench. The current redistribution among tapes, variation of voltage and temperature, and the normal zone propagation on the target tape during quench process were analysed and discussed. The MQE under various uniform TCRs was calculated to show the dependence of MQE on TCRs. Then, as each tape in the cable will practically have different TCRs, the influence of non-uniform TCRs on the quench behaviour of the cable was studied. Results clearly showed that the tape with moderate value of TCR had the highest MQE, which made it the most stable tape among all tapes in the cable. The tape with the lowest TCR, on the other hand, had the lowest MQE, which means that this tape has the worst thermal stability.

Chapter 5. An HTS tri-axial CORC cable for hybrid-electric aircraft

5.1 Development of next generation of aircraft

Research has reported that the use of air transport releases particulates that is 4.5 times more than those released by cargo shipment, while the emission of nitrous oxides is even 25 times higher [177]. According to *National Geographic*, in 2013, aircrafts released around seven hundred million metric tons of carbon dioxide (CO_2) into the air. This amount of gas emissions is predicted to triple by the end of the year of 2050. On October 2016, 23 countries signed together the first-ever global market-based measure (GMBM) to control gas emissions from international air transport [178]. The global growth in commercial aviation pushes the urgent need for reduction in fuel consumption as well as in carbon emission. To achieve this goal, the next generation of aircraft with lower gas emissions and higher efficiency is an urgent call.

A particular developing component for the next generation commercial aviation fleet is the propulsion system. Revolutionary new technologies are needed to design an electrical propulsion system with lower noise, reduced fuel consumption and high reliability. Three electric propulsion architectures are proposed:

- All-electric (or more-electric) aircraft

- Turboelectric aircraft

- Hybrid-electric aircraft

As shown in Figure 5. 1, the only source of propulsion on an all-electric aircraft is batteries. On the other hand, the hybrid-electric system uses gas turbines as engines to charge batteries as well as for propulsion. The charged batteries are another propulsion for the flight. There are currently three hybrid-electric propulsion systems, the series-hybrid, the parallel-hybrid and the combination of these two [179]. A motor that is powered by batteries and a turbine engine is used to drive a fan, thus providing propulsion for a parallel-hybrid system. For a series hybrid aircraft, the electric motors are connected to the fans while the gas turbine drives an electrical generator. The output of the generator is used to drive the motors as well as charge the batteries.

The series hybrid system can be applied to a distributed propulsion system that uses multiple motors and fans. In the series/parallel partial-hybrid system, the gas turbine drives multiple fans while electrical motors are in charge of the other fans. A battery or a turbine-driven generator is used to power these electrical motors. Turboelectric configuration is classified into two categories, full- and partial-turboelectric. They both use gas turbines instead of batteries to drive electric generators. The only difference between these two concepts is that power of the partial-turboelectric system is partly provided by electric propulsion and partially generated by a turbine-driven turbofan. This means that the technology development required by the partial-turboelectric system is easier than that required by a full-turboelectric system.
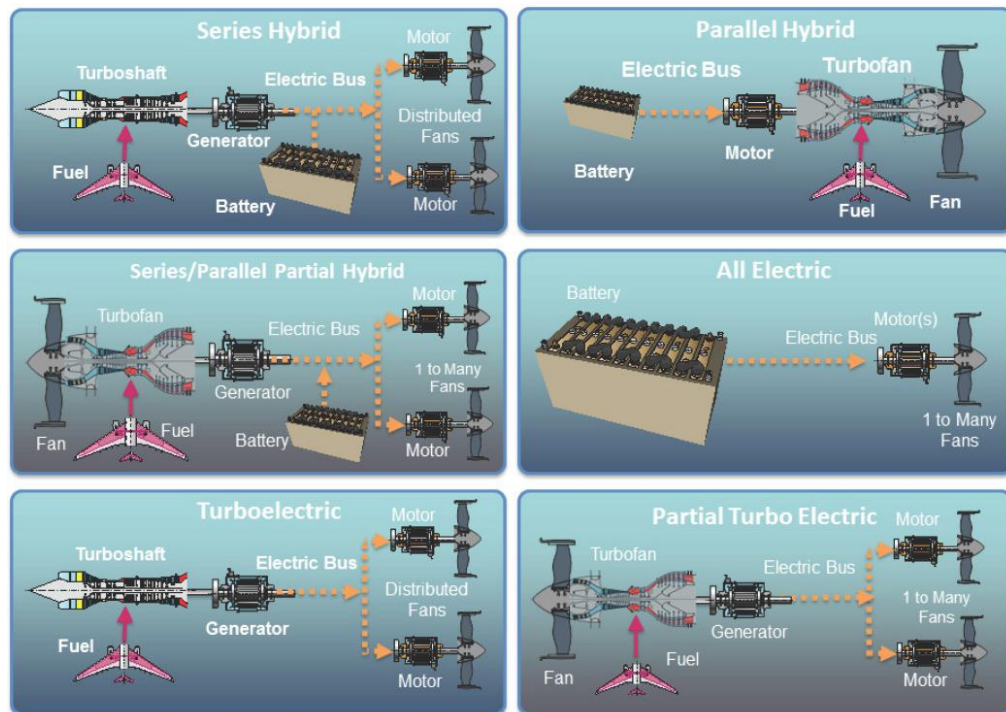
Figure 5. 1 Six electric propulsion system architectures [180].

The concept of more-electric aircraft (MEA) can be traced back to 1993. The basic idea of this new type of aircraft is to partially or fully replace the subsystems of aircraft, which use mechanical, hydraulic or pneumatic power, with electrical systems that are driven only by electric power [181]. Traditional aeroplanes use the centralized power system distribution. Generation of power is centred on the wings, usually near to the main engines of the plane, before it is transported to the front of the plane. The utilization of MEA, on the other hand, enables the simultaneous generation and distribution of power to be close to the place where it

is needed. The distance between generation and consumption is shortened, leading to lower line losses and eventually higher efficiency of power distribution. Also, decentralized power generation results in the reduced power rating of main conductors, thus cutting weight and volume of the conductors down. This effectively improves fuel efficiency while saves manufacturing costs. Moreover, this system also reduces the maintenance cost of the aircraft. Numerous researches have been done to analyse the performance of MEA in details [182-187].

One of the National Aeronautics and Space Administration's (NASA) future goals is to design a hybrid gas-electric propulsion aircraft [188]. Superconducting motors and generators are potential enabling technology to cope with the strict weight and volume limits for electric propulsion systems on aircraft. The N3-X superconducting concept aircraft, which uses the revolutionary turbo-electric distributed propulsion (TeDP) system, was proposed to meet the N+3 goals in 2014 [189]. From Figure 5. 2, the superconducting turbogenerators were mounted on the wing tips to maximize the power of the turboshaft engines. 14 superconducting motor-driven fans were located in a continuous fan nacelle to absorb the boundary-layer flow. This configuration is known as boundary layer ingestion (BLI) and it helps to reduce the total drag of the aircraft. Power was electrically distributed from the turbogenerators to motors, driving electric fans for propulsion. The TeDP system is expected to incredibly enhance the performance of future aircraft in fuel consumption, energy consumption, noise reduction, and gas emission reductions. NASA also proposed another concept, the ESAero ECO-I50 fully turboelectric aircraft concept with 150 seats [190]. Two turbogenerators were separately located at wings while 16 superconducting motor-driven fans were embedded in wings. Figure 5. 3 gives the illustration of motors used on the aircraft.
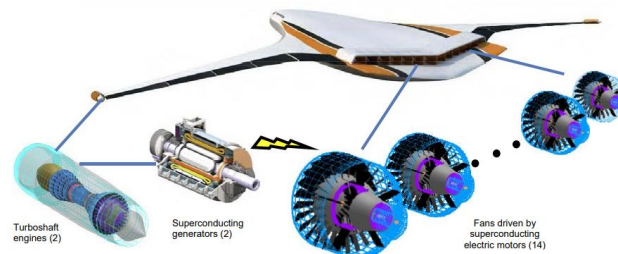
Figure 5. 2 The N3-X superconducting concept aircraft using superconducting TeDP system [189].
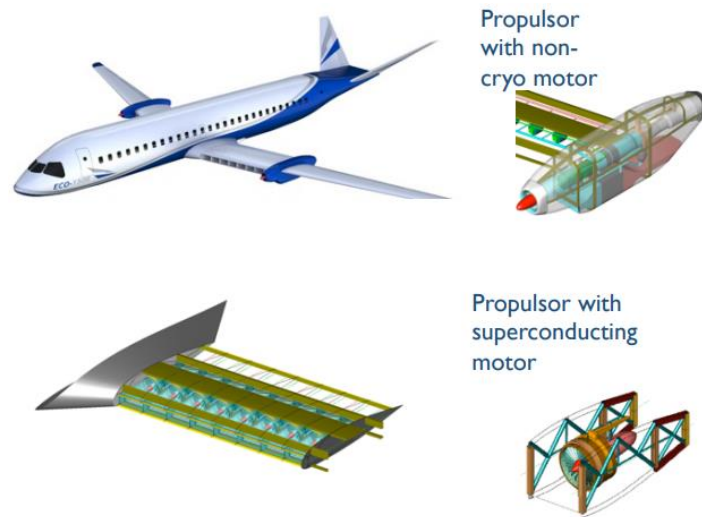
Figure 5. 3 The ESAero ECO-I50 fully turboelectric aircraft [190].

An high-temperature superconducting axial flux motor composed of 6 YBCO plates was designed for the aircraft propulsion system in 2007 [191]. A superconducting coil was wound on the outside of the motor to magnetize the plates. During the simulation process, a magnetic field of up to 6 T was successfully trapped in the YBCO plates to produce a high electromagnetic torque. This axial-flux configuration enables the storage for non-superconducting rotors and stators. Thus, conventional permanent magnet rotors can be used as a backup to generate minimum safety torque when the superconducting part loses its superconductivity. It is expected to use fuel cells or turbogenerators that are cooled down by pure hydrogen to power an all-electric aircraft. This enables the installation of a relatively simple and convenient cooling system at around 20 K.

Airbus cooperated with the Rolls-Royce Strategic Research Centre and Cranfield University to design the Distributed Electric Aerospace Propulsion (DEAP) system in 2015 [192]. Two turbogenerators are used to generate power, while eight motor-driven fans provide thrust to deliver total 9 MW. Their initial assessment indicated that although superconducting electrical conversion and distribution system had great advantage in fuel/energy consumption, the strict technology targets in the electronics efficiency as well as power density of the cryocoolers were still to be met. This is because the unignorable cryocooling requirements makes the efficiency a more essential factor to be considered than weight.

Bauhaus Luftfahrt, a German research institution, proposed a quad-fan narrow-body transport aircraft with two advanced geared-turbofans (GTFs) and two electric fans (EFs) [193]. The resulting performance of this aircraft concept indicates that efficiency of the hybrid-electric aircraft decreases significantly with the increase of degree-of-hybridization for useful power ($H_{P,USE}$). The sensitivity of the design with reference to the battery gravimetric specific energy also shows no obvious improvement in block fuel reduction, compared to conventional gas-turbine driven aircraft. Also, the narrow-body shape of the aircraft limits the volume of batteries. To improve the performance of the hybrid-electric system studied in this research, the GTFs need to be optimized to operate at peak efficiency and the EFs should be used to lower the required thrust fluctuation during cruise. Efficiency of the GTFs won't be affect by $H_{P,USE}$. Since efficiency of an HTS motor can be considered as a constant for a wide range of power levels, the thrust throttling of the EFs has no impact on efficiency of the overall propulsion system. Both the size of the electrical system and the required battery mass decide the cascading sizing effect of the aircraft. Thus, to improve the negative weight impact of the electrical system integration, future propulsion system of the hybrid-electric aircraft needs to adapt more compact approaches.

5.2 HTS tri-axial CORC cable for hybrid electric aircraft

The tri-axial CORC cable is considered to be a promising candidate for the propulsion system of a hybrid-aircraft. Figure 5. 4 gives the basic configuration of the tri-axial design on the cross-sectional view. Three electrical superconducting phases of the cold dielectric cable are concentrically arranged around a single core (not shown in the figure) in cryogenic dielectric materials [194]. Most of the previous cold dielectric HTS cables have used the coaxial design, of which several layers of HTS tapes are required to compose both the forward and return superconducting paths to eliminate the external magnetic fields. Different from the co-axial design, the tri-axial configuration has a 3-phase delta-connected co-axial scheme, which means that the vector sum of 3-phase currents equals to zero. Thus, the net external magnetic field of a tri-axial cable is small enough to be ignored. Since there is no need to build superconducting return path, the use of HTS tapes is significantly reduced. Thus, the capacity of the cryogenic system is also reduced accordingly. The reduced usage of materials, as well as easier design

requirements of the cooling system, makes the triaxial cable structure a promising candidate for power applications that require high power capacity but have limited space.

The first Russian tri-axial HTS cable prototype has been developed and tested [195]. A 10 kV, 40 MVA high-temperature superconducting system consisting of an AC tri-axial HTS cable with a length of 1 km has been installed in a real grid application in Germany [196]. The power level of modern aircraft has reached 1 MW, and is expected to be in the range of a few MW to tens of MW for future fully electric aircraft, according to its size [195]. Compared with conventional conductors, the lighter, smaller HTS tri-axial power cable with higher efficiency is the most advanced cabling technology for transporting current on board of aeroplanes. Combined with the tri-axial design, the CORC cabling concept is used to helically wind the ReBCO tapes along the axial direction to construct the newly-proposed tri-axial CORC cable, in the aim of achieving compact structure, high power density and reduced use of ReBCO tapes.
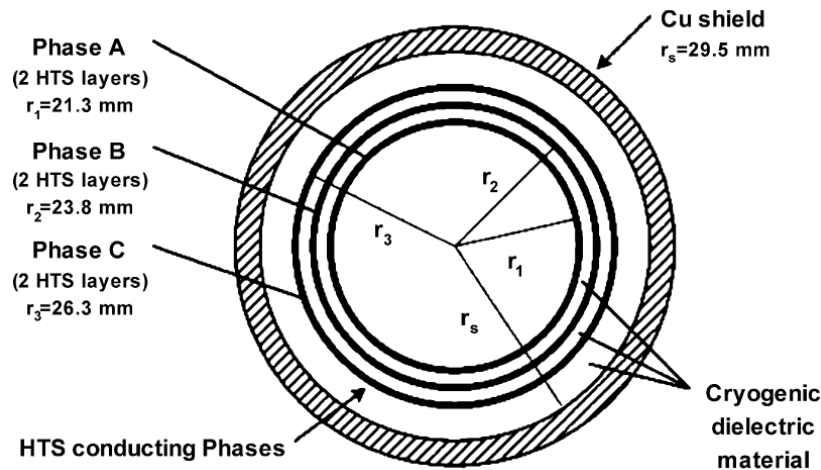
Figure 5. 4 Cross-section of HTS tri-axial cable with 3 superconducting phases. The shielding layer is made from copper [194].

A project has been conducted by our group to develop a superconducting propulsion system for hybrid-electric aircraft [197]. So far, a 10 MW tri-axial CORC cable with a rated voltage of 3 kV_{rms} and a rated current of 2 kA_{rms} has been developed. Detailed analysis of AC losses of this cable is needed to prove the validation of this cable. The aforementioned study has already analysed the electromagnetic behaviours of CORC cables under a wide range of transport currents and external magnetic fields. For a practical propulsion system of an electric aircraft,

induced harmonic currents in generators/motors, as well as AC/DC converters, are unavoidable [198], which might have a significant impact on the total AC losses of the cable. According to [199], for single HTS wires, including the YBCO wires, the non-magnetic substrate won't affect the magnetic field distribution and AC losses of the wires. This indicates that the magnetization losses generated by transport currents contribute almost all the AC losses of the tapes. Eddy losses generated in the non-ferromagnetic metallic layers of the ReBCO tapes are small enough to be ignored. A 2-dimensional numerical T-A model is built to analyse the influence of harmonic current on the AC losses of the proposed tri-axial CORC cable designed for hybrid-electric aircraft. Note again that only magnetization losses in the superconducting layers are considered in this research.

5.3 Specification of the tri-axial CORC cable

The initial target is of this chapter is to design a tri-axial CORC cable that can deliver propulsion power of 10 MW from the generator to the motors. Specification of the cable proposed in this chapter is given by the previous study from our research group [3, 200]. It has an operating frequency of 50 Hz. The operating temperature of the cable is 70 K. The cross-section of the cable is presented in Figure 5. 5. This 2D model for HTS tri-axial CORC cable takes the copper formers, dielectric materials, and the shielding layer into consideration. 28 ReBCO tapes are wound helically around a stainless-steel former for each phase. The ReBCO tape used here is the same with that mentioned in the previous chapters and has a Hastelloy substrate and a copper stabilizer. Each tape has I_c=150 A at 70 K in self-field while I_c of each tape during operation is around 140 A. The rated peak transport current, I_p, is 100 A. The refrigerant being filled in the channels of the inner and outer formers is liquid nitrogen (LN$_2$). The red circular area in the cross-section of the cable represents three phases of the cable. Kapton is used as dielectric material to fill in the gaps between phases and gaps between layers. Cooper shielding layer is mounted on the outer former. It is grounded to prevent overrated voltage from damaging the cable. The detailed specification of the cable is given in Table 5.1.
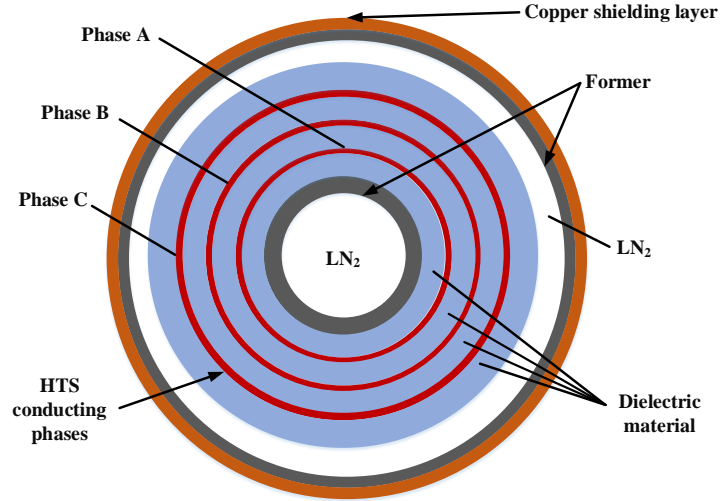
Figure 5. 5   Cross-section of the HTS tri-axial CORC cable studied in this chapter.

Table 5. 1 Specifications of the HTS tri-axial CORC cable designed for hybrid-electric aircraft [201].

Parameters		Material/Quantity
Cable	Phase	3
	Power	10 MW
	Voltage	3 kV_{rms}
	Current	2 kA_{rms}
	Frequency	50 Hz
ReBCO tape	Tapes per phase	28
	Width/Thickness	4 mm/0.1 mm
	Operating temperature	70 K
	Critical current, I_c @ 70 K	150 A
	Peak operating current, I_p	100 A
Inner former	Material	Stainless-steel
	Diameter/thickness	25 mm/0.3 mm
Outer former	Material	Stainless-steel
	Diameter/thickness	99.2 mm/2 mm
Insulation	Material	Kapton
	Thickness	8 mm

5.4 2D tri-axial CORC cable model development

5.4.1   A full cross-sectional 2D model

COMSOL Multiphysics is used to build and solve this 2D FEM T-A tri-axial CORC cable model. Figure 5. 6 (a) presents the cross-sectional geometry of this 2D model. Since the ReBCO tapes are the main research objects that generate losses, they need extra fine element size for more precise results. The Distribution node is used to specify the distribution of mesh elements along the thin lines that represent the ReBCO tapes. Each tape is divided into 50 segments with an element ratio of 3. Since the symmetric distribution is chosen, the element ratio applied to the tape makes the elements on the edges of the tape 3 times finer than that on the middle part of the tape. After specifically defining the distribution of mesh on ReBCO tapes, free unstructured triangular mesh is created on the entire domain of this 2D model. The final mesh of this model is shown in Figure 5. 6 (b).

(a)

(b)
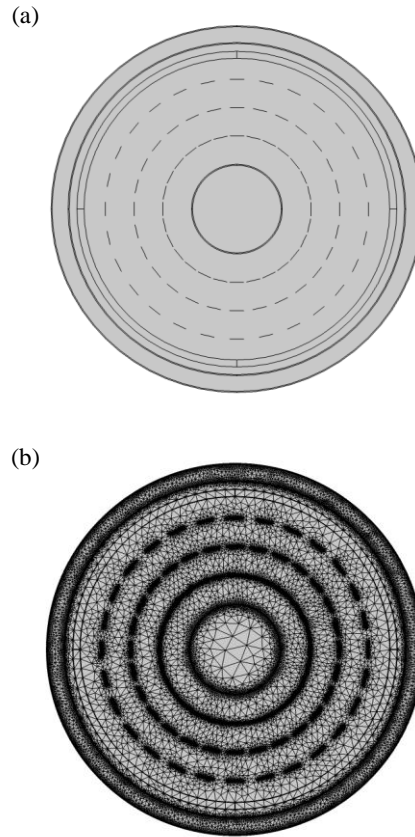
Figure 5. 6 Mesh of the FEM 2D model based on T-A formulation for tri-axial CORC cable.

The outer boundary of this model is hidden in this graph.

125

The electrical conductivity of the stainless-steel formers used here is 2 MS/m, while the electrical conductivity of the copper shielding layer is 650 MS/m. The remaining domains are superconducting tapes with electrical conductivity of 10 S/m. Two of the three-phase currents are ramped using the ramp function in COMSOL to distinguish their start time of the current wave from phase A. Waveform of the three-phase operating currents of the tri-axial CORC cable is presented in Figure 5. 12.

5.4.2 A 1/28 sector-shaped 2D model

Since the cross-section of the tri-axial CORC cable is fully axisymmetric, it is reasonable to reduce the model size to a small portion of the cable's cross-section, as the simulation results will be identical to the rest portions of the cable. A sector-shaped model was built to represent a 1/28 continuous circumferential cross-section of the cable. Figure 5. 7 presents the basic geometry of the sector 2D model. The sector area including both the cross-section of the superconducting cable as well as the outer boundary of the model. Three adjacent ReBCO tapes that are from three phases respectively are simulated in this model.

Electromagnetic behaviours (including the field and current distribution) that are near boundaries of a model will be considerably influenced by the settings of the boundary conditions. Location of the boundaries of a sector model as well as the illustration of the periodic boundary conditions (PBC) is presented in Figure 5. 8. For a sector model, the circumferential PBC involves a simple principle; the particle that moves out of a periodic boundary (e.g. PB1 in Figure 5. 8 (b)) can be considered as keeping moving into the other periodic boundary (e.g. PB2 in Figure 5. 8 (b)) [202]. The only difference between particle 1 and 1' (as well as particle 3 and 3') is the relative location within the model. These two particles have identical properties.

For the tri-axial CORC cable, two radii of this sector-shaped model have an electromagnetic periodic connection with their surrounding area of the cable. As the CORC cable are fully symmetric, it is reasonable to say that the upper boundary (upper radius) is magnetically connected with the lower boundary (the lower radius). Relative position at both radii of the sector-shaped geometry is equal, with both radii equally oriented by two coordinate systems, as the example geometry shown in Figure 5. 9. Thus, the destination boundary on the graph is simply geometrically translated from

the source boundary along the axial direction. COMSOL Multiphysics only needs to force the solution of the state variables at each point on the destination boundary to be exactly the same with the solution at the surface of the corresponding source boundary [203]. When setting the magnetic field's interface of this 1/28 sector-shaped model, a circumferential periodic condition is applied to two radii of the sector to define continuous periodicity between radii and the connected surroundings. The settings are given in Figure 5. 10 (a). As shown in Figure 5. 10 (b), the upper radius of the 1/28 sector is chosen to be the destination boundary of the periodic condition.
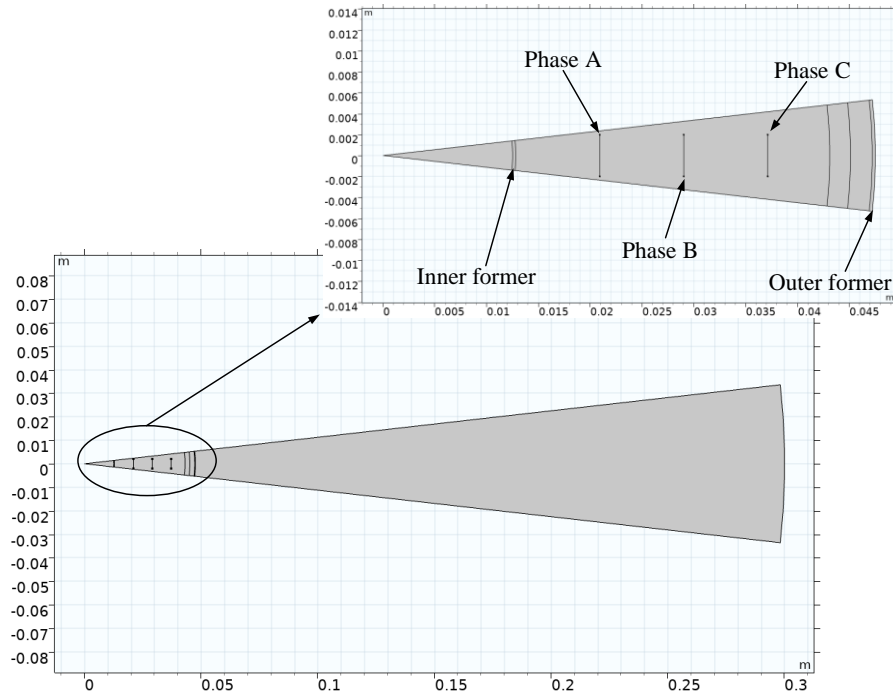
Figure 5. 7 The geometry of the 1/28 sector 2D tri-axial CORC cable mode.
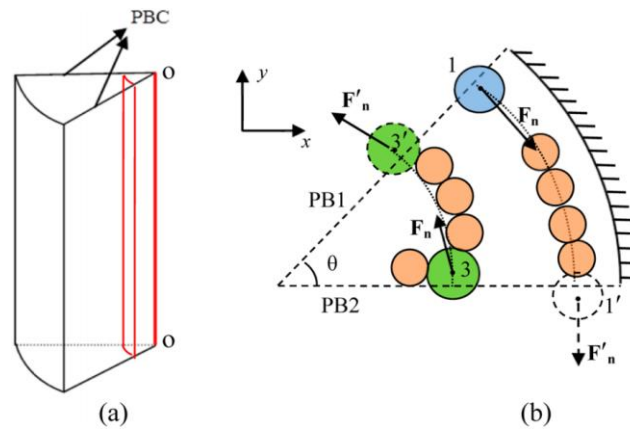
Figure 5. 8 (a) Location of the boundary of a sector model; (b) Circumferential periodic boundary condition [202].

127
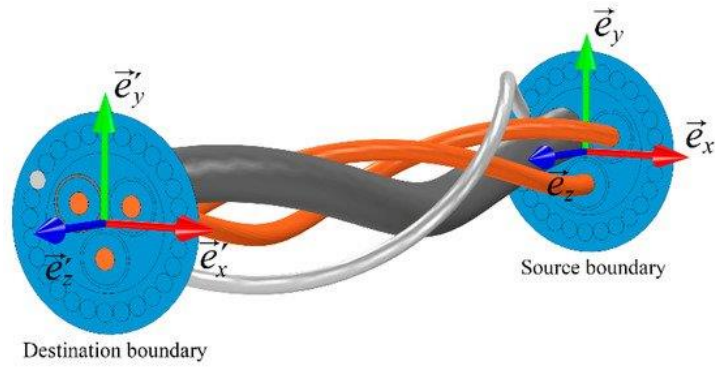
Figure 5. 9 Boundary orientation for model with periodic geometry [203].
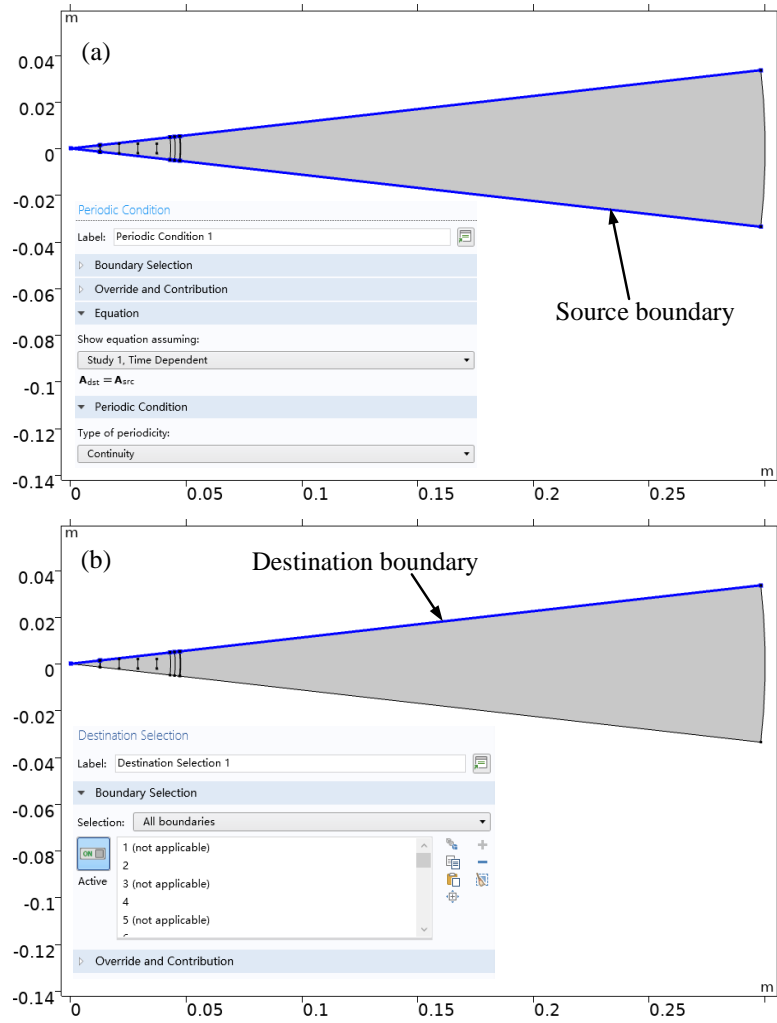
Figure 5. 10 Settings of (a) the Periodic condition on radii of the sector model; and (b) the

destination selection.

Construction of the mesh of the sector model involves three separate settings. The size of mesh elements for the cooling channels inside the inner former, as well as between the dielectric materials

and the outer former, is calibrated as extremely fine. The allowed element size of the inner and outer formers is limited by a maximum of 0.3 mm to ensure precise simulation result. Same with the full cross-sectional model, distribution of mesh elements along the three lines that represent superconducting tapes in the sector model is specified using the distribution node in the mesh physics. Instead of 50, each tape is divided into 60 segments with an element ratio of 3. The remaining geometry are meshed into free triangles. The final mesh construction is plotted in Figure 5. 11.
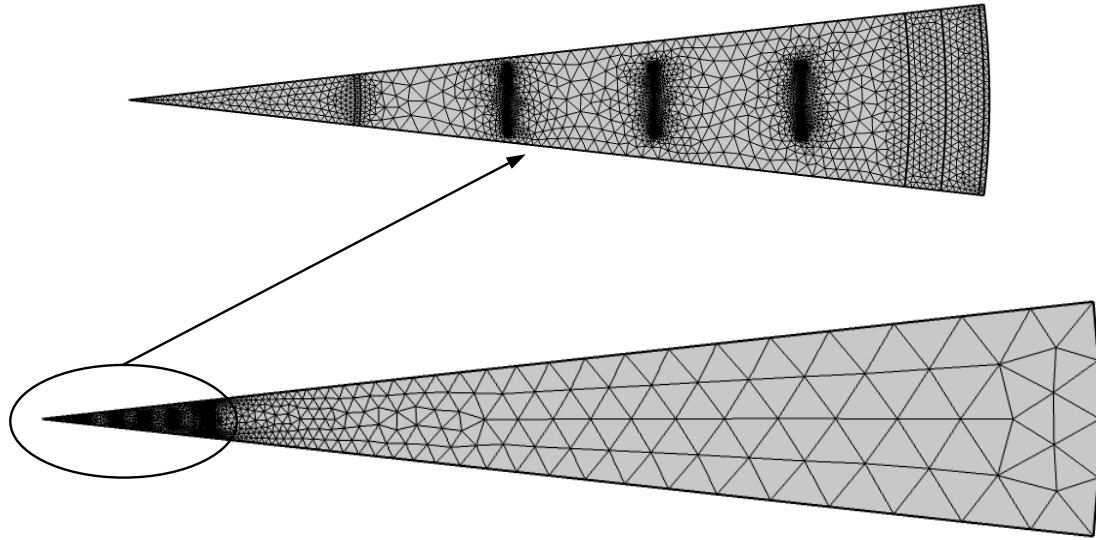
Figure 5. 11 Mesh of the 1/28 sector model based on T-A formulation for tri-axial CORC cable.

5.5 Transport AC loss calculation

5.5.1 Balanced rated load without harmonic current

For simplicity, in this section of study, only the transport loss of the cable has been analysed. Firstly, the case when only the three-phase operating currents with a magnitude of 100 A exist in each phase during the operation process is studied. The harmonic current is not considered in this part of the study. The fundamental frequency, f_1, of the cable is 50 Hz. The transport loss in a unit length of the cable varies with time under a balanced rated load is calculated using the proposed 2D model.

From Figure 5. 13, although each phase of the cable transported the same magnitude of current, the transport losses generated in three phases still show significant imbalance. The innermost phase, phase A, produced the lowest loss among the three phases. The peak value of loss in phase A is around 0.42 W/m. Loss generated in the middle phase (phase B) reaches 0.95 W/m, which is doubled compared with that of phase A. The outmost phase, phase C, contributes the largest value of transport losses, which is around 1.18 W/m. It is almost three times more than the loss in phase A. The time when the transport loss reaches its peak value is not simultaneous with the time when the current of each phase rises to its maximum value. Reason for this is that the transport loss does not depend only on the transport current. The critical current, which is field-dependent, also has an impact on the generation of AC losses. Moreover, the loss generated on ReBCO tapes in one phase is considerably affected by the other two phases, due to the magnetic coupling process among phases during operation.

The dependence of the transport loss on the magnitude of three-phase operating currents is presented in Figure 5. 14. It clearly shows that the transport losses of the tri-axial CORC cable rise rapidly with the increase of the operating current. The increasing rates of losses in each phase are given in Figure 5. 15. When the operating current increases from 40 A to 60 A, the losses in three phases all tripled, while the loss in Phase C is almost four times larger than before. This means that under relatively low current range, a slight increase of current results in a significant rise of transport losses in all three phases. The increasing rate decreases sharply after the operating current is higher than 60 A in three phases. This indicates that higher operating current will have a lower influence on the generation of transport losses of tri-axial CORC cable.
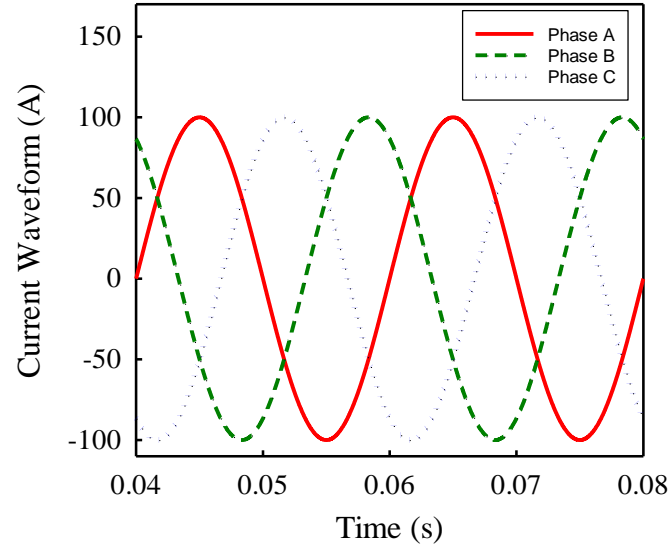
Figure 5. 12 Waveform of the three-phase operating currents.
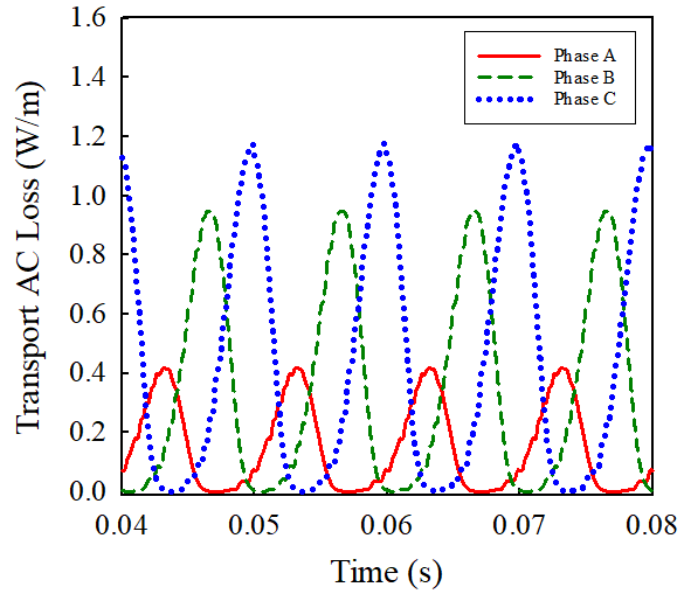
Figure 5. 13 Variation of the transport loss of the tri-axial CORC cable during operation. The

cable is under a balanced rated load. I_{op} = 100 A, fundamental frequency f_1 = 50 Hz.
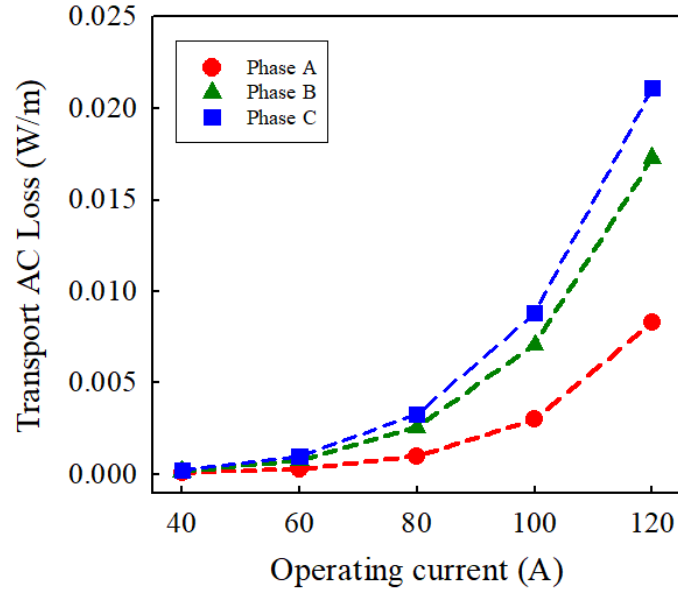
Figure 5. 14 Transport loss of tri-axial CORC cable for a full-cycle time against operating current under a balanced rated load. No harmonic current exists.

Figure 5. 15 The increasing rate of transport losses in each phase with the increase of operating current.

The dependence of transport loss on the operating fundamental frequency is presented in Figure 5. 16. In the previous published paper, the transport loss was given for a duration of one second, as can be seen from Figure 5. 16 (a) [201]. For comparison, the loss generated for only a full-cycle time in each phase is also presented in Figure 5. 16 (b). The linear increase of loss in each phase in Figure 5. 16 (a) proves that the transport loss per cycle time (*J/cycle*) is

independent with the frequency in the tri-axial CORC cable, which is consistent with previous studies done by other research groups [171, 204]. Meanwhile, losses in each phase for the duration of a second only decrease slightly with the increase of frequency, which further proves the frequency independence of transport loss of tri-axial CORC cable.

The calculation of transport loss in each phase of the tri-axial CORC cable shows that, despite the fact that the three phases have the same load and there is no harmonic current induced, losses among three phases still have a considerable non-uniform distribution. This is probably due to the tri-axial geometry causes the non-uniform distribution of magnetic fields among three phases.
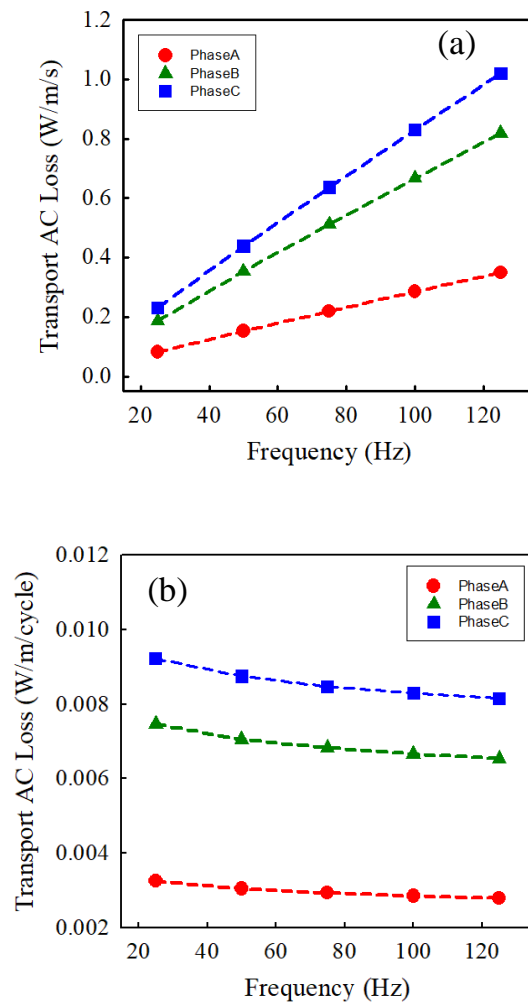
Figure 5. 16 Transport loss of tri-axial CORC cable for a duration of (a) one second; and (b) a full-cycle time; against operating fundamental frequency under a balanced rated load. No harmonic current exists.

5.5.2 Balanced rated load with harmonic current

The harmonic currents were applied to the tri-axial CORC cable in the aim of analysing the influence of the harmonics on the AC losses of the cable. Notice that the operating transport current, which is 100 A here, is applied simultaneously with the harmonic currents. Calculation of the transport losses in this section includes losses generated by the operating current and the harmonic current together.

The magnitude of the harmonic current varies from 2 A to 15 A, while the harmonic frequency is from the second harmonic to fourth harmonic. All the harmonic currents applied to the model are in-phase sinusoidal signals. Firstly, to verify the accuracy and reliability of the presented 1/28 sector-shaped model, the transport loss of a single tape in each phase of the cable is calculated using both 2D models. The comparison result is given in Figure 5. 17. The losses calculated from both models are exactly the same, which validates the sector model. 'Moreover, at the moment when the peak values of losses are generated, the loss curve calculated from the sector model is smoother than that from the full cross-sectional model. This comparison indicates that for calculation of AC losses of the tri-axial CORC cable, it is totally reasonable and reliable to use the sector model to lower the memory requirement and shorten the computation time.

The transport loss generated in the tri-axial CORC cable with a harmonic current of 10 A/200 Hz applied on each phase is presented in Figure 5. 18. The existence of harmonic current obviously causes a notable change on the transport loss of tri-axial CORC cable. The overall loss is almost doubled, compared with loss generated by operating current only. From Figure 5. 18, there are three peaks of losses induced during a full-cycle time for each phase. The distribution of the normal magnetic field and the normalized current density (J_c/J_c) at the peak points of losses given in Figure 5. 18 is extracted from the 1/28 sector-shaped model and presented in Figure 5. 19. The background magnetic field of each phase has a dependence on the fields of the other two phases. The magnitude of the loss in each phase depends on both the operating current in that phase and the current flowing in the other two phases. In one word,

the curve of the transport loss with three different peak values is caused by the comprehensive electromagnetic coupling between phases.
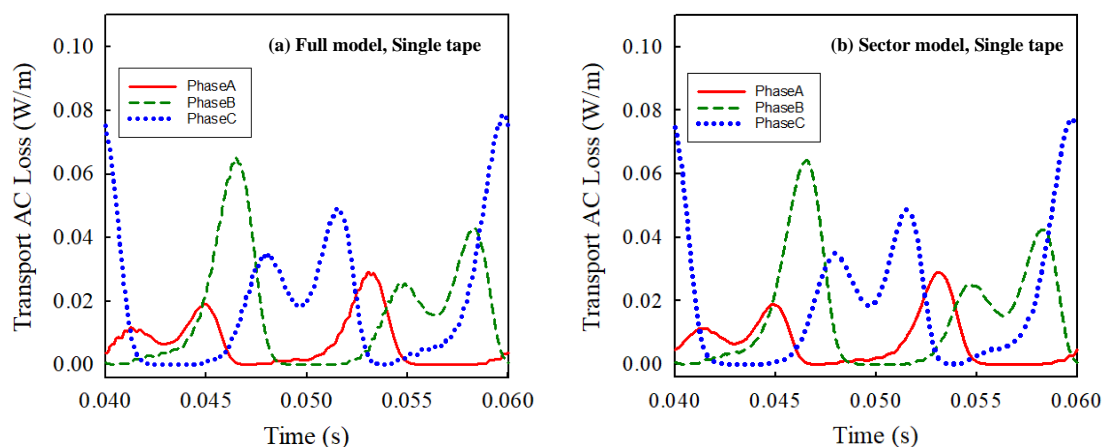
Figure 5. 17 Comparison of transport loss of a single tape in each phase of the tri-axial CORC cable calculated using (a) the full cross-sectional model; and (b) the 1/28 sector-shaped model. $f_1 = 50$ Hz, $I_{op} = 100$ A, $f_4 = 200$ Hz, $I_4 = 10$ A.
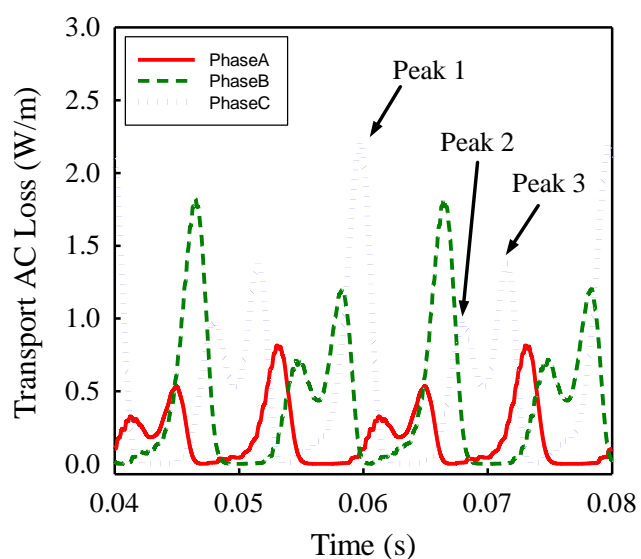
Figure 5. 18 Transport loss of the tri-axial CORC cable under rated load with a harmonic current with a magnitude of 10 A. $f_1 = 50$ Hz, $f_4 = 200$ Hz, $I_{op} = 100$ A.

(a) Magnetic flux density, B_{norm} (b) Normalized current density, J_{norm}/J_c
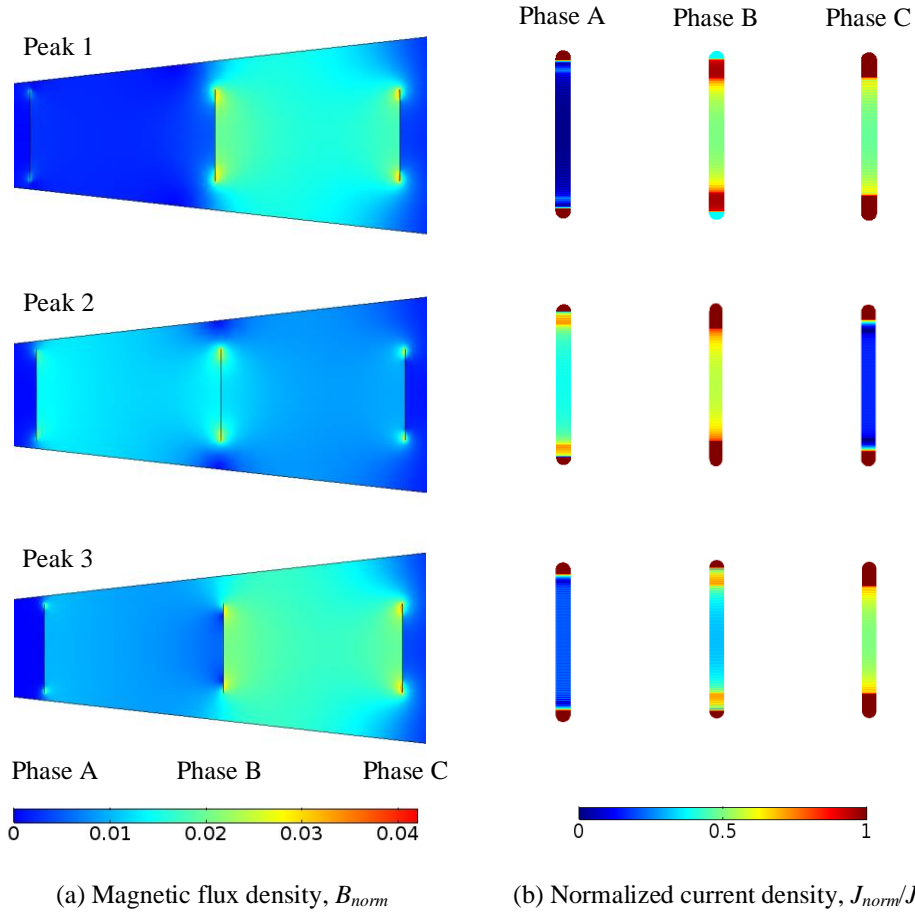
Figure 5. 19 (a) The normalized magnetic field density and (b) the normalized current density of 1/28 sector of the cross-section of the tri-axial CORC cable under a balanced rated load. f_1 = 50 Hz, I_{op} = 100 A. The harmonic current has a magnitude of 10 A and a frequency of 200 Hz.

The influence of harmonic current is also analysed by independently varying the frequency or the magnitude of the harmonic current to see the variation of the losses among phases. Figure 5. 20 presented the losses in three phases when a harmonic current with a magnitude from 2 A to 15 A is applied to each phase. The harmonic frequency is fixed at 200 Hz. The tri-axial CORC cable still delivers a balanced rated load in this case, and the harmonic currents pulse the rated load to generate transport loss in the cable. A considerable increase of transport loss is shown with the increase of the magnitude of the harmonic current. However, the increasing trends in the three phases are slightly different from each other. The loss calculated after applying the harmonic current is compared with the loss generated by a transport current of 100 A only (which is plotted in Figure 5. 14). The comparison result is given in Figure 5. 21. It is obvious

136

that when the magnitude of the applied harmonic current is low, which is only 2 A in this case, the existence of harmonic current hardly increases the AC loss of the cable. The increase of the magnitude of harmonic current causes an increase in loss generation in each phase. With the magnitude increases to up to 15 A, loss in the innermost phase A is creased by 53.3%, while losses in the other two phases are increased by around 45% only.
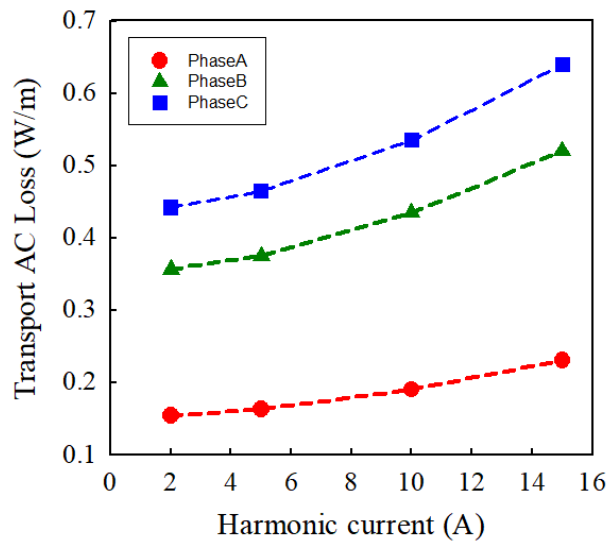
Figure 5. 20 The transport loss of the tri-axial CORC cable against the magnitude of a

harmonic current with a fixed frequency of 200 Hz. f_1 = 50 Hz, I_{op} = 100 A.
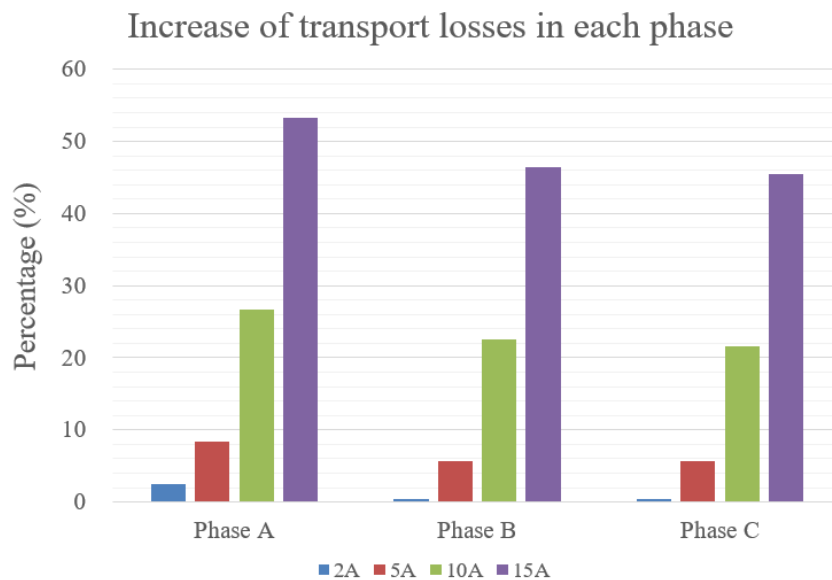
Figure 5. 21 Percentage of increase of transport loss in each phase after applying the

harmonic current with different magnitudes, compared with loss generated by a transport

current of 100 A under 50 Hz only. The harmonic frequency is 200 Hz.

The increasing rate (%) of loss in each phase in corresponding to the increase of harmonic frequencies is then analysed. A harmonic current of 10 A is applied to each phase, with its harmonic frequency varies from 100 Hz to 1000 Hz. Results are presented in Figure 5. 22. When the harmonic frequency is low, e.g. range from 100 Hz (2nd order harmonics) to 500 Hz (10th order harmonics), the transport loss increases sharply with the rise of harmonic frequency. However, with a higher order of harmonic frequency applied, e.g. higher than 800 Hz (16th order harmonics) here, the increasing rate of transport loss in each phase of the tri-axial CORC cable slowly stops rising and becomes stable. The results also further prove that when a harmonic current is simultaneously applied to each phase of the tri-axial CORC cable, it has a maximal impact on the innermost phase of the cable, and affects the outermost phase the least.
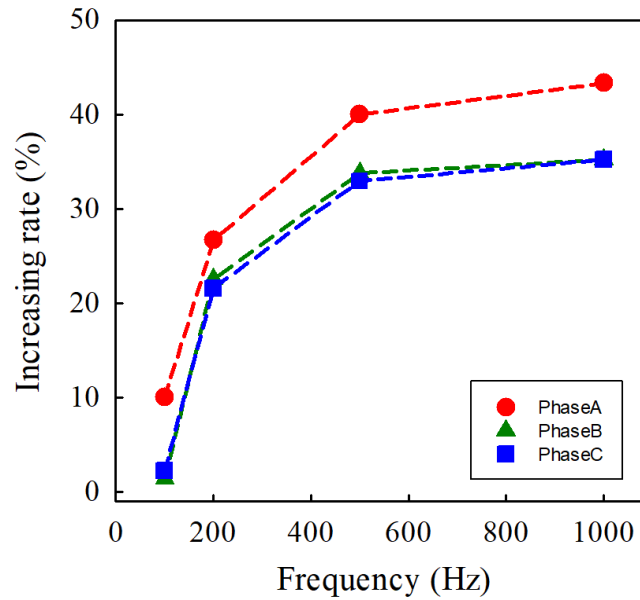
Figure 5. 22 Increasing rate of the transport loss of the cable against frequency of a harmonic current with a fixed magnitude of 10 A. f_1 = 50 Hz, I_{op} = 100 A.

5.6 Summary

This chapter aims at designing an HTS tri-axial CORC cable (3 kV/2 kA) to deliver propulsion power of up to 10 MW for the propulsion system of hybrid-electric aircraft. Analysis of how the harmonic current affects the AC transport loss of the cable was carried out numerically. Two different 2D FEM T-A models were proposed using COMSOL Multiphysics for the simulation of the electromagnetic behaviours of the cable. The first one was a full cross-sectional model,

which simulates the full cross-section of the tri-axial CORC cable. Taking advantage of the fully axisymmetric geometry of the cable, a 1/28 sector-shaped model was then built to fasten the simulation while maintaining the accuracy of the results. Key settings of both models, including the setting of boundary conditions and the construction of the mesh, were given in details.

The tri-axial CORC cable studied here operated under a balanced rated load. Firstly, the comparison of the losses calculated from two models was made to validate the proposed sector-shaped model. Then, transport loss generated by an operating current of 100 A under a fundamental frequency of 50 Hz was calculated and used as a reference value for the following study. The result showed that though a balanced rated load was used, the non-uniform distribution of the magnetic field among three phases still led to an imbalance in the distribution of losses. How the harmonic currents affect the variation of the transport AC loss of the cable was analysed using both models. The transport loss in each phase increases dramatically with the amplitude and frequency of the applied harmonic current. A small harmonic current with a magnitude less than ten percentage of the rated current caused a considerable increase in transport losses. On the other hand, when the harmonic frequency was high enough, the transport AC losses started to show frequency independence. Also, the increasing rate of the transport losses generated in the innermost phase is mostly affected by the increase of the frequency, while the outermost phase has the lowest increasing rate among the three phases.

Chapter 6. Conclusions and future work

6.1 Conclusion of the PhD's work

The aim of this thesis is to perform a thorough numerical study on the HTS conductor-on-round-core (CORC) cable. A novelty of this thesis lies in the use of a new set of numerical formulation, the T-A formulation. This new formulation is, for the first time, applied to three-dimensional (3D) modelling of CORC cable with practical structure. Several numerical simulation models have been developed using COMSOL Multiphysics for the aim of analysing both the electromagnetic and quench behaviour of the CORC cable. The efficient simulation tools proposed in this thesis provide valuable guidance in designing HTS CORC cables with minimized AC losses for applications with high-field, energy conversion and energy transmission.

Chapter 2 gave a basic introduction to the development of the field of superconductivity. History, fundamental properties, as well as the classification of superconductivity was presented. Then, a detailed literature review was presented regarding three cutting-edge superconducting cabling concepts. Finally, as this thesis focused on the numerical study, an introduction on three types of modelling methods; the analytical, differential and integral methods, was presented.

The first numerical model proposed in this thesis was a novel 3D model based on the T-A formulation, which was presented in Chapter 3. By applying the T-A formulation to the model, the modelling difficulties in a three-dimensional coordinate caused by the helicity of the CORC cable were successfully overcome. Two steps of validation were taken, in both the numerical and experimental way, to ensure the validity and accuracy of the proposed 3D T-A model. A single-layer CORC cable sample and a double layer CORC cable sample were simulated using this model. The dependence of the AC loss of the cable on the transport current and the external magnetic field was analysed. Then, three novel 2D T-A models were proposed to further shorten the computation time as well as to lower the memory requirement. By taking both the direction of the transport current and the size of air gap on the cross-section of the cable into consideration,

the Advanced 2D T-A model was proved to be able to accurately simulate multi-layer CORC cables with higher efficiency and lower requirement on the hardware.

A novel 3D quench model was proposed in Chapter 4 to thoroughly study the quench behaviour of the CORC cable. Four different modules were coupled together to form this quench model. Multi-physics properties of this quench model were introduced in details. The influence of uniform terminal contact resistance was first studied by inducing a hotspot-induced quench on one of the tapes of the cable. The current redistribution among tapes, variation of voltage and temperature, and the normal zone propagation on the target tape were analyzed and discussed. The MQE under various uniform TCRs was calculated to show the dependence of MQE on TCRs. Then, the influence of non-uniform TCRs (which is more realistic in practical applications) on the quench behaviour of the cable was studied. The tape with a moderate value of TCR had the highest MQE, which means it was the most stable one among three tapes. Meanwhile, the tape with the lowest TCR has the lowest MQE, which represents the worst thermal stability.

Finally, the design concept of a 10 MW/3 kV/2 kA HTS tri-axial CORC cable was proposed in Chapter 5 in the aim of improving the propulsion system of hybrid-electric aircraft. This chapter focused on the influence of harmonic current on the magnetization AC loss of the tri-axial CORC cable. A full cross-sectional 2D T-A based model was built to simulate the operation process of this cable. In addition, a 1/28 sector-shaped 2D model was developed to simulate only a small sector of the cable's cross-section. Simulation results of these two models agreed well with each other. The magnetization AC loss of the cable was calculated under a balanced rated load with and without the existence of harmonic current. Results showed that the distribution of losses among the three phases are significantly uneven, although there was no harmonic current applied. The losses increased rapidly with the amplitude and frequency of the applied harmonic current. The innermost phase of the cable was mostly affected by the variation of harmonic frequency, while the outermost phase is affected the least. However, when the harmonic frequency reached a certain stage, i.e. the 16th harmonic frequency, the magnetization loss of the cable was frequency independent.

6.2 Possible future work

Although the numerical models proposed in this thesis have given some reliable and useful simulation results for analysing the electromagnetic and quench behaviours of the HTS CORC cables, further efforts are still necessary. Future work regarding the study on the HTS CORC cable will be;

- Using the 3D T-A model to simulate three and more layers of CORC cables and study the electromagnetic as well as the quench behaviour of these multi-layer CORC cables. Although several 2D T-A models have also been proposed here for the simulation of industry-scale CORC cables, improvement on the 3D T-A model still needs to be made, as the 2D model cannot fully present the distribution of field and current among layers along the axial direction of the cable.

- Further studies on how the winding angle, pitch length and packing arrangement of air gaps in each layer of the cable affect the AC losses of the HTS CORC cables, and how these influences can be reduced.

- Investigation on how the striated ReBCO tapes can be used to reduce the AC loss of the HTS CORC cables at high magnetic fields, in comparison to its un-striated counterpart.

- Following the quench behaviour analysis of this thesis, a detailed study on the quench detection and quench protection for the operation of HTS CORC cable will be carried out to better prevent the cable from potential damage caused by the quench.

- The proposed design concept of the tri-axial CORC cable for the propulsion system of the hybrid-electric aircraft was analysed numerically in this thesis. The future work will be focused on the experimental validation of this cable sample. A cable sample will be wound and tested. The measured AC loss will be compared with the numerical results.

References

[1]   CarbonBrief. (2016, 3 Sep). *Analysis: Aviation could consume a quarter of 1.5C carbon budget by 2050*. Available: https://www.carbonbrief.org/aviation-consume-quarter-carbon-budget

[2]   J. Whitelegg, "AVIATION: the social, economic and environmental impact of flying," *Ashden Trust, London,* 2000.

[3]   S. Venuturumilli, "Superconducting cables for electric aircraft," University of Bath, 2019.

[4]   A. V. Narlikar, *High Temperature Superconductivity 2*. Springer Science & Business Media, 2013.

[5]   A. Malozemoff, J. Yuan, and C. Rey, "High-temperature superconducting (HTS) AC cables for power grid applications," in *Superconductors in the power grid*: Elsevier, 2015, pp. 133-188.

[6]   D. C. van der Laan, J. D WEISS, and D. McRae, "Status of CORC® cables and wires for use in high-field magnets and power systems a decade after their introduction," *Superconductor Science Technology,* 2019.

[7]   D. van der Laan, F. Douglas, X. Lu, U. Trociewitz, and D. Larbalestier, "Conductor on Round Core (CORC) cable development for accelerator magnets," in *WAMHTS*, 2014.

[8]   J. D. Weiss, T. Mulder, H. J. ten Kate, and D. C. van der Laan, "Introduction of CORC (R) wires: highly flexible, round high-temperature superconducting wires for magnet and power transmission applications," *Superconductor Science & Technology,* vol. 30, no. 1, Jan 2017, Art. no. 014002.

[9]   M. Vojenciak *et al.*, "Magnetization ac loss reduction in HTS CORC (R) cables made of striated coated conductors," *Superconductor Science & Technology,* vol. 28, no. 10, Oct 2015, Art. no. 104006.

[10]   T. Mulder *et al.*, "Design and Manufacturing of a 45 kA at 10 T REBCO-CORC Cable-in-Conduit Conductor for Large-Scale Magnets," *Ieee Transactions on Applied Superconductivity,* vol. 26, no. 4, Jun 2016, Art. no. 4803605.

[11]   D. C. van der Laan *et al.*, "Engineering current density in excess of 200Amm(-2) at 20T in CORC (R) magnet cables containing RE-Ba2Cu3O7-delta tapes with 38 mu m thick substrates," *Superconductor Science & Technology,* vol. 28, no. 12, Dec 2015, Art. no. 124001.

[12]   A. C. T. LLC. (2018). *In the News: DOE Office of Science*. Available: https://www.advancedconductor.com/2018/05/17/in-the-news-doe-office-of-science/

[13]   D. van der Laan, "Development of HTS CORC cables for high field magnets and advanced power transmission," *Cold Facts,* vol. 31, no. 3, pp. 22-23, 2015.

[14]   L. Cooley and I. Pong, "Cost drivers for very high energy pp collider magnet conductors," *FCC Week,* 2016.

[15]   Y. Wang, M. Zhang, F. Grilli, Z. Zhu, and W. Yuan, "Study of the magnetization loss of CORC cables using 3D TA formulation," *Superconductor Science and Technology,* 2018.

[16]   F. Trillaud *et al.*, "Normal zone generation and propagation in YBa2Cu3O7− δ coated conductors initialized by localized, pulsed disturbances," in *AIP Conference Proceedings*, 2004, vol. 711, no. 1, pp. 852-859: American Institute of Physics.

[17]   F. Trillaud, H. Palanki, U. Trociewitz, S. Thompson, H. Weijers, and J. Schwartz, "Normal zone propagation experiments on HTS composite conductors," *Cryogenics,* vol. 43, no. 3-5, pp. 271-279, 2003.

[18]   S. Honghai and J. Schwartz, "Stability and quench behavior of YBa2Cu3O7− x coated conductor at 4.2 K, self-field," *IEEE Trans. Appl. Supercond,* vol. 19, pp. 3735-3743, 2009.

[19]   C. Thieme, K. Gagnon, J. Coulter, H. Song, and J. Schwartz, "Stability of second generation HTS pancake coils at 4.2 K for high heat flux applications," *IEEE transactions on applied superconductivity,* vol. 19, no. 3, pp. 1626-1632, 2009.

[20]   X. Wang *et al.*, "Normal zone initiation and propagation in Y-Ba-Cu-O coated conductors with Cu stabilizer," *IEEE transactions on applied superconductivity,* vol. 15, no. 2, pp. 2586-2589, 2005.

[21]   X. Wang, U. Trociewitz, and J. Schwartz, "Near-adiabatic quench experiments on short Y Ba 2 Cu 3 O 7− δ coated conductors," *Journal of Applied Physics,* vol. 101, no. 5, p. 053904, 2007.

[22]   X. Wang, U. Trociewitz, and J. Schwartz, "Self-field quench behaviour of YBa2Cu3O7− δ coated conductors with different stabilizers," *Superconductor Science Technology,* vol. 22, no. 8, p. 085005, 2009.

[23]   F. Trillaud, M. C. Ahn, J. Bascunan, W.-S. Kim, J. P. Voccio, and Y. Iwasa, "Quench behavior, quench protection of a YBCO test coil assembly," *IEEE transactions on applied superconductivity,* vol. 18, no. 2, pp. 1329-1332, 2008.

[24]   P. Mangin and R. Kahn, *Superconductivity: an introduction*. Springer, 2016.

[25]   K.-H. Bennemann and J. B. Ketterson, *Superconductivity: Volume 1: Conventional and Unconventional Superconductors Volume 2: Novel Superconductors*. Springer Science & Business Media, 2008.

[26]   S. C. Kaddour, J. Singleton, and S. Haddad, "Superconducting materials," *Journal of Physics: Condensed Matter,* vol. 23, no. 46, p. 460301, 2011.

[27]   J. G. Bednorz and K. A. Müller, "Possible highT c superconductivity in the Ba− La− Cu− O system," *Zeitschrift für Physik B Condensed Matter,* vol. 64, no. 2, pp. 189-193, 1986.

[28]   A. Saleem and S. T. Hussain, "Review the High Temperature Superconductor (HTSC) Cuprates-Properties and Applications," *Journal of Surfaces and Interfaces of Materials,* vol. 1, no. 2, pp. 97-119, 2013.

[29]   *Superconductivity in short*. Available: https://www.lhc-closer.es/taking_a_closer_look_at_lhc/0.superconductivity_in_short

[30]   S. Posen *et al.*, "Efficient expulsion of magnetic flux in superconducting radiofrequency cavities for high Q 0 applications," *Journal of Applied Physics,* vol. 119, no. 21, p. 213903, 2016.

[31]   S. United and R. Office of Naval, "Naval research reviews," (in English), *Naval research reviews,* 1959.

[32]   E. Krüger, "Constraining forces causing the Meissner effect," *arXiv preprint arXiv:1706.08737,* 2017.

[33]   J. Bardeen, "Theory of the Meissner effect in superconductors," *Physical Review,* vol. 97, no. 6, p. 1724, 1955.

[34]   G. Wentzel, "Meissner effect," *Physical Review,* vol. 111, no. 6, p. 1488, 1958.

[35]   E. Education. (2020, 7 Sep). *Superconductor*. Available: https://energyeducation.ca/encyclopedia/Superconductor

[36]   W. contributors. (2020). *Meissner effect. Wikipedia, The Free Encyclopedia*. Available: https://en.wikipedia.org/w/index.php?title=Meissner_effect&oldid=936808035

[37]   HyperPhysics. (2020, 3 Sep). *The Meissner Effect*. Available: http://hyperphysics.phy-astr.gsu.edu/hbase/Solids/meis.html

[38]   C. Rey and A. Malozemoff, "Fundamentals of superconductivity," in *Superconductors in the Power Grid*: Elsevier, 2015, pp. 29-73.

[39]   H. Physics. *Characteristic Lengths in Superconductors*. Available: http://hyperphysics.phy-astr.gsu.edu/hbase/Solids/chrlen.html

[40]   C. Plummer and J. Evetts, "Dependence of the shape of the resistive transition on composite inhomogeneity in multifilamentary wires," *IEEE Transactions on Magnetics,* vol. 23, no. 2, pp. 1179-1182, 1987.

[41]   J. Rhyner, "Magnetic properties and AC-losses of superconductors with power law current—voltage characteristics," *Physica C: Superconductivity,* vol. 212, no. 3-4, pp. 292-300, 1993.

[42]   S. S. Kalsi, *Applications of high temperature superconductors to electric power equipment*. John Wiley & Sons, 2011.

[43]   M. Chudy, Z. Zhong, M. Eisterer, and T. Coombs, "n-Values of commercial YBCO tapes before and after irradiation by fast neutrons," *Superconductor Science Technology,* vol. 28, no. 3, p. 035008, 2015.

[44]   B. Goodman, "Type II superconductors," *Reports on progress in physics,* vol. 29, no. 2, pp. 445-487, 1966.

[45]   V. Schmidt, P. Müller, and A. V. Ustinov, "Type-II Superconductors," in *The Physics of Superconductors*: Springer, 1997, pp. 101-137.

[46]   J. Bardeen, L. N. Cooper, and J. R. Schrieffer, "Microscopic theory of superconductivity," *Physical Review,* vol. 106, no. 1, p. 162, 1957.

[47]   HyperPhysics. (2020, 7 Sep). *BCS Theory of Superconductivity*. Available: http://hyperphysics.phy-astr.gsu.edu/hbase/Solids/bcs.html

[48]   S. Buga, G. Dubitsky, N. Serebryanaya, V. Kulbachinskii, and V. Blank, "Superhard Superconductive Composite Materials Obtained by High-Pressure-High-Temperature Sintering," *Applications of High-Tc Superconductivity,* p. 237, 2011.

[49]   P. Zhang *et al.*, "NbTi superconducting wires and applications," in *Titanium for Consumer Applications*: Elsevier, 2019, pp. 279-296.

[50]   Y. Li and Y. Gao, "Superconducting properties variation with A15 composition in Nb3Sn," *arXiv preprint arXiv:1408.0353,* 2014.

[51]   D. Larbalestier *et al.*, "Strongly linked current flow in polycrystalline forms of the superconductor MgB 2," *Nature,* vol. 410, no. 6825, pp. 186-189, 2001.

[52]   F. Rene, *Mgb2 Superconducting Wires: Basics And Applications*. World Scientific, 2016.

[53]   C. Buzea and T. Yamashita, "Review of the superconducting properties of MgB2," *Superconductor Science and Technology,* vol. 14, no. 11, p. R115, 2001.

[54]   K. Konstantopoulou *et al.*, "Electro-mechanical characterization of MgB2 wires for the Superconducting Link Project at CERN," *Superconductor Science and Technology,* vol. 29, no. 8, p. 084005, 2016.

[55] M.-K. Wu *et al.*, "Superconductivity at 93 K in a new mixed-phase Y-Ba-Cu-O compound system at ambient pressure," *Physical review letters,* vol. 58, no. 9, p. 908, 1987.

[56] H. Maeda, Y. Tanaka, M. Fukutomi, and T. Asano, "A new high-Tc oxide superconductor without a rare earth element," *Japanese Journal of Applied Physics,* vol. 27, no. 2A, p. L209, 1988.

[57] J. Tallon *et al.*, "High-Tc superconducting phases in the series Bi2. 1 (Ca, Sr) n+ lCunO2n+ 4+ δ," *Nature,* vol. 333, no. 6169, pp. 153-156, 1988.

[58] Z. Sheng and A. Hermann, "Bulk superconductivity at 120 K in the Tl–Ca/Ba–Cu–O system," *Nature,* vol. 332, no. 6160, pp. 138-139, 1988.

[59] A. Schilling, M. Cantoni, J. Guo, and H. Ott, "Superconductivity above 130 K in the Hg–Ba–Ca–Cu–O system," *Nature,* vol. 363, no. 6424, pp. 56-58, 1993.

[60] O. Van der Meer, B. ten Haken, and H. H. ten Kate, "A model to describe the angular dependence of the critical current in a Bi-2223/Ag superconducting tape," *Physica C: Superconductivity,* vol. 357, pp. 1174-1177, 2001.

[61] T. Kiss and H. Okamoto, "Anisotropic current transport properties and their scaling in multifilamentry Bi-2223 Ag-sheathed tapes," *IEEE transactions on applied superconductivity,* vol. 11, no. 1, pp. 3900-3903, 2001.

[62] T. Kiss *et al.*, "Angular dependence of critical current properties in YBCO coated tape under high magnetic field up to 18 T," *Physica C: Superconductivity,* vol. 378, pp. 1113-1117, 2002.

[63] K. Yamamoto, H. Mazaki, and H. Yasuoka, "Magnetization of type-II superconductors in the Kim-Anderson model," *Physical Review B,* vol. 47, no. 2, p. 915, 1993.

[64] Y. Kim, C. Hempstead, and A. Strnad, "Critical persistent currents in hard superconductors," *Physical Review Letters,* vol. 9, no. 7, p. 306, 1962.

[65] D. X. Chen and R. B. Goldfarb, "Kim model for magnetization of type-II superconductors," *Journal of Applied Physics,* vol. 66, no. 6, pp. 2489-2500, 1989.

[66] G. M. Zhang, L. Z. Lin, L. Y. Xiao, and Y. J. Yu, "A theoretical model for the angular dependence of the critical current of BSCCO/Ag tapes," *Physica C: Superconductivity,* vol. 390, no. 4, pp. 321-324, 2003.

[67] J. Clem, "Anisotropy and two-dimensional behaviour in the high-temperature superconductors," *Superconductor Science and Technology,* vol. 11, no. 10, p. 909, 1998.

[68] A. Shick, J. B. Ketterson, D. Novikov, and A. J. Freeman, "Electronic structure, phase stability, and semimetal-semiconductor transitions in Bi," *Physical Review B,* vol. 60, no. 23, p. 15484, 1999.

[69] Q. Hu *et al.*, "Anisotropy of the critical current in silver sheathed (Bi, Pb) 2Sr2Ca2Cu3O10 tapes," *Journal of applied physics,* vol. 78, no. 2, pp. 1123-1130, 1995.

[70] P. Kes, J. Aarts, V. Vinokur, and C. Van der Beek, "Dissipation in highly anisotropic superconductors," *Physical review letters,* vol. 64, no. 9, p. 1063, 1990.

[71] D. Finnemore, K. Gray, M. Maley, D. Welch, D. Christen, and D. Kroeger, "Coated conductor development: an assessment," *Physica C: Superconductivity,* vol. 320, no. 1-2, pp. 1-8, 1999.

[72] D. Turrioni, E. Barzi, M. J. Lamm, R. Yamada, A. Zlobin, and A. Kikuchi, "Study of HTS wires at high magnetic fields," *IEEE transactions on applied superconductivity,* vol. 19, no. 3, pp. 3057-3060, 2009.

[73] X. Xiong *et al.*, "High throughput processing of long-length IBAD MgO and epi-buffer templates at SuperPower," *IEEE transactions on applied superconductivity,* vol. 17, no. 2, pp. 3375-3378, 2007.

[74] V. Selvamanickam *et al.*, "Recent progress in second-generation HTS conductor scale-up at SuperPower," *IEEE Transactions on applied superconductivity,* vol. 17, no. 2, pp. 3231-3234, 2007.

[75] J. Sarrao, W. Kwok, and I. Bozovic, "Basic research needs for superconductivity," in *Report of the Basic Energy Sciences Workshop on Superconductivity*, 2006, pp. 8-11: sn.

[76] M. Rupich *et al.*, "Second generation HTS wire based on RABiTSTM substrates and MOD YBCO," *IEEE Trans. Appl. Superc,* vol. 15, p. 2458, 2005.

[77] P. P. S. Vemulakonda, "Comparative Characterization of Superconducting Thin Films Fabricated by Different Techniques," 2007.

[78] B. A. Howe, "Crystal structure and superconductivity of YBa2Cu3O7-x," 2014.

[79] W. V. Hassenzahl, S. E. Eckroad, P. M. Grant, B. Gregory, and S. Nilsson, "A high-power superconducting DC cable," *IEEE transactions on applied superconductivity,* vol. 19, no. 3, pp. 1756-1761, 2009.

[80] R. Garwin and J. Matisoo, "Superconducting lines for the transmission of large amounts of electrical power over great distances," *Proceedings of the IEEE,* vol. 55, no. 4, pp. 538-548, 1967.

[81] F. Edeskuty and P. Chowdhuri, "DC superconducting power transmission line project at LASL. US DOE Division of Electric Energy Systems. Progress report No. 19, October 1, 1976--September 30, 1977," Los Alamos Scientific Lab., N. Mex.(USA)1978.

[82] F. Edeskuty, R. Bartlett, and J. Dean, "Current test of a dc superconducting power transmission line," *IEEE Transactions on Magnetics,* vol. 17, no. 1, pp. 161-164, 1981.

[83] S. M. Schoenung, W. Hassenzahl, and P. Grant, "System study of long distance low voltage transmission using high temperature superconducting cable," *EPRI Report WO-12,* 1997.

[84] R. Cresap, W. Mittelstadt, D. Scott, and C. Taylor, "Operating experience with modulation of the Pacific HVDC intertie," *IEEE Transactions on Power Apparatus Systems,* no. 4, pp. 1053-1059, 1978.

[85] G. D. Breuer and R. L. Hauth, "HVDC's increasing popularity," *iEEE Potentials,* vol. 7, no. 2, pp. 18-21, 1988.

[86] Y. Zhang, T. F. Lehner, T. Fukushima, H. Sakamoto, and D. W. Hazelton, "Progress in production and performance of second generation (2G) HTS wire for practical applications," *IEEE Transactions on applied superconductivity,* vol. 24, no. 5, pp. 1-5, 2014.

[87] L. Xiao and L. Lin, "Recent progress of power application of superconductor in China," *IEEE transactions on applied superconductivity,* vol. 17, no. 2, pp. 2355-2360, 2007.

[88] S. Samoilenkov *et al.*, "Customised 2G HTS wire for applications," *Superconductor Science Technology,* vol. 29, no. 2, p. 024001, 2015.

[89] V. Hussennether, M. Oomen, M. Leghissa, and H.-W. Neumueller, "DC and AC properties of Bi-2223 cabled conductors designed for high-current applications," *Physica C: Superconductivity,* vol. 401, no. 1-4, pp. 135-139, 2004.

[90] M. Leghissa *et al.*, "Development and application of superconducting transformers," *Physica C: Superconductivity,* vol. 372, pp. 1688-1693, 2002.

[91]   M. N. Wilson, "Superconductivity and accelerators: the good companions," *IEEE transactions on applied superconductivity,* vol. 9, no. 2, pp. 111-121, 1999.

[92]   W. Goldacker, "Roebel cable from coated conductors," in *Proc. Late Breaking News Talk, CEC/ICMC Conf. Keystone*, 2005, pp. 1-44.

[93]   W. Goldacker *et al.*, "High current DyBCO-ROEBEL assembled coated conductor (RACC)," in *Journal of Physics: Conference Series*, 2006, vol. 43, no. 1, p. 901: IOP Publishing.

[94]   W. Goldacker, F. Grilli, E. Pardo, A. Kario, S. I. Schlachter, and M. Vojenčiak, "Roebel cables from REBCO coated conductors: a one-century-old concept for the superconductivity of the future," *Superconductor Science Technology,* vol. 27, no. 9, p. 093001, 2014.

[95]   W. Goldacker *et al.*, "ROEBEL assembled coated conductors (RACC): preparation, properties and progress," *IEEE transactions on applied superconductivity,* vol. 17, no. 2, pp. 3398-3401, 2007.

[96]   C. Schmidt, "AC losses in ROBEL Assembled Coated Conductors–RACC," *at ISS- Nagoya, 31th. Oct-2 Nov,* 2006.

[97]   W. Goldacker *et al.*, "Critical currents in ROEBEL assembled coated conductors (RACC)," in *AIP Conference Proceedings*, 2008, vol. 986, no. 1, pp. 461-470: American Institute of Physics.

[98]   N. Long *et al.*, "Narrow strand YBCO Roebel cable for lowered AC loss," in *Journal of Physics: Conference Series*, 2008, vol. 97, no. 1, p. 012280: IOP Publishing.

[99]   W. Goldacker *et al.*, "Status of high transport current ROEBEL assembled coated conductor cables," *Superconductor Science Technology,* vol. 22, no. 3, p. 034003, 2009.

[100]   S. Fetisov *et al.*, "Development and characterization of a 2G HTS Roebel cable for aircraft power systems," *IEEE Transactions on Applied Superconductivity,* vol. 26, no. 3, pp. 1-4, 2016.

[101]   M. Takayasu, L. Chiesa, L. Bromberg, and J. V. Minervini, "HTS twisted stacked-tape cable conductor," *Superconductor Science Technology,* vol. 25, no. 1, p. 014011, 2011.

[102]   M. Takayasu, J. V. Minervini, and L. Bromberg, "Torsion strain effects on critical currents of HTS superconducting tapes," in *AIP Conference Proceedings*, 2010, vol. 1219, no. 1, pp. 337-344: American Institute of Physics.

[103]   M. Takayasu, L. Chiesa, L. Bromberg, and J. Minervini, "Investigations of HTS Twisted Stacked-Tape Conductor," 2011.

[104]   M. Takayasu, L. Chiesa, L. Bromberg, and J. Minervini, "Cabling method for high current conductors made of HTS tapes," *IEEE transactions on applied superconductivity,* vol. 21, no. 3, pp. 2340-2344, 2010.

[105]   M. Takayasu, "Superconducting tape cable termination," *US provisional patent application,* no. 61/400,858, 2010.

[106]   A. Ballarino, J. Fleiter, J. Hurte, M. Sitko, and G. Willering, "First tests of twisted-pair HTS 1 kA range cables for use in superconducting links," *Physics Procedia,* vol. 36, pp. 855-858, 2012.

[107]   L. Chiesa, N. Allen, and M. Takayasu, "Electromechanical investigation of 2G HTS twisted stacked-tape cable conductors," *IEEE transactions on applied superconductivity,* vol. 24, no. 3, pp. 1-5, 2013.

[108] M. Tomita *et al.*, "Critical Current Properties of HTS Twisted Stacked-Tape Cable in Subcooled-and Pressurized-Liquid Nitrogen," in *IOP Conference Series: Materials Science and Engineering*, 2015, vol. 102, no. 1, p. 012024: IOP Publishing.

[109] M. Takayasu, L. Chiesa, P. D. Noyes, and J. V. Minervini, "Investigation of HTS twisted stacked-tape cable (TSTC) conductor for high-field, high-current fusion magnets," *IEEE Transactions on Applied Superconductivity,* vol. 27, no. 4, pp. 1-5, 2017.

[110] D. C. van der Laan, "YBa2Cu3O7− δ coated conductor cabling for low ac-loss and high-field magnet applications," *Superconductor Science Technology,* vol. 22, no. 6, p. 065013, 2009.

[111] C. Barth, D. Van der Laan, N. Bagrets, C. M. Bayer, K.-P. Weiss, and C. Lange, "Temperature-and field-dependent characterization of a conductor on round core cable," *Superconductor Science Technology,* vol. 28, no. 6, p. 065007, 2015.

[112] D. C. van der Laan, P. D. Noyes, G. Miller, H. W. Weijers, and G. Willering, "Characterization of a high-temperature superconducting conductor on round core cables in magnetic fields up to 20 T," *Superconductor Science Technology,* vol. 26, no. 4, p. 045005, 2013.

[113] M. Majoros, M. Sumption, E. Collings, and D. Van der Laan, "Magnetization losses in superconducting YBCO conductor-on-round-core (CORC) cables," *Superconductor Science Technology,* vol. 27, no. 12, p. 125008, 2014.

[114] C. P. Bean, "Magnetization of high-field superconductors," *Reviews of modern physics,* vol. 36, no. 1, p. 31, 1964.

[115] C. P. Bean, "Magnetization of hard superconductors," *Physical review letters,* vol. 8, no. 6, p. 250, 1962.

[116] W. Yuan, *Second-generation high-temperature superconducting coils and their applications for energy storage*. Springer Science & Business Media, 2011.

[117] L. Prigozhin, "On the Bean critical-state model in superconductivity," *European Journal of Applied Mathematics,* vol. 7, no. 3, pp. 237-247, 1996.

[118] P. W. Anderson and Y. Kim, "Hard superconductivity: theory of the motion of Abrikosov flux lines," *Reviews of modern physics,* vol. 36, no. 1, p. 39, 1964.

[119] Y. Kim, C. Hempstead, and A. Strnad, "Magnetization and critical supercurrents," *Physical Review,* vol. 129, no. 2, p. 528, 1963.

[120] P. W. Anderson, "Theory of flux creep in hard superconductors," *Physical Review Letters,* vol. 9, no. 7, p. 309, 1962.

[121] H. Yasuoka, S. Tochihara, M. Mashino, and H. Mazaki, "Material parameters of YBa2Cu3Oy in the Kim–Anderson critical-state model," *Physica C: Superconductivity,* vol. 305, no. 1-2, pp. 125-138, 1998.

[122] W. Norris, "Calculation of hysteresis losses in hard superconductors carrying ac: isolated conductors and edges of thin sheets," *Journal of Physics D: Applied Physics,* vol. 3, no. 4, p. 489, 1970.

[123] E. H. Brandt and M. Indenbom, "Type-II-superconductor strip with current in a perpendicular magnetic field," *Physical review B,* vol. 48, no. 17, p. 12893, 1993.

[124] P. P. Silvester and R. L. Ferrari, *Finite elements for electrical engineers*. Cambridge university press, 1996.

[125]   J. R. Clem, J. Claassen, and Y. Mawatari, "AC losses in a finite Z stack using an anisotropic homogeneous-medium approximation," *Superconductor Science Technology,* vol. 20, no. 12, p. 1130, 2007.

[126]   W. Yuan, A. Campbell, Z. Hong, M. Ainslie, and T. Coombs, "Comparison of AC losses, magnetic field/current distributions and critical currents of superconducting circular pancake coils and infinitely long stacks using coated conductors," *Superconductor Science Technology,* vol. 23, no. 8, p. 085011, 2010.

[127]   W. Yuan, A. Campbell, and T. Coombs, "A model for calculating the AC losses of second-generation high temperature superconductor pancake coils," *Superconductor Science Technology,* vol. 22, no. 7, p. 075028, 2009.

[128]   E. Pardo, "Modeling of coated conductor pancake coils with a large number of turns," *Superconductor Science Technology,* vol. 21, no. 6, p. 065014, 2008.

[129]   E. Pardo, J. Šouc, and J. Kováč, "AC loss in ReBCO pancake coils and stacks of them: modelling and measurement," *Superconductor Science Technology,* vol. 25, no. 3, p. 035003, 2012.

[130]   L. Prigozhin, "Analysis of critical-state problems in type-II superconductivity," *IEEE Transactions on Applied Superconductivity,* vol. 7, no. 4, pp. 3866-3873, 1997.

[131]   L. Prigozhin and V. Sokolovsky, "Computing AC losses in stacks of high-temperature superconducting tapes," *Superconductor Science Technology,* vol. 24, no. 7, p. 075012, 2011.

[132]   G. Barnes, M. McCulloch, and D. Dew-Hughes, "Computer modelling of type II superconductors in applications," *Superconductor Science and Technology,* vol. 12, no. 8, p. 518, 1999.

[133]   T. Coombs, A. Campbell, A. Murphy, and M. Emmens, "A fast algorithm for calculating the critical state in superconductors," *COMPEL-The international journal for computation and mathematics in electrical and electronic engineering,* vol. 20, no. 1, pp. 240-252, 2001.

[134]   N. Amemiya, S.-i. Murasawa, N. Banno, and K. Miyamoto, "Numerical modelings of superconducting wires for AC loss calculations," *Physica C: Superconductivity,* vol. 310, no. 1, pp. 16-29, 1998/12/01/ 1998.

[135]   G. Meunier, Y. Le Floch, and C. Guérin, "A nonlinear circuit coupled t-t/sub 0/-phi formulation for solid conductors," *IEEE Transactions on Magnetics,* vol. 39, pp. 1729-1732, 2003.

[136]   A. Campbell, "An introduction to numerical methods in superconductors," *Journal of superconductivity novel magnetism,* vol. 24, no. 1-2, pp. 27-33, 2011.

[137]   A. Campbell, "A direct method for obtaining the critical state in two and three dimensions," *Superconductor Science Technology,* vol. 22, no. 3, p. 034005, 2009.

[138]   H. Zhang, "Study of Second Generation High Temperature Superconducting Coils for Energy Storage System," 2016. University of Bath

[139]   N. Amemiya, K. Miyamoto, N. Banno, and O. Tsukamoto, "Numerical analysis of AC losses in high T/sub c/superconductors based on Ej characteristics represented with n-value," *IEEE transactions on applied superconductivity,* vol. 7, no. 2, pp. 2110-2113, 1997.

[140]   N. Banno and N. Amemiya, "Numerical analysis of AC loss in high T/sub c/twisted tape carrying AC transport current in external AC magnetic field. Effect of twisting on loss reduction," *IEEE transactions on applied superconductivity,* vol. 9, no. 2, pp. 2561-2564, 1999.

[141]   R. Brambilla, F. Grilli, and L. Martini, "Development of an edge-element model for AC loss computation of high-temperature superconductors," *Superconductor Science Technology,* vol. 20, no. 1, p. 16, 2006.

[142]   Z. Hong, A. Campbell, and T. Coombs, "Numerical solution of critical state in superconductivity by finite element software," *Superconductor Science Technology,* vol. 19, no. 12, p. 1246, 2006.

[143]   F. Grilli and S. P. Ashworth, "Measuring transport AC losses in YBCO-coated conductor coils," *Superconductor Science Technology,* vol. 20, no. 8, p. 794, 2007.

[144]   M. Zhang, J. Kvitkovic, S. Pamidi, and T. Coombs, "Experimental and numerical study of a YBCO pancake coil with a magnetic substrate," *Superconductor Science technology,* vol. 25, no. 12, p. 125020, 2012.

[145]   M. Zhang, K. Matsuda, and T. Coombs, "New application of temperature-dependent modelling of high temperature superconductors: Quench propagation and pulse magnetization," *Journal of Applied Physics,* vol. 112, no. 4, p. 043912, 2012.

[146]   H. Zhang, M. Zhang, and W. Yuan, "An efficient 3D finite element method model based on the T–A formulation for superconducting coated conductors," *Superconductor Science and Technology,* vol. 30, no. 2, p. 024005, 2016.

[147]   F. Liang *et al.*, "A finite element model for simulating second generation high temperature superconducting coils/stacks with large number of turns," *Journal of Applied Physics,* vol. 122, no. 4, p. 043903, 2017.

[148]   Z. Jiang *et al.*, "The dependence of AC loss characteristics on the spacing between strands in YBCO Roebel cables," *Superconductor Science Technology,* vol. 24, no. 6, p. 065005, 2011.

[149]   M. Majoros, M. D. Sumption, E. W. Collings, and D. C. van der Laan, "Magnetization losses in superconducting YBCO conductor-on-round-core (CORC) cables," *Superconductor Science & Technology,* vol. 27, no. 12, Dec 2014, Art. no. 125008.

[150]   J. Šouc *et al.*, "Low AC loss cable produced from transposed striated CC tapes," *Superconductor Science and Technology,* vol. 26, no. 7, p. 075020, 2013.

[151]   J. Sheng, M. Vojenčiak, R. Terzioğlu, L. Frolek, and F. Gömöry, "Numerical Study on Magnetization Characteristics of Superconducting Conductor on Round Core Cables," *IEEE Transactions on Applied Superconductivity,* vol. 27, no. 4, pp. 1-5, 2017.

[152]   Q. Li, N. Amemiya, K. Takeuchi, T. Nakamura, and N. Fujiwara, "AC loss characteristics of superconducting power transmission cables: gap effect andJcdistribution effect," *Superconductor Science and Technology,* vol. 23, no. 11, p. 115003, 2010/09/28 2010.

[153]   L. Bottura, "Magnet quench 101," *arXiv preprint arXiv:1401.3927,* 2014.

[154]   Z.-m. Bai, X. Wu, C.-l. Wu, and J.-x. Wang, "Quench propagation properties analysis of high-temperature superconductors using finite element method," *Physica C: Superconductivity,* vol. 436, no. 2, pp. 99-102, 2006.

[155]   B. Seeber, *Handbook of applied superconductivity*. CRC press, 1998.

[156]   A. Shajii and J. P. Freidberg, "Quench in superconducting magnets. I. Model and numerical implementation," *Journal of applied physics,* vol. 76, no. 5, pp. 3149-3158, 1994.

[157] R. Bellis and Y. Iwasa, "Quench propagation in high Tc superconductors," *Cryogenics,* vol. 34, no. 2, pp. 129-144, 1994.

[158] A. V. Gurevich and R. Mints, "Self-heating in normal metals and superconductors," *Reviews of modern physics,* vol. 59, no. 4, p. 941, 1987.

[159] C. Lacroix, J.-H. Fournier-Lupien, K. McMeekin, and F. Sirois, "Normal zone propagation velocity in 2G HTS coated conductor with high interfacial resistance," *IEEE transactions on applied superconductivity,* vol. 23, no. 3, pp. 4701605-4701605, 2013.

[160] Y. Liyang, L. Pei, S. Tengming, and S. Justin, "Quench degradation limit of multifilamentary Ag/Bi 2 Sr 2 CaCu 2 O x round wires," *Superconductor Science and Technology,* vol. 29, no. 3, p. 035010, 2016.

[161] S. Tengming, Y. Liyang, and L. Pei, "Feasible voltage-tap based quench detection in a Ag/Bi-2212 coil enabled by fast 3D normal zone propagation," *Superconductor Science and Technology,* vol. 29, no. 8, p. 08LT01, 2016.

[162] H. Song and J. Schwartz, "Stability and Quench Behavior of YBa2Cu3O7-x Coated Conductor at 4.2 K, Self-Field," *Ieee Transactions on Applied Superconductivity,* vol. 19, no. 5, pp. 3735-3743, Oct 2009.

[163] W. K. Chan and J. Schwartz, "Three-Dimensional Micrometer-Scale Modeling of Quenching in High-Aspect-Ratio YBa2Cu3O7-delta Coated Conductor Tapes-Part II: Influence of Geometric and Material Properties and Implications for Conductor Engineering and Magnet Design," (in English), *Ieee Transactions on Applied Superconductivity,* vol. 21, no. 6, pp. 3628-3634, Dec 2011.

[164] G. P. Willering, D. C. van der Laan, H. W. Weijers, P. D. Noyes, G. E. Miller, and Y. Viouchkov, "Effect of variations in terminal contact resistances on the current distribution in high-temperature superconducting cables," *Superconductor Science & Technology,* vol. 28, no. 3, Mar 2015, Art. no. 035001.

[165] Y. Wang, J. Zheng, Z. Zhu, M. Zhang, and W. Yuan, "Quench behavior of high-temperature superconductor (RE) Ba2Cu3O x CORC cable," *Journal of Physics D: Applied Physics,* vol. 52, no. 34, p. 345303, 2019.

[166] M. Majoros, M. D. Sumption, E. W. Collings, and D. v. d. Laan, "Stability and normal zone propagation in YBCO CORC cables," *Superconductor Science and Technology,* vol. 29, no. 4, p. 044006, 2016.

[167] Y. Iwasa, *Case studies in superconducting magnets: design and operational issues*. Springer Science & Business Media, 2009.

[168] S. Fu *et al.*, "Numerical study on AC loss properties of HTS cable consisting of YBCO coated conductor for HTS power devices," *IEEE Transactions on Applied Superconductivity,* vol. 28, no. 4, pp. 1-5, 2018.

[169] J. Sheng, M. Vojenciak, R. Terzioglu, L. Frolek, and F. Gomory, "Numerical Study on Magnetization Characteristics of Superconducting Conductor on Round Core Cables," *Ieee Transactions on Applied Superconductivity,* vol. 27, no. 4, Jun 2017, Art. no. 4800305.

[170] J. Zhenan, A. Naoyuki, and N. Masaaki, "Numerical calculation of AC losses in multi-layer superconducting cables composed of coated conductors," *Superconductor Science and Technology,* vol. 21, no. 2, p. 025013, 2008.

[171] R. Terzioglu, M. Vojenciak, J. Sheng, F. Gomory, T. F. Ccedil;avus, and I. Belenli, "AC loss characteristics of CORC((R))cable with a Cu former," *Superconductor Science & Technology,* vol. 30, no. 8, Aug 2017, Art. no. 085012.

[172] Y. Wang, W. K. Chan, and J. Schwartz, "Self-protection mechanisms in no-insulation (RE) Ba2Cu3O x high temperature superconductor pancake coils," *Superconductor Science and Technology,* vol. 29, no. 4, p. 045007, 2016.

[173] Z. Zhu, Y. Wang, D. Xing, X. Pei, M. Zhang, and W. Yuan, "Quench of a single-layer ReBCO CORC cable with non-uniform terminal contact resistance," *IEEE Transactions on Applied Superconductivity,* vol. 29, no. 5, pp. 1-5, 2019.

[174] A. Álvarez, P. Suárez, B. Pérez, and L. García, "Coated superconducting tape model based on the distribution of currents between the tape layers: computing implementation," *IEEE Transactions on Applied Superconductivity,* vol. 28, no. 4, pp. 1-5, 2018.

[175] W. K. Chan and J. Schwartz, "A Hierarchical Three-Dimensional Multiscale Electro–Magneto–Thermal Model of Quenching in $\hbox {REBa} _ {2}\hbox {Cu} _ {3}\hbox {O} _ {7-\delta} $ Coated-Conductor-Based Coils," *IEEE transactions on applied superconductivity,* vol. 22, no. 5, pp. 4706010-4706010, 2012.

[176] J. Lu, E. S. Choi, and H. D. Zhou, "Physical properties of Hastelloy (R) C-276 (TM) at cryogenic temperatures," (in English), *Journal of Applied Physics,* vol. 103, no. 6, Mar 15 2008.

[177] MachineDesign. (2016). *The Future of Electric Hybrid Aviation*. Available: https://www.machinedesign.com/automation-iiot/batteries-power-supplies/article/21831997/the-future-of-electric-hybrid-aviation

[178] U. A. ICAO. (2016). *Historic agreement reached to mitigate international aviation emissions*. Available: https://www.icao.int/Newsroom/Pages/Historic-agreement-reached-to-mitigate-international-aviation-emissions.aspx

[179] E. National Academies of Sciences and Medicine, *Commercial aircraft propulsion and energy systems research: reducing global carbon emissions*. National Academies Press, 2016.

[180] J. Felder, "NASA Hybrid Electric Propulsion Systems Structures," *Presentation to committee on September,* vol. 1, p. 2015, 2015.

[181] R. Quigley, "More electric aircraft," in *Proceedings Eighth Annual Applied Power Electronics Conference and Exposition*, 1993, pp. 906-911: IEEE.

[182] R. Telford, S. Galloway, and G. M. Burt, "Evaluating the reliability & availability of more-electric aircraft power systems," in *2012 47th International Universities Power Engineering Conference (UPEC)*, 2012, pp. 1-6: IEEE.

[183] L. Han, J. Wang, and D. Howe, "Small-signal stability studies of a 270 V DC more-electric aircraft power system," 2006.

[184] K. Areerak, S. Bozhko, G. Asher, L. De Lillo, and D. W. Thomas, "Stability study for a hybrid AC-DC more-electric aircraft power system," *IEEE Transactions on Aerospace Electronic Systems,* vol. 48, no. 1, pp. 329-347, 2012.

[185] A. Griffo and J. Wang, "Large signal stability analysis of'more electric'aircraft power systems with constant power loads," *IEEE Transactions on Aerospace Electronic Systems,* vol. 48, no. 1, pp. 477-489, 2012.

[186]   R. Burgos, G. Chen, F. Wang, D. Boroyevich, W. G. Odendaal, and J. D. Van Wyk, "Reliability-oriented design of three-phase power converters for aircraft applications," *IEEE Transactions on Aerospace Electronic Systems,* vol. 48, no. 2, pp. 1249-1263, 2012.

[187]   A. Lücken, J. Brombach, and D. Schulz, "Design and protection of a high voltage DC onboard grid with integrated fuel cell system on more electric aircraft," in *Electrical Systems for Aircraft, Railway and Ship Propulsion*, 2010, pp. 1-6: IEEE.

[188]   C. A. Luongo *et al.*, "Next generation more-electric aircraft: A potential application for HTS superconductors," *IEEE Transactions on applied superconductivity,* vol. 19, no. 3, pp. 1055-1068, 2009.

[189]   R. Singh, H. D. Kim, J. L. Felder, M. T. Tong, J. J. Berton, and W. J. Haller, "Turboelectric distributed propulsion benefits on the N3-X vehicle," *Aircraft Engineering Aerospace Technology: An International Journal,* 2014.

[190]   N. Madavan, "NASA Investments in Electric Propulsion Technologies for Large Commercial Aircraft," 2016.

[191]   P. J. Masson, M. Breschi, P. Tixador, and C. A. Luongo, "Design of HTS axial flux motor for aircraft propulsion," *IEEE Transactions on Applied Superconductivity,* vol. 17, no. 2, pp. 1533-1536, 2007.

[192]   F. Berg, J. Palmer, P. Miller, M. Husband, and G. Dodds, "HTS electrical system for a distributed propulsion aircraft," *IEEE Transactions on Applied Superconductivity,* vol. 25, no. 3, pp. 1-5, 2015.

[193]   C. Pornet and A. T. Isikveren, "Conceptual design of hybrid-electric transport aircraft," *Progress in Aerospace Sciences,* vol. 79, pp. 114-135, 2015.

[194]   M. Young *et al.*, "An investigation of the current distribution in the triaxial cable and its operational impacts on a power system," *IEEE transactions on applied superconductivity,* vol. 15, no. 2, pp. 1751-1754, 2005.

[195]   S. S. Fetisov, V. V. Zubko, S. Y. Zanegin, A. A. Nosov, S. M. Ryabov, and V. S. Vysotsky, "Study of the first russian triaxial HTS cable prototypes," *IEEE Transactions on Applied Superconductivity,* vol. 27, no. 4, pp. 1-5, 2017.

[196]   M. Stemmle, F. Merschel, M. Noe, and A. Hobl, "Plenary talk—European project and application of high T c superconducting cable," in *2013 IEEE International Conference on Applied Superconductivity and Electromagnetic Devices*, 2013, pp. 257-257: IEEE.

[197]   M. Zhang, F. Eastham, and W. Yuan, "Design and modeling of 2G HTS armature winding for electric aircraft propulsion applications," *IEEE Transactions on Applied Superconductivity,* vol. 26, no. 3, pp. 1-5, 2016.

[198]   E. Lavopa, P. Zanchetta, M. Sumner, and F. Cupertino, "Real-time estimation of fundamental frequency and harmonics for active shunt power filters in aircraft electrical systems," *Physica C: Superconductivity,* vol. 56, no. 8, pp. 2875-2884, 2009.

[199]   Z. Yao *et al.*, "Influence of substrates in HTS wires on AC loss characteristics of cylindrical single layer conductors," *Journal of Superconductivity Novel Magnetism,* vol. 28, no. 12, pp. 3447-3453, 2015.

[200]   S. Venuturumilli *et al.*, "Forceful uniform current distribution among all the tapes of a coaxial cable to enhance the operational current," *IEEE Transactions on Applied Superconductivity,* vol. 27, no. 4, pp. 1-4, 2016.

[201]   Z. Zhu, Y. Wang, S. Venuturumilli, J. Sheng, M. Zhang, and W. Yuan, "Influence of Harmonic Current on Magnetization Loss of a Triaxial CORC REBCO Cable for Hybrid Electric Aircraft," *IEEE Transactions on Applied Superconductivity,* vol. 28, no. 4, pp. 1-5, 2018.

[202]   W. Y. a. Z. Z. a. D. P. a. A. Yu, "Periodic boundary conditions for discrete element method simulation of particle flow in cylindrical vessels," *Industrial and Engineering Chemistry Research,* vol. 53, no. 0888-5885, pp. 8245 -- 8256, 2014, Art. no. 19.

[203]   J. C. del-Pino-López, M. Hatlo, and P. Cruz-Romero, "On simplified 3D finite element simulations of three-core armored power cables," *Energies,* vol. 11, no. 11, p. 3081, 2018.

[204]   L. S. Lakshmi *et al.*, "Frequency dependence of magnetic ac loss in a Roebel cable made of YBCO on a Ni-W substrate," *Superconductor Science & Technology,* vol. 23, no. 8, Aug 2010, Art. no. 085009.